

# Binary Neutron Stars with Generic Spin, Eccentricity, Mass ratio, and Compactness - Quasi-equilibrium Sequences and First Evolutions

Tim Dietrich,<sup>1</sup> Niclas Moldenhauer,<sup>1</sup> Nathan K. Johnson-McDaniel,<sup>2</sup> Sebastiano Bernuzzi,<sup>3,4</sup> Charalampos M. Markakis,<sup>5</sup> Bernd Brügmann,<sup>1</sup> and Wolfgang Tichy<sup>6</sup>

<sup>1</sup>*Theoretical Physics Institute, University of Jena, 07743 Jena, Germany*

<sup>2</sup>*International Centre for Theoretical Sciences, Tata Institute of Fundamental Research, Bengaluru 560012, India*

<sup>3</sup>*Theoretical Astrophysics, California Institute of Technology,  
1200 E California Blvd, Pasadena, California 91125, USA*

<sup>4</sup>*DiFeST, University of Parma, and INFN Parma, I-43124 Parma, Italy*

<sup>5</sup>*Mathematical Sciences, University of Southampton, Southampton SO17 1BJ, United Kingdom*

<sup>6</sup>*Department of Physics, Florida Atlantic University, Boca Raton, FL 33431 USA*

(Dated: February 19, 2022)

Information about the last stages of a binary neutron star inspiral and the final merger can be extracted from quasi-equilibrium configurations and dynamical evolutions. In this article, we construct quasi-equilibrium configurations for different spins, eccentricities, mass ratios, compactnesses, and equations of state. For this purpose we employ the SGRID code, which allows us to construct such data in previously inaccessible regions of the parameter space. In particular, we consider spinning neutron stars in isolation and in binary systems; we incorporate new methods to produce highly eccentric and eccentricity reduced data; we present the possibility of computing data for significantly unequal-mass binaries with mass ratios  $q \simeq 2$ ; and we create equal-mass binaries with individual compactness up to  $\mathcal{C} \simeq 0.23$ . As a proof of principle, we explore the dynamical evolution of three new configurations. First, we simulate a  $q = 2.06$  mass ratio which is the highest mass ratio for a binary neutron star evolved in numerical relativity to date. We find that mass transfer from the companion star sets in a few revolutions before merger and a rest mass of  $\sim 10^{-2} M_{\odot}$  is transferred between the two stars. This amount of mass accretion corresponds to  $\sim 10^{51}$  ergs of accretion energy. This configuration also ejects a large amount of material during merger ( $\sim 7.6 \times 10^{-2} M_{\odot}$ ), imparting a substantial kick to the remnant neutron star. Second, we simulate the first merger of a precessing binary neutron star. We present the dominant modes of the gravitational waves for the precessing simulation, where a clear imprint of the precession is visible in the (2,1) mode. Finally, we quantify the effect of an eccentricity reduction procedure on the gravitational waveform. The procedure improves the waveform quality and should be employed in future precision studies. However, one also needs to reduce other errors in the waveforms, notably truncation errors, in order for the improvement due to eccentricity reduction to be effective.

Contents		
I. Introduction	2	1. Mass transfer 19
II. Method	3	2. Ejecta and kick 20
A. General Framework	3	3. Gravitational waves 21
1. Assumptions for metric variables	4	B. A precessing unequal mass binary 22
2. Assumptions for matter variables	5	1. Dynamics 22
B. Specifying the symmetry vector	6	2. Gravitational Waves 24
III. Code description	6	C. Effect of eccentricity reduction on waveform phasing 26
A. Grid configuration	6	VI. Conclusions 26
B. Iteration procedure	8	A. Quasi-equilibrium sequences 27
C. Code Improvements	8	B. Dynamical Evolutions 27
1. Including piecewise polytropes	8	Acknowledgments 28
2. Updating $\Omega$ and $x_{CM}^1$	9	A. Astrophysical predictions for more extreme masses, mass ratios, and spins for binary neutron stars 28
IV. Binary neutron stars in Quasi-equilibrium	10	1. Large and small masses and larger mass ratios 28
A. Spins	10	2. Larger spins 30
B. Highly eccentric configurations	12	3. Neutron star spin predictions at merger 31
C. Orbits with reduced eccentricity	14	B. Alternative derivation of a first integral to the Euler equation 32
D. Unequal masses	16	C. Single CRV-stars 32
E. High compactness	17	1. Comparison with rigidly rotating stars 32
F. Convergence of SGRID	17	
V. Dynamical Evolutions	19	
A. A $q = 2.06$ binary	19	

2. Empirical $\omega$ - $j$ -Relation	33
3. Rapidly rotating neutron stars	33
References	34

## I. INTRODUCTION

The majority of coalescing binary neutron star systems are often expected to have negligible eccentricity, low spins, and be very close to equal-mass (with masses around  $1.35M_{\odot}$ ). These expectations are based on the masses and spins of the population of observed binary neutron stars where at least one star is seen as a radio pulsar (see, e.g., [1, 2]), combined with the efficient shedding of eccentricity due to gravitational waves (GWs) during the long inspiral [3, 4]. However, this observed population is quite small, currently consisting of around 12 systems. For many of these systems, the evidence that the companion of the pulsar is in fact another neutron star is indirect, at best—the companion could still be a fairly massive white dwarf (see, e.g., Sec. 8 in [5] for some discussion of this issue). Moreover, of these 12 systems, only 7 have well-determined masses, and only 6 systems (all with well-determined masses) will merge within a Hubble time, and thus contribute directly to merger rate calculations; see, e.g., Table 2 of [6] and Table 1 in [1, 2]. It is thus unclear to what extent these small spins, medium masses, and small mass ratios are just a selection effect.

On the one hand, population synthesis models for binaries formed “*in situ*” (e.g., [7]) predict a much wider range of masses and mass ratios than those currently observed; see the discussion in Appendix A 1. Also the spins at merger could potentially be considerably higher than those observed in binary pulsars to date, which is discussed in Appendix A 2. On the other hand, dynamical capture in dense stellar regions, such as globular clusters, offers the possibility of forming quite exotic objects, such as double millisecond pulsars [8, 9]. In fact, there is good evidence that dynamical capture and exchange interactions involving neutron stars are a frequent occurrence in globular clusters [10]. Binaries formed by dynamical capture might also have nonnegligible eccentricity at merger [11].

Numerical simulations in full general relativistic hydrodynamics are the only way to make accurate theoretical predictions for the properties of these systems in the time period around merger. A prerequisite for all simulations are accurate initial data that solve the Einstein constraint equations along with the Euler equation on the initial hypersurface and also describe the physical system one wants to study at some instant of time. Generally, one also wants to have this time be not too far from merger, to avoid an excessively expensive computation to reach the merger. Additionally, quasi-equilibrium sequences of initial data at different separations can be used to study certain pre-merger properties of these systems without a full dynamical evolution.

Given the potential diversity of the population of coalescing neutron stars in the universe, it is important to be able to generate accurate initial data for as much of the

potential parameter space as possible. In particular, even relatively small spin and eccentricity can significantly bias measurements of the neutron star tidal deformabilities, affecting their ability to constrain the nuclear equation of state [12, 13]. Also note that higher mass-ratio neutron star systems, even if rare, are quite interesting from a gravitational wave data analysis standpoint, since the individual masses of a  $q = 2.5$  system could be measured much more precisely than for equal-mass systems [14].

There are a number of well-developed codes for computing binary neutron star initial data in certain portions of the parameter space, most notably the open source spectral code LORENE [15]. Other codes include the Princeton group’s multigrid solver [16], BAM’s multigrid solver [17], the COCAL code [18], the SpEC code’s spectral solver [19–21], and our spectral code SGRID [22–24]. All these codes are incapable of reaching certain portions of the possible binary neutron star parameter space. In particular, they cannot generate consistent initial data with (noncorotating) spin with specified eccentricities. They also generally have difficulty reaching large compactnesses and high mass ratios. Additionally, when one evolves quasicircular initial data computed using these codes, one obtains an eccentricity of  $\sim 10^{-2}$ , which is orders of magnitude larger than we would expect in most binary neutron star systems (see, e.g., [4]). There are standard methods for iteratively reducing eccentricity in binary black hole initial data (e.g., [25–28]). However, it is not possible to apply these methods to binary neutron star initial data generated with the standard helical Killing vector technique. Such methods can only be applied to consistent initial data if one appropriately generalizes the helical Killing vector, as was only done recently in [17, 29]. Finally, there is no known way of including magnetic fields consistently in binary neutron star initial data—they are added by hand in all studies that include them.

Of course, it is possible to generate less accurate initial data in large regions of parameter space if one does not solve the Euler equation and possibly not even the Einstein constraint equations (e.g., using superpositions of boosted isolated star solutions, possibly with constraint solving, as was done in, e.g., [16, 30–34]). However, if one uses inconsistent initial data to initialize a simulation, it is always unclear how accurate the resulting simulation will be.

Recently, there has been progress in generating consistent initial data in all these portions of parameter space (except for magnetic fields). One of us presented a method for constructing consistent binary neutron star initial data with arbitrary spin using the constant rotational velocity (CRV) approach in [23] and implemented the method in SGRID in [24]. This method has now also been implemented by other groups [18, 21]. There has also been some work on obtaining somewhat high mass ratios (up to  $q = 1.5$  [35, 36]) and high compactnesses (up to  $\mathcal{C} \simeq 0.26$  [37]), but neither of these are close to the maximum mass ratios (at least  $\sim 2$ ; possibly up to  $\sim 3$  for a large maximum neutron star mass) and compactnesses (up to  $\sim 0.3$ ) that are (at least in principle) possible. We also presented a method for generating consistent binary

neutron star initial data with arbitrary eccentricity, including the possibility of reducing the eccentricity present in standard quasicircular data, in [17]. Concurrently, [29] applied a similar method for eccentricity reduction of binary neutron star initial data.

Here, we use SGRID to construct binary neutron star initial data pushing in all these directions. We have implemented the eccentric neutron star binary initial data construction method from [17] in SGRID, allowing us to solve for the velocity potential, which was not feasible in our initial multigrid implementation. We have also implemented piecewise polytropes in SGRID, allowing us to construct initial data with more realistic equations of state (EOSs). We thus show the improvement in the initial density oscillations of the simple polytropic highly eccentric data from [17] with the new SGRID data, and also construct eccentricity-reduced initial data for a simple polytropic and a realistic EOS. We also compute aligned spin initial data with somewhat larger spins than in [38] (as well as for more realistic EOSs). Finally, we illustrate the ability of SGRID to compute binary initial data with compactnesses up to  $\mathcal{C} \sim 0.23$  as well as to compute high mass-ratio initial data ( $q = 2.06$ ) with a realistic EOS.

Of course, one would like to study the phenomena around merger in these newly accessible portions of the binary neutron star parameter space: Around merger, the strongest gravitational wave, electromagnetic, and neutrino emission happens; see [39] for a review of binary neutron star simulations. Such a study requires dynamical evolutions, which will start from initial data provided by a member of a quasi-equilibrium sequence. In recent years there has been significant work on improving binary neutron star simulations on many fronts, notably by including more realistic equations of state from piecewise polytropes [40] to finite temperature EOSs [41, 42], magnetohydrodynamics [43–47], and neutrino cooling [41, 48, 49]. There are now some simulations that include all three of these improvements at once [50]. For our simulations, we use the BAM code in its newest version [36, 51, 52].

In this work, we present three different dynamical simulations. We consider a binary configuration with a mass ratio of  $q = 2.06$ , which is the largest mass ratio binary neutron star system ever evolved in full general relativity. This large mass ratio is particularly interesting, since the system undergoes mass transfer prior to merger and during the merger process a large amount of material gets unbound and is ejected from the system. The second example we consider is an unequal mass configuration, where the two neutron stars have spins misaligned with the orbital angular momentum; this is the first simulation of the merger of a precessing binary neutron star system. Here we find the same close relation between the precessing system (viewed in the nonprecessing frame) and the aligned-spin analogue found for binary black holes in previous studies (e.g., [53]). As a third test, we perform a simulation of an equal mass setup, with and without the eccentricity reduction procedure, where one can see a clear improvement in the waveform quality due to the eccentricity reduction procedure.

The article is structured as follows: In Sec. II, we re-

call the most important equations for our initial data construction and the general framework employed in SGRID. In Sec. III we describe the implementation and the numerical methods focusing on the recent upgrades to the code. We summarize the main results of our work in Sec. IV, where we compute binary neutron star (BNS) systems in quasi-equilibrium sequences varying the spin, eccentricity, mass ratio, and compactness and show convergence of the numerical method. In Sec. V, we evolve a  $q = 2.06$  nonspinning system, an unequal mass precessing configuration, and an equal-mass system with eccentricity reduction. We conclude in Sec. VI. The appendices summarize binary neutron star population synthesis predictions for more extreme systems, along with some issues in predicting the spins expected in binary neutron stars at merger; an alternative derivation of the CRV approach; and results from our study of single CRV-stars.

Throughout this work we use geometric units, setting  $c = G = M_\odot = 1$ , though we will sometimes include  $M_\odot$  explicitly or quote values in cgs units for better understanding. Spatial indices are denoted by Latin letters running from 1 to 3 and Greek letters are used for space-time indices running from 0 to 3. We always raise and lower indices with the physical metric (3-metric for spatial indices and 4-metric for spacetime indices). We shall also use index-free notation when convenient, denoting vectors (spatial or spacetime) using boldface.

## II. METHOD

The following section summarizes the fundamental framework of the initial data construction in SGRID. Since no new development was made in the evolution method in this work, we refer the reader to [36, 51, 52, 54] for details of the methods used in the BAM code.

### A. General Framework

In this article we investigate BNS systems in quasi-equilibrium. We construct such configurations with the help of a 3+1 decomposition of Einstein’s field equations [55]. In this section we recast important equations and derive the specific system of partial differential equations we solve.

We start writing the spacetime metric in the form

$$ds^2 = g_{\mu\nu} dx^\mu dx^\nu = -\alpha^2 dt^2 + \gamma_{ij} (dx^i + \beta^i dt)(dx^j + \beta^j dt), \quad (2.1)$$

where  $\alpha$  is the lapse function and  $\beta^i$  the shift. The spatial metric induced on 3-dimensional hypersurfaces of constant  $t$  is denoted by  $\gamma_{ij}$ . By performing the 3+1 decomposition, the field equations split into two sets, namely the Hamiltonian and momentum constraints,

$$R - K_{ij}K^{ij} + K^2 = 16\pi\rho, \quad (2.2a)$$

$$D_j (K^{ij} - \gamma^{ij}K) = 8\pi j^i, \quad (2.2b)$$

and the evolution equations

$$\partial_t \gamma_{ij} = -2\alpha K_{ij} + \mathcal{L}_\beta \gamma_{ij}, \quad (2.3a)$$

$$\begin{aligned} \partial_t K_{ij} = & \alpha(R_{ij} - 2K_{il}K^l_j + K K_{ij}) - D_i D_j \alpha \\ & + \mathcal{L}_\beta K_{ij} - 8\pi\alpha S_{ij} + 4\pi\alpha \gamma_{ij}(S - \rho). \end{aligned} \quad (2.3b)$$

Here the Ricci tensor  $R_{ij}$  and Ricci scalar  $R$  are computed from the spatial metric  $\gamma_{ij}$  with compatible covariant derivative operator  $D_i$ , and the extrinsic curvature  $K_{ij}$  is given by

$$K_{ij} = -\frac{1}{2\alpha}(\partial_t \gamma_{ij} - \mathcal{L}_\beta \gamma_{ij}), \quad (2.4)$$

where  $\mathcal{L}_\beta$  denotes the Lie derivative along the vector field  $\beta^i$ . We use  $K := \gamma^{ij}K_{ij}$ . The source terms (energy density, flux, and stress tensor) contained in the right hand side of the equations are

$$\rho := T_{\mu\nu} n^\mu n^\nu, \quad (2.5a)$$

$$j^i := -T_{\mu\nu} n^\mu \gamma^{\nu i}, \quad (2.5b)$$

$$S^{ij} := T_{\mu\nu} \gamma^{\mu i} \gamma^{\nu j}, \quad (2.5c)$$

where  $n^\mu$  is the normal vector to the hypersurface; we also write  $S := \gamma^{ij}S_{ij}$ . In this work we assume that the matter can be described as a perfect fluid with stress-energy tensor

$$T^{\mu\nu} = [\rho_0(1 + \epsilon) + p] u^\mu u^\nu + p g^{\mu\nu}, \quad (2.6)$$

where  $\rho_0$ ,  $\epsilon$ ,  $p$ , and  $u^\mu$  denote the mass density, the internal energy, the pressure, and the four-velocity of the fluid, respectively. Inserting (2.6) in the definition of  $\rho$ ,  $j^i$ , and  $S^{ij}$  [Eqs. (2.5a)–(2.5c)], one can obtain explicit expressions for the matter quantities entering the right-hand sides of the constraint and evolution equations in terms of the perfect fluid variables.

To ensure consistency, we have to solve the constraint equations along with the matter equation

$$\nabla_\nu T^{\mu\nu} = 0 \quad (2.7)$$

and the continuity equation

$$\nabla_\nu (\rho_0 u^\nu) = 0, \quad (2.8)$$

which comes from the conservation of the baryon number. Equation (2.7) can be written as the relativistic Euler equations

$$[\rho_0(1 + \epsilon) + p] u^\nu \nabla_\nu u^\mu = -(g^{\mu\nu} + u^\mu u^\nu) \nabla_\nu p. \quad (2.9)$$

In many cases it is useful to introduce the specific enthalpy

$$h = 1 + \epsilon + p/\rho_0. \quad (2.10)$$

Then the Euler equations can be written as

$$u^\nu \nabla_\nu (h u_\mu) + \nabla_\mu h = 0. \quad (2.11)$$

To further simplify the equations, we split the three-metric into a conformal factor  $\psi$  and the corresponding conformal metric  $\bar{\gamma}_{ij}$ , writing

$$\gamma_{ij} = \psi^4 \bar{\gamma}_{ij}. \quad (2.12)$$

Similarly, we express the extrinsic curvature in terms of a trace-free piece  $A_{ij}$ , writing

$$K_{ij} = A_{ij} + \frac{1}{3} \gamma_{ij} K. \quad (2.13)$$

Inserting (2.12) and (2.13) in the constraint equations gives their final general form before making any additional assumptions.

### 1. Assumptions for metric variables

In order to obtain a stationary configuration that is appropriate for initial data, we include additional assumptions which bring the entire system in an elliptic form. The first assumption is the existence of an approximate symmetry vector<sup>1</sup>

$$\mathbf{k} = \partial_t + g_x \partial_x + g_y \partial_y, \quad (2.14)$$

where the functions  $g_x$ ,  $g_y$  are chosen according to the problem we want to tackle, allowing us to construct quasircular, eccentric, and eccentricity-reduced configurations, as discussed in Sec. II B. Together with the existence of  $\mathbf{k}$  and the assumption

$$\mathcal{L}_\mathbf{k} g_{\mu\nu} = 0, \quad (2.15)$$

we assume spatial conformal flatness<sup>2</sup> and maximal slicing

$$\bar{\gamma}_{ij} = f_{ij}, \quad (2.16a)$$

$$K := \gamma_{ij} K^{ij} = 0, \quad (2.16b)$$

where  $f_{ij}$  denotes the flat metric which simplifies to  $\delta_{ij}$  in Cartesian coordinates. We preserve these conditions in time (at least infinitesimally), that is,  $\partial_t \bar{\gamma}_{ij} = \mathcal{L}_\mathbf{k} \bar{\gamma}_{ij} = 0$  and  $\partial_t K = \mathcal{L}_\mathbf{k} K = 0$ . Note that we have not used the assumption of an approximate symmetry vector in obtaining these last equalities, which is the usual approach, with conformal flatness and maximal slicing imposed afterwards, as discussed in Sec. III A of [17]. We also obtain

$$A^{ij} = \frac{1}{2\psi^4 \alpha} (\mathbf{L}\beta)^{ij}, \quad (2.17)$$

<sup>1</sup> Notice that in this work we employ a different notation than presented in [23, 24] where the Killing vector was denoted with  $\xi$ . We change our notation to emphasize that we assume a symmetry vector, not necessarily a helical Killing vector.

<sup>2</sup> See, e.g., Sec. III A in [17] for a discussion of the limitations of the conformal flatness assumption, but note that these caveats are quite mild for the systems we are considering. In particular, while the conformal flatness assumption is a significant obstruction to constructing high-spin binary black hole initial data (with dimensionless spin  $j \gtrsim 0.93$ ) as discussed in, e.g., [56], neutron stars cannot spin rapidly enough for this to be a problem. Specifically, neutron stars have maximum dimensionless spins of at most 0.7, except for strange quark stars, which can have dimensionless spins greater than 1; see, e.g., Figs. 3 and 6 in [57]. Since we are not considering strange quark stars in this work, we do not expect that the assumption of conformal flatness places any restrictions on the parameter space we can cover.



with  $(\mathbf{L}\beta)^{ij} = \bar{D}^i\beta^j + \bar{D}^j\beta^i - \frac{2}{3}\delta^{ij}\bar{D}_k\beta^k$ , where  $\bar{D}_i$  denotes the flat-space covariant derivative.

Finally, these assumptions lead to the following partial differential equations

$$\bar{D}^2\psi = -\frac{\psi^5}{32\alpha^2}(\mathbf{L}B)^{ij}(\mathbf{L}B)_{ij} - 2\pi\psi^5\rho \quad (2.18a)$$

$$\bar{D}_j(\mathbf{L}B)^{ij} = (\mathbf{L}B)^{ij}\bar{D}_j\ln\left(\frac{\alpha}{\psi^6}\right) + 16\pi\alpha\psi^4j^i \quad (2.18b)$$

$$\bar{D}^2(\alpha\psi) = \alpha\psi\left(\frac{7\psi^4}{32\alpha^2}(\mathbf{L}B)^{ij}(\mathbf{L}B)_{ij} + 2\pi\psi^4(\rho + 2S)\right), \quad (2.18c)$$

with  $\bar{D}_i = \partial_i$  in Cartesian coordinates and  $B^i = \beta^i + k^i + \Omega\epsilon_{ijl}(x^j - x_{\text{CM}}^j)a^l$ , where  $x_{\text{CM}}^j$  is the center of mass,  $\Omega$  the orbital frequency,  $\epsilon_{ijl}$  is the Levi-Civita symbol, and  $a^l$  is a unit vector pointing along the direction of the orbital angular momentum.

## 2. Assumptions for matter variables

Similarly to the metric variables, we also need to make assumptions for the matter fields. These assumptions are discussed in more detail in [17, 23] and briefly described below. We start by splitting the four-velocity into a piece along  $k^\mu$ , and one orthogonal to it, which we call  $V^\mu$ . Specifically, we write

$$u^\mu = u^0(k^\mu + V^\mu), \quad (2.19)$$

with  $u^0 = -u^\nu n_\nu/\alpha$ . Next we define

$$p_\mu = hu_\mu. \quad (2.20)$$

While we can assume that  $\mathcal{L}_k p_\mu = 0$  for irrotational binaries, this equation is, in general, not satisfied for spinning neutron stars—see appendix A of [23]. Thus, we introduce the canonical momentum 1-form of a fluid element

$$p_i = \gamma_i^\mu p_\mu \quad (2.21)$$

and split  $p_i$  into an irrotational part which can be written as the gradient of a potential,  $D_i\phi$ , and a rotational part  $w_i$ :

$$p_i = D_i\phi + w_i \quad (2.22)$$

or equivalently in four-dimensions

$$p_\mu = \nabla_\mu\phi + w_\mu. \quad (2.23)$$

Although  $\mathcal{L}_k p_\mu \neq 0$ , we assume

$$\mathcal{L}_k(\rho u^0) = 0, \quad (2.24a)$$

$$\gamma_i^\mu \mathcal{L}_k(\nabla_\mu\phi) = 0, \quad (2.24b)$$

$$\gamma_i^\mu \mathcal{L}_{\bar{k}} w_\mu = 0, \quad (2.24c)$$

with

$$\bar{k}^\mu := \frac{\nabla^\mu\phi}{hu^0} =: k^\mu - \Delta k^\mu, \quad (2.25)$$

which is parallel to the worldline of the star's center. At this point useful relations can be derived immediately,

$$\begin{aligned} \gamma_i^\nu \mathcal{L}_k p_\nu &\stackrel{(2.24b)}{=} \gamma_i^\nu \mathcal{L}_k w_\nu = \gamma_i^\nu \mathcal{L}_{\bar{k} + \Delta k} w_\nu \\ &\stackrel{(2.24c)}{=} \gamma_i^\nu \mathcal{L}_{\Delta k} w_\nu = {}^{(3)}\mathcal{L}_{\Delta \bar{k}} w_\nu, \end{aligned} \quad (2.26a)$$

$$V^i + \Delta \bar{k}^i \stackrel{(2.19)}{=} \frac{u^i}{u^0} - k^i + \Delta k^i = \frac{u^i}{u^0} - \bar{k}^i \stackrel{(2.22)}{=} \frac{w^i}{hu^0} \quad (2.26b)$$

with the three-dimensional Lie derivative  ${}^{(3)}\mathcal{L}$  and  $\Delta k^\mu = (0, \Delta \bar{k}^i)$ . Additionally, from the fact that  $hu^0$  and  $\gamma_{ij}$  are approximately constant along  $\frac{w^i}{hu^0}$  we obtain

$${}^{(3)}\mathcal{L}_{V + \Delta \bar{k}} w_i = \frac{w_i}{hu^0} {}^{(3)}\mathcal{L}_{\frac{w}{hu^0}} hu^0 + w^j {}^{(3)}\mathcal{L}_{\frac{w}{hu^0}} \gamma_{ij} \approx 0. \quad (2.27)$$

Plugging (2.19) into the continuity equation (2.8) and using (2.15), (2.24a) we get

$$D_i(\rho_0 \alpha u^0 V^i) = 0. \quad (2.28)$$

Similarly, the Euler equation (2.9) together with (2.26a), (2.26b), and (2.27) can be simplified to

$$D_i\left(\frac{h}{u^0} + V^j D_j\phi\right) = 0, \quad (2.29)$$

which can be integrated to obtain

$$\frac{h}{u^0} + V^j D_j\phi = -C = \text{const.} \quad (2.30)$$

Note that a simple derivation of this first integral, which makes use of the Cartan identity, can be found in Appendix B.

The constant  $C$  is chosen during the numerical iteration process in such a way that the baryonic mass of each star stays constant; see Sec. III.

In general the velocity is given by

$$V^i = \frac{D^i\phi + w^i}{hu^0} - (\beta^i + k^i), \quad (2.31)$$

which brings the continuity equation in the form

$$D_i\left[\frac{\rho_0\alpha}{h}(D^i\phi + w^i) - \rho_0\alpha u^0(\beta^i + k^i)\right] = 0. \quad (2.32)$$

This equation can be seen as a nonlinear elliptic equation in  $\phi$  and especially needs known boundaries at the star's surface to be solved. To handle this issue we introduce surface-fitted coordinates in the subsequent section.

Integrating and using  $u^\mu u_\mu = -1$  leads to

$$h = \sqrt{L^2 - (D_i\phi + w_i)(D^i\phi + w^i)}, \quad (2.33)$$

with

$$L^2 = \frac{b + \sqrt{b^2 - 4\alpha^4[(D_i\phi + w_i)w^i]^2}}{2\alpha^2}, \quad (2.34a)$$

$$b = [(k^i + \beta^i)D_i\phi - C]^2 + 2\alpha^2(D_i\phi + w_i)w^i. \quad (2.34b)$$

For the data constructed with the CRV-approach we choose throughout the entire paper

$$w^i = \epsilon^{ijk}\omega^j(x^k - x_{C*}^k), \quad (2.35)$$

where  $x_{C*}^i$  gives the coordinate position of the center of the star and  $\omega^i$  is an arbitrary angular velocity vector.

## B. Specifying the symmetry vector

Helical Killing vectors are well known and commonly used constructs in numerical relativity to construct binaries on circular orbits that are stationary in a corotating frame. The general expression for these vectors is given by

$$k_{\text{qc}}^\alpha = t^\alpha + \Omega_{\text{qc}} \varphi^\alpha = t^\alpha + \Omega_{\text{qc}} (xy^\alpha - yx^\alpha), \quad (2.36)$$

where we used the vectors  $\mathbf{t} = \partial_t$ ,  $\mathbf{x} = \partial_x$ ,  $\mathbf{y} = \partial_y$  and  $\varphi = \partial_\varphi$  that generate translations in the  $t$ ,  $x$ , and  $y$  directions, respectively, and rotations in the  $\varphi$  direction. In [17], we showed how to generalize this vector to incorporate eccentricity as well as radial velocity. However, because our initial numerical implementation of the method used a Cartesian grid, without the surface-fitted coordinates needed to solve for the velocity potential, we settled on a constant fluid-velocity approximation instead of solving Eq. (2.32). We are now able to solve the full set of equations for the first time. In the following, we will briefly summarize how we generalize the standard approximate helical Killing vector to an approximate helical symmetry vector that incorporates radial velocity and eccentricity.

To find a vector  $k^\alpha$  that approximately Lie-derives the flow we make the following two assumptions: (i) Such a  $k^\alpha$  exists. (ii)  $k^\alpha$  is along the motion of the star center.

In order to describe eccentric orbits we make the additional assumption that (iii) each star center moves along a segment of an elliptic orbit at apoapsis. Since we only need a small segment of an orbit near apoapsis, we will approximate this segment by the circle inscribed into the elliptical orbit there. Then the radii of the inscribed circles are

$$r_{c1,2} = (1 - e)d_{1,2}, \quad (2.37)$$

where  $d_1$  and  $d_2$  are the distances of the particles from the center of mass at apoapsis and  $e$  is the eccentricity parameter for the elliptic orbit [17]. These two inscribed circles are not centered on the center of mass, but on the points

$$x_{c1,2} = x_{1,2} \mp r_{c1,2} = x_{\text{CM}} + e(x_{1,2} - x_{\text{CM}}), \quad (2.38)$$

where we have used  $d_{1,2} = |x_{1,2} - x_{\text{CM}}|$  and assumed that apoapsis occurs on the  $x$ -axis. (The upper and lower signs correspond to the subscripts 1 and 2, respectively.) Assumption (ii) then tells us that the approximate Killing vector for elliptic orbits must have the form

$$k_{\text{ecc1,2}}^\alpha = t^\alpha + \Omega [(x - x_{c1,2})y^\alpha - yx^\alpha] \quad (2.39)$$

near each star [17].

The next step is to allow a slow inspiral of the orbit due to energy loss because of GW emission. This means the orbital velocity will have a small radial component in the direction of the center of mass. Assumption (ii) then tells us that assumption (iii) above needs to be modified to include a radial piece. We assume that the approximate Killing vector now is

$$k_{1,2}^\alpha = k_{\text{ecc1,2}}^\alpha + \frac{v_r}{r_{12}} r^\alpha = t^\alpha + \Omega [(x - x_{c1,2})y^\alpha - yx^\alpha] + \frac{v_r}{r_{12}} r^\alpha, \quad (2.40)$$

which we also refer to as a *heliptical approximate* symmetry vector. Here  $r^\alpha = (0, x, y, z)$  points in the radial direction,  $r_{12} = |x_1 - x_2|$  is the distance between the star centers, and  $v_r$  is a radial velocity parameter. The radial velocity  $v_r$  could be chosen corresponding to the radial velocity of an inspiralling binary from post-Newtonian calculations, or it can be obtained from an iterative procedure aimed at reducing the orbital eccentricity such as the one described in Sec. IV C. In this case we also have to adjust the eccentricity parameter  $e$  that appears in  $x_{c1,2}$ . The reason is that changing  $e$  amounts to changing the tangential orbital velocity, which is needed when we want non-eccentric inspiral orbits.

To have a more physical quantity that will be useful for comparisons, we consider the mean motion, as in [17]:

$$\bar{\Omega} = 2\pi/T = \Omega(1 + e)\sqrt{1 - e^2}, \quad (2.41)$$

where  $T$  is the orbital period.

## III. CODE DESCRIPTION

To construct initial data with SGRID we use the numerical framework described in [22, 24]. In this section we recall important aspects to give an almost complete picture. In particular, we describe the grid configuration, the iteration procedure, and recent changes which allow us to use more realistic EOS and also compute configurations with a relatively large mass ratio. A short discussion about the BAM code will be given in Sec. V.

### A. Grid configuration

We place the neutron stars along the  $x$ -axis. Figure 1 illustrates the part of the computational domain with  $y > 0$ ,  $z = 0$ . The entire grid is built out of six individual domains. The grid configuration is not fixed and changes during the computation in response to changes in the positions of the stars' surfaces.

We follow the approach of [22, 58] and express Cartesian coordinates as

$$x = \frac{b}{2} \left( \frac{1}{(X^2 + R^2)^2} + 1 \right) (X^2 - R^2), \quad (3.1a)$$

$$y = b \left( \frac{1}{(X^2 + R^2)^2} - 1 \right) XR \cos(\varphi), \quad (3.1b)$$

$$z = b \left( \frac{1}{(X^2 + R^2)^2} + 1 \right) XR \sin(\varphi), \quad (3.1c)$$

with  $X \in [0, 1]$ ,  $R \in [0, \sqrt{1 - X^2}]$ ,  $\varphi \in [0, 2\pi)$ . Furthermore, we transform to coordinates  $A, B, \varphi$  for the different domains. The domains covering the exterior of the stars and including spatial infinity  $(A, B) = (1, 0)$  employ

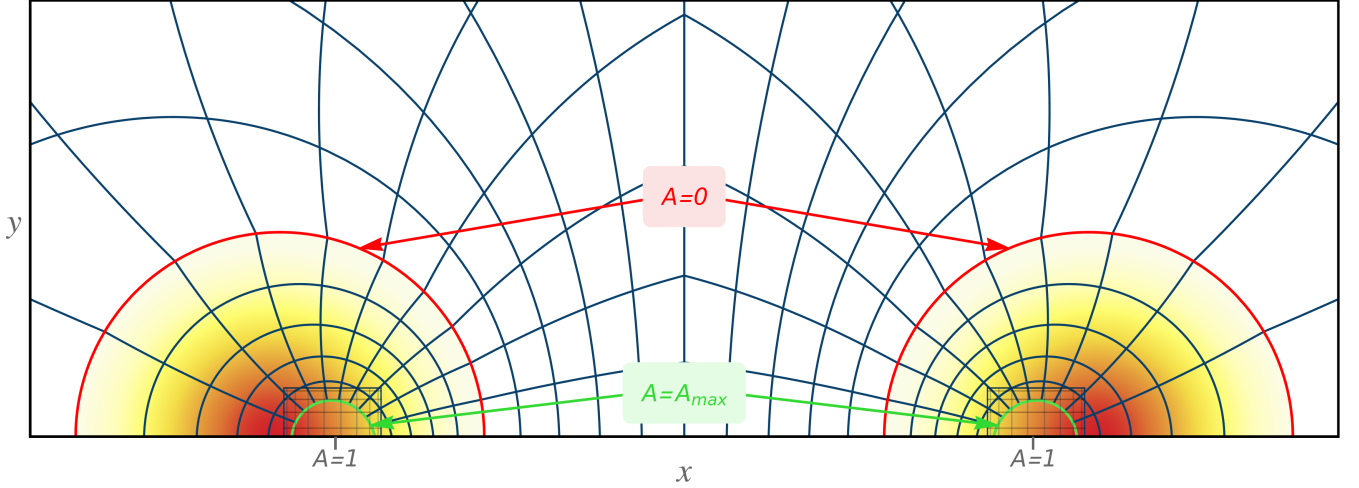


FIG. 1: The grid structure in the  $xy$ -plane for an equal-mass configuration. One can see lines of constant  $A$  and  $B$  (dark blue lines) for  $b = 16, \sigma_+ = -\sigma_- = 1.304$  and  $A_{\max} = 0.5$  with an overlay of the density profile of the cross section. Moreover one can see the Cartesian boxes with Chebychev grids inside the stars.

$$X = (1 - A) [\operatorname{Re}(C_{\pm}(B, \varphi)) - B \operatorname{Re}(C_{\pm}(1, \varphi))] + B \cos \left( \frac{A\pi}{4} + (1 - A) \arg(C_{\pm}(1, \varphi)) \right), \quad (3.2a)$$

$$R = (1 - A) [\operatorname{Im}(C_{\pm}(B, \varphi)) - B \operatorname{Im}(C_{\pm}(1, \varphi))] + B \sin \left( \frac{A\pi}{4} + (1 - A) \arg(C_{\pm}(1, \varphi)) \right). \quad (3.2b)$$

Since spatial infinity is included in our domain, we can impose exact Dirichlet boundary conditions:

$$\lim_{r \rightarrow \infty} \psi = 1, \quad (3.3a)$$

$$\lim_{r \rightarrow \infty} B^i = 0, \quad (3.3b)$$

$$\lim_{r \rightarrow \infty} \alpha \psi = 1, \quad (3.3c)$$

where  $r$  denotes the coordinate distance from the origin.

The inner domain boundary  $A = 0$  is the star's surface, with

$$C_{\pm}(B, \varphi) = \sqrt{\tanh \left( \frac{\sigma_{\pm}(B, \varphi) + i\pi B}{4} \right)}, \quad (3.4)$$

where  $\sigma_{\pm}$  is a function that determines the shape of the star's surface, and  $\pm$  denotes the sign of the  $x$ -coordinate, i.e., the left or the right star. At each star's surface Eq. (2.32) is subject to the boundary conditions

$$[(D^i + w^i \phi) - hu^0(\beta^i + k^i)] D_i \rho = 0. \quad (3.5)$$

The coordinate transformations inside the stars are

$$X = (1 - A) [\operatorname{Re}(C_{\pm}(B, \varphi)) - B \operatorname{Re}(C_{\pm}(1, \varphi))] + B \cos(D_{\pm}) + \delta_{\pm}(1 - B)A, \quad (3.6a)$$

$$R = (1 - A) [\operatorname{Im}(C_{\pm}(B, \varphi)) - B \operatorname{Im}(C_{\pm}(1, \varphi))] + B \sin(D_{\pm}) + \delta_{\mp}(1 - B)A, \quad (3.6b)$$

with

$$D_{\pm} := (1 - A) \arg(C_{\pm}(1, \varphi)) + \delta_{\mp} \frac{\pi}{2} A, \quad (3.7)$$

where  $\delta_{\pm} = 1$  for the star with  $x > 0$  and is zero for the other, and vice versa for  $\delta_{\mp}$ . Unfortunately, the transformation to  $(A, B, \varphi)$  coordinates is singular for  $A = 1$  (i.e., at the star's center). To cure this problem, we cover the center by a Cartesian box with grid points at

$$x^i_k = \frac{x^i_{\min} - x^i_{\max}}{2} \cos \left( \frac{k\pi}{n^i - 1} \right) + \frac{x^i_{\min} + x^i_{\max}}{2}, \quad (3.8)$$

where  $x^i = (x, y, z)$ , with  $0 \leq k < n_{\text{Cart}}$ . The Cartesian boxes cover a region for  $A > A_{\max}$ . The choice of  $A_{\max}$  allows us to specify the clustering of the grid points. For large  $A_{\max}$  the Cartesian box is smaller, while for small  $A_{\max}$  the box is larger. Thus, introducing a small  $A_{\max}$  increases the resolution in the outer region of the stars. This will be important when piecewise polytropes are employed, where it is crucial to resolve the crust with a sufficient number of grid points. The collocation points in the other regions of the grid are

$$A_i = \frac{A_{\max}}{2} \left[ 1 - \cos \left( \frac{\pi i}{n_A - 1} \right) \right], \quad (3.9a)$$

$$B_j = \frac{1}{2} \left[ 1 - \cos \left( \frac{\pi j}{n_B - 1} \right) \right], \quad (3.9b)$$

$$\varphi_k = \frac{2\pi k}{n_{\varphi}}, \quad (3.9c)$$

with  $0 \leq i < n_A$ ,  $0 \leq j < n_B$ ,  $0 \leq \varphi < n_{\varphi}$ . In the  $A, B$ -directions we use Chebyshev polynomials, while for the  $\varphi$ -direction a Fourier expansion is used. For a typical configuration, we employ between 20 and 28 points in  $A, B$  and 8 points in the  $\varphi$ -direction. The Cartesian box is covered with  $n_x = n_y = n_z = n_{\text{Cart}} = 16, \dots, 24$  points, where typically we choose  $n_{\text{Cart}} = n_A - 4$ .

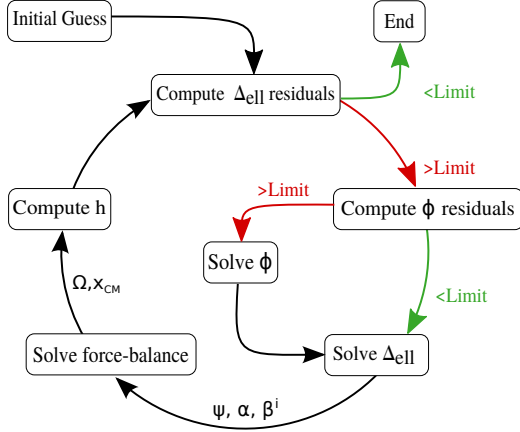


FIG. 2: Iteration scheme as outlined in the text.

Finally, some regularity conditions along the  $x$ -axis have to be imposed: In the domains where  $(A, B, \varphi)$ -coordinates are employed, we set

$$\partial_\varphi F = 0, \quad (3.10a)$$

$$\partial_s F + \partial_s \partial_\varphi \partial_\varphi F = 0, \quad (3.10b)$$

with  $F \in \{\psi, B^i, \alpha, \phi\}$  and  $s := \sqrt{y^2 + z^2}$ .

### B. Iteration procedure

To solve the coupled system of partial differential equations we perform a specific iteration procedure first introduced and described in detail in [24]. The scheme is sketched in Fig. 2 and we describe it in detail in the following:

(i) We start with an initial guess. This guess can be obtained by solving the Tolman-Oppenheimer-Volkoff (TOV) [59, 60] equation (and superposing, if we are considering a binary) or given by a previously constructed configuration. The velocity potential  $\phi$  in each star is set to  $\phi = \Omega(x_{C*} - x_{CM})y$ , where  $x_{C*}$  is the  $x$ -coordinate of the star's center (this initial guess corresponds to a spatially constant velocity field and is exact for rigidly rotating nonrelativistic stars).

(ii) In the second step we evaluate the residuals of all elliptic equations (denoted by  $\Delta_{\text{ell}}$  in Fig. 2) and stop if these residuals are below the prescribed tolerance.

(iii) If the residual of Eq. (2.32) is bigger than the combined residuals of Eqs. (2.18), we solve (2.32) for  $\phi$  and use a softening procedure  $\phi = \zeta \phi_{\text{solved}} + (1 - \zeta) \phi_{\text{old}}$ , where for this iteration procedure  $\zeta = 0.2$  is applied.

(iv) We solve the elliptic equations for  $\psi, B^i, \alpha$  (2.18) with a softening of  $\zeta = 0.4$ .

(v) The positions of the stars' centers,  $x_{C*, \pm}$ , are determined by the maximum of  $h$  along the  $x$ -axis. We determine  $\Omega$  and  $x_{CM}$  with the help of the force balance

equation (3.16); see III C 2 for more details.

(vi) We then compute  $h$  and choose  $C_\pm$  such that the baryonic mass of each star remains constant. Afterwards, we update  $\sigma_\pm$  to reflect the changes in the shape of the stars' surfaces and adjust the domain boundaries accordingly. In most cases we filter out high frequencies in  $\sigma_\pm$  for overall stability and apply  $\partial_B \sigma_\pm(B, \varphi)|_{B=0,1} = 0$  to keep the stars on the  $x$ -axis.

(vii) We go back to step (ii).

### C. Code Improvements

#### 1. Including piecewise polytropes

In order to easily incorporate more realistic equations of state we follow the approach in [61] and approximate them by piecewise polytropic equations of state.

For a simple polytropic equation of state (EOS), with  $p = \kappa \rho_0^\Gamma$  (where  $\Gamma = 1 + 1/n$ ), the matter-variables inside the star are  $C^\infty$  and only the star's surface needs special attention. However, this is no longer the case when dealing with piecewise polytropes.

For a polytrope with polytropic index  $n_I$  and constant  $\kappa_I$ , the pressure  $p$ , specific enthalpy  $h$ , and energy density  $\rho_E$  are related to the rest mass or baryonic mass density  $\rho_0$  via

$$p = \kappa_I \rho_0^{1+1/n_I}, \quad (3.11a)$$

$$h = (n_I + 1) \kappa_I \rho_0^{1/n_I} + K_I, \quad (3.11b)$$

$$\rho_E = (n_I \kappa_I \rho_0^{1/n_I} + K_I) \rho_0, \quad (3.11c)$$

where  $K_I$  is a constant that determines the specific enthalpy at the star surface. For piecewise polytropic EOSs we divide the range of possible  $\rho_0$  into intervals  $[0, \rho_{0,1}]$ ,  $[\rho_{0,1}, \rho_{0,2}]$ , etc. We label the intervals by  $I = 0, 1, \dots$ . Within each interval  $I$  we use the polytropic relations of Eq. (3.11a), but with a different  $n_I$ ,  $\kappa_I$  and  $K_I$ . In interval 0 we must choose  $K_0 = 1$  to ensure that the specific enthalpy is unity at the star surface. We can freely choose all the  $n_I$  and  $\kappa_0$  to closely approximate some desired EOS. However, in order to assure continuity of  $p$ ,  $h$  and  $\rho_E$  across interval boundaries the remaining  $\kappa_I$  and  $K_I$  must be related by

$$\kappa_I = \kappa_{I-1} \rho_{0,I}^{1/n_{I-1} - 1/n_I}, \quad (3.12a)$$

$$K_0 = 1, \quad (3.12b)$$

$$K_I = K_{I-1} + n_{I-1} \kappa_{I-1} \rho_{0,I}^{1/n_{I-1}} - n_I \kappa_I \rho_{0,I}^{1/n_I} \quad (3.12c)$$

In this case we only know that all the matter variables are at least  $C^0$  (i.e., continuous), but not necessarily differentiable.<sup>3</sup> We use the parameters presented in [61]

<sup>3</sup> We have not used the spectral fits to realistic equations of state from [62], even though these would give  $C^\infty$  matter variables

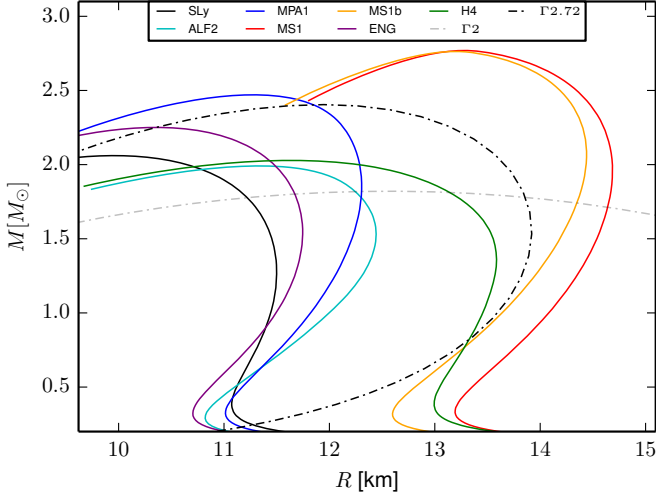


FIG. 3: The mass-radius relation for the EOSs employed in this work. See Table I for further details.

and employ four different pieces consisting of a crust and three inner regions. All piecewise polytropic EOSs we use give a maximum mass of  $M_{\max} \geq 1.99M_{\odot}$  (so they are  $1\sigma$  compatible with the precise high-mass neutron star measurements in [63, 64]), and have an adiabatic sound speed  $c_s \leq 1$  for densities up to the maximum density of a stable TOV star. These EOSs also span a range of microphysical content, including hyperons (H4) and the hadron-quark mixed phase (ALF2), as well as the standard  $npe\mu$  composition, and were obtained using a variety of calculational methods (see Sec. II in [61] for further details). Important parameters for the EOSs we employ are given in Tab. I and the mass-radius relations for TOV stars are shown in Fig. 3. Additionally, we use two simple polytropic EOS, one ( $\Gamma_2$ ) with  $\kappa = 123.6489$  and  $\Gamma = 2$  and one ( $\Gamma_{2.72}$ ) with  $\kappa = 23841.43$  and  $\Gamma = 2.7203$ . The latter EOS is constructed as an “average fit” to certain of the realistic EOSs we consider, where we have fitted  $p(\rho_0) = \sum_{i \in S} p_i(\rho_0)/6$  for the six EOS  $S = (\text{SLy}, \text{ALF2}, \text{MPA1}, \text{MS1}, \text{MS1b}, \text{ENG})$  with a simple polytropic EOS in the density interval  $\rho_0 \in [0, 3.24 \times 10^{-3}]$ . The resulting EOS tends to be more “realistic” than the  $\Gamma_2$  polytrope widely used in the literature. In particular, it allows a maximum mass  $> 2M_{\odot}$  and has a maximum adiabatic sound speed  $< 1$  for the maximum mass TOV star. The overall qualitative behavior of its mass-radius curve is also more similar to those of realistic EOSs than that of the  $\Gamma_2$  EOS (see Fig. 3).

In the past, SGRID used  $\bar{q} := p/\rho_0$  as the fundamental variable, i.e., the matter variables and their spatial derivatives were all derived from  $\bar{q}$ . But with this definition  $\bar{q}$  will only be  $C^0$  in case of a piecewise polytropic EOS, even for a single TOV star. In contrast,  $h$ , which

TABLE I: Properties of the equations of state (EOSs) used in this work. The first seven rows refer to piecewise polytropes, where we employ the fits of [61]. These EOS use a crust with  $\kappa_{\text{crust}} = \kappa_0 = 8.948185 \times 10^{-2}$  and  $\Gamma_{\text{crust}} = 1 + 1/n_0 = 1.35692$ . The divisions for the individual parts are at  $\rho_{0,1} = \rho_{\text{crust}}$ ,  $\rho_{0,2} = 8.12123 \times 10^{-4}$  and  $\rho_{0,3} = 1.62040 \times 10^{-3}$ . The last two rows refer to simple polytropic EOSs. The columns (for the piecewise polytropes) refer to: the name of the EOS, the maximum density in the crust, the three polytropic exponents  $\Gamma_I = 1 + 1/n_I$  for the individual pieces, and the maximum supported gravitational mass  $M^{\max}$ , maximum baryonic mass  $M_b^{\max}$ , and maximum compactness  $C^{\max}$ , respectively, of an isolated nonrotating star. [We define the compactness by  $C := M/R$ , where  $R$  is the star’s radius (in Schwarzschild coordinates) and  $M$  is its gravitational mass.] For the simple polytropes we present  $\Gamma$  and  $\kappa$ , in addition to the same maximum values for an isolated nonrotating star given for the piecewise polytropes.

EOS	$\rho_{\text{crust}} \cdot 10^4$	$\Gamma_1$	$\Gamma_2$	$\Gamma_3$	$M^{\max}$	$M_b^{\max}$	$C^{\max}$
SLy	2.36953	3.005	2.988	2.851	2.06	2.46	0.31
ALF2	3.15606	4.070	2.411	1.890	1.99	2.32	0.26
ENG	2.99450	3.514	3.130	3.168	2.25	2.73	0.32
H4	1.43830	2.909	2.246	2.144	2.03	2.33	0.26
MPA1	2.71930	3.446	3.572	2.887	2.47	3.04	0.32
MS1	1.52594	3.224	3.033	1.325	2.77	3.35	0.31
MS1b	1.84169	3.456	3.011	1.425	2.76	3.35	0.31
$\Gamma_2$	$\Gamma = 2, \quad \kappa = 123.6489$				1.82	2.00	0.21
$\Gamma_{2.72}$	$\Gamma = 2.7203, \quad \kappa = 23841.43$				2.40	2.85	0.30

is given by

$$\frac{dh}{dr} = -\frac{h[m(r) + 4\pi r^2 p]}{r[r - 2m(r)]} \quad (3.13)$$

for a single TOV star, will be at least  $C^1$  inside the star under the assumption that  $p, \rho_0 \in C^0$ . [Here  $m(r) := 4\pi \int_0^r \rho_0(\bar{r}) \bar{r}^2 d\bar{r}$ , so  $m \in C^1$ .] For this reason we have switched variables to

$$q := h - 1, \quad (3.14)$$

which is at least  $C^1$  for single TOV stars. Taking spatial derivatives of  $q$  is thus more accurate than taking them of  $p/\rho_0$ .

We can compute the other matter variables in terms of  $q$ , giving

$$\rho_0 = \left[ \frac{q + 1 - K_I}{\kappa_I(n_I + 1)} \right]^{n_I}, \quad (3.15a)$$

$$p = \rho_0 \frac{q + 1 - K_I}{n_I + 1}, \quad (3.15b)$$

$$\rho_E = n_I p + K_I \rho_0. \quad (3.15c)$$

## 2. Updating $\Omega$ and $x_{CM}^1$

In order to also solve Eq. (2.33) we need to know the values of  $\Omega$  and  $x_{CM}^1$ . We first determine the star centers

inside the star, since we need to have the same implementation of the EOS as in the BAM code that we use for evolutions: Slight differences between the two fits to a given EOS would lead to unphysical effects upon starting the evolution.

$x_{C*\pm}^1$  by finding the maximum of the current  $h$  along the  $x$ -axis. Using  $\partial_1 h|_{x_{C*\pm}^1} = 0$  in Eq. (2.33) we find [24]

$$\partial_1 \ln \left[ \alpha^2 - \left( \beta^i + k^i + \frac{w^i}{hu^0} \right) \left( \beta_i + k_i + \frac{w_i}{hu^0} \right) \right] \Big|_{x_{C*\pm}^1} = -2\partial_1 \ln \Gamma \Big|_{x_{C*\pm}^1} \quad (3.16)$$

Note that  $\beta^i + k^i$  is a function of  $\Omega$  and  $x_{CM}^1$ . The right hand side of Eq. (3.16) is given by

$$\Gamma = \frac{\alpha u^0 \left[ 1 - \left( \beta^i + k^i + \frac{w^i}{hu^0} \right) \frac{D_i \phi}{\alpha^2 hu^0} - \frac{w_i w^i}{(\alpha hu^0)^2} \right]}{\sqrt{1 - \left( \beta^i + k^i + \frac{w^i}{hu^0} \right) \left( \beta_i + k_i + \frac{w_i}{hu^0} \right) \frac{1}{\alpha^2}}}, \quad (3.17)$$

which we reproduce here (with  $\xi^i$  replaced by  $k^i$ ) because there were some typos in the original published version in [24]. Eq. (3.16) is called force balance equation. It gives one equation for  $\Omega$  and  $x_{CM}^1$  at each star center and thus can be used to update  $\Omega$  and  $x_{CM}^1$ . One noteworthy caveat is that we evaluate the derivative of  $\ln \Gamma$  in Eq. (3.16) for the  $\Omega$  and  $x_{CM}^1$  before the update.

We have found that the force balance equation works well in many cases. However, for more massive stars or higher mass ratios the overall iteration can become unstable. In this case the center of mass drifts away and the magnitude of the Arnowitt-Deser-Misner (ADM) momentum

$$P_{ADM}^i = \int j^i \psi^{10} d^3x, \quad (3.18)$$

especially of its  $y$ -component  $P_{ADM}^y$  becomes large. This problem has also been observed by others [37]. It can be solved in part by computing  $\Omega$  and  $x_{CM}^1$  in a different way: Notice first that the matter flux

$$j^i = \alpha(\rho_E + p)(u^0)^2(V^i + k^i + \beta^i) \quad (3.19)$$

in Eq. (3.18) depends on the Killing vector  $k^\mu$  and thus on  $\Omega$  and  $x_{CM}^1$ . Using the  $\Omega$  from the previous iteration we can then solve the equation  $P_{ADM}^y = 0$  for  $x_{CM}^1$ . This gives a value for the center of mass such that the  $P_{ADM}^y$  will be zero as desired. Once we have determined  $x_{CM}^1$  in this way, we next compute  $\Omega$  from Eq. (3.16) for each star's center. This will in general give two different values for  $\Omega$ . For the final  $\Omega$  we simply use the average of these two values.

#### IV. BINARY NEUTRON STARS IN QUASI-EQUILIBRIUM

In the following, we discuss the main results on equilibrium configurations obtained by applying the framework and code improvements discussed in Sec. II and Sec. III. In particular we analyze the spin-orbit (SO) interaction for realistic EOSs; we extend the work of [17] on highly eccentric orbits, where we improve our data by solving Eq. (2.32) for the velocity potential; we investigate inspirals on eccentricity reduced orbits; we also present significantly unequal mass setups as well as configurations with high compactnesses; we end with a convergence study.

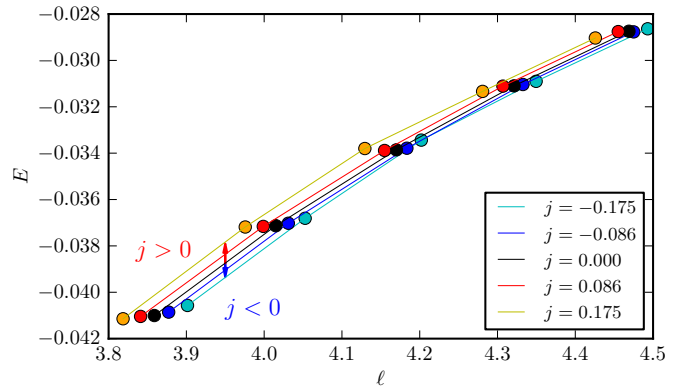


FIG. 4: Reduced binding energy vs. specific total angular momentum for a binary system with  $M_b^A = M_b^B = 1.4895$  and the SLy EOS. The influence of aligned and antialigned spin is shown with arrows

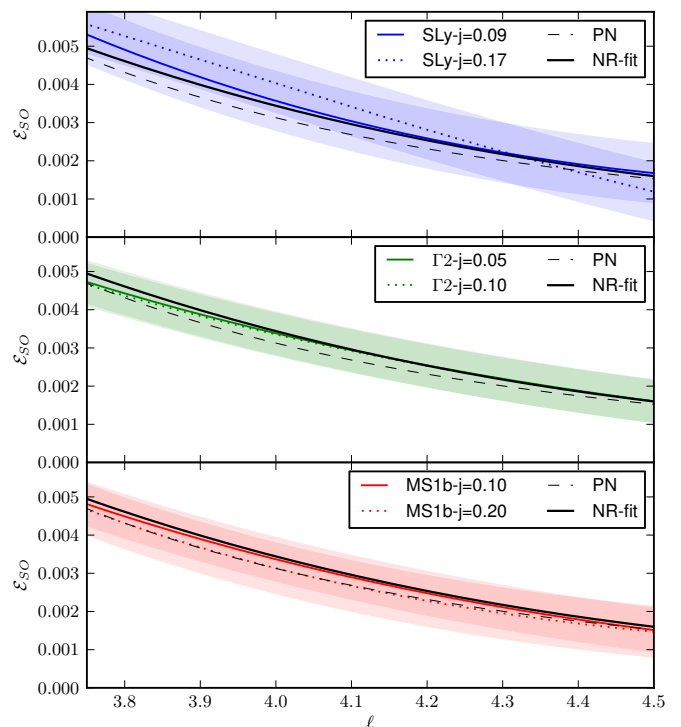


FIG. 5: The spin-orbit coefficient  $\mathcal{E}_{SO}$  in the reduced binding energy of the binary neutron stars. We compare numerical results for the SLy (top panel),  $\Gamma 2$  (middle panel), and MS1b (bottom panel) EOSs with the predictions of the post-Newtonian (PN) approximation (black dashed lines). We also include an average line for our data in all panels (solid black lines). We estimate the numerical error bars from computations at different resolutions and show them as shaded regions.

##### A. Spins

To date, there exist three ways to model the fluid velocity field in quasi-equilibrium BNS configurations in general relativity. Neutron star spins are neglected in the irrotational approach, while they are treated in an unphysical manner if corotation is assumed. The CRV approach [23, 24] (see also [38]) is the only known alternative for the construction of consistent and constraint



solved initial data where spins are included and can be chosen freely. Alternative approaches have been proposed and employed in dynamical evolutions [31–33], but they are based on constraint-violating data which also violate hydrodynamical stationarity conditions. Here we discuss some properties of equilibrium sequences of CRV BNS expanding the work of [38], and focusing on the spin-orbit interaction.

We compute equilibrium sequences for the SLy and MS1b EOSs (Table I), setting the baryonic masses of the individual neutron stars to  $M_b = 1.48945$ . Additionally, we use results of [38], where the  $\Gamma 2$  EOS was employed and the baryonic mass of the neutron stars was set to  $M_b = 1.625$ . For each of these EOSs we obtain sequences at fixed baryonic mass and for five different spin magnitudes, two aligned spin setups ( $\uparrow\uparrow$ ), one irrotational (00), and two anti-aligned setups ( $\downarrow\downarrow$ ). Each sequence essentially mimics an adiabatic evolution. (In the aligned and anti-aligned cases we are considering, the spin directions remain unchanged during an evolution.) The resolution employed for the piecewise polytropes is  $n_A = n_B = 28$ ;  $n_\varphi = 8$ ,  $n_{\text{Cart}} = 24$ , while for the  $\Gamma 2$  simple polytrope it is  $n_A = n_B = 24$ ,  $n_\varphi = 8$ ,  $n_{\text{Cart}} = 20$ . We use a higher resolution for the piecewise polytropic runs to better resolve the crust region (cf. Table I and Sec. IV F).

We stress that an unambiguous definition of the individual spins of the stars in a binary system is in general not possible. It is however possible to define the spin of single isolated neutron stars within the CRV approach, as discussed in Appendix C. Using this result, one can give an estimate of the magnitudes of the spins of the stars in a binary by considering, for each star, an isolated configuration with the same baryonic mass  $M_b$  and the same rotational part of the 4-velocity  $w^\mu$ , and assuming that the individual spin magnitudes  $S^A$ ,  $S^B$  remain unchanged when we use the same parameters to compute binary initial data.

We analyze equilibrium sequences in terms of the reduced binding energy

$$E = \frac{1}{\nu} \left( \frac{M_{\text{ADM}}}{M} - 1 \right), \quad (4.1)$$

and the specific orbital angular momentum

$$\ell = \frac{L}{\nu M^2} = \frac{J_{\text{ADM}} - S^A - S^B}{\nu M^2}. \quad (4.2)$$

Here  $\nu := M^A M^B / M^2$  is the symmetric mass ratio,  $M^A$  and  $M^B$  are the individual masses of the stars in isolation,  $M := M^A + M^B$ ,<sup>4</sup> and  $M_{\text{ADM}}$  and  $J_{\text{ADM}}$  are the binary's ADM mass and angular momentum, respectively. Here  $E(\ell)$  is a gauge-invariant way to characterize the dynamics, which is also applicable to full numerical relativity evolutions; see [65, 66] and Sec. V B. The  $E(\ell)$  curves are shown in Fig. 4 for the SLy EOS; other EOSs

show qualitatively the same behavior. From the figure one observes that aligned configurations are less bound than antialigned configurations. This behavior follows from the fact that the spin-orbit (SO) interaction, which is the main spin-related effect, is repulsive for aligned spins and attractive for antialigned spins (for a fixed  $\ell$ ), see, e.g., [67] and below.

In the following we explicitly compute the SO contribution in our binding energy data, and show its influence on the dynamics as well as its independence of finite size (EOS) effects. We write the binding energy as

$$E(\ell) = E_0 + E_{SO} + E_T + E_{SS}, \quad (4.3)$$

where  $E_0$  describes the binding energy of a nonspinning black hole binary in the conformal flatness approximation, and is therefore independent of the spin and matter effects;  $E_{SO}$  and  $E_{SS}$  represent the SO and spin-spin contributions, respectively; and  $E_T$  denotes the tidal contribution. Assuming for simplicity that the dimensionless spins are the same (as is the case here)  $\mathbf{j} := \mathbf{j}^A = \mathbf{S}^A / (M^A)^2 = \mathbf{j}^B = \mathbf{S}^B / (M^B)^2$ , the SO interaction is proportional to

$$E_{SO} \propto \mathbf{j} \cdot \mathbf{L} = \|\mathbf{j}\| \|\mathbf{L}\| \cos(\angle(\mathbf{j}, \mathbf{L})). \quad (4.4)$$

Thus, the angle between  $\mathbf{j}$  and the orbital angular momentum  $\mathbf{L}$  defines whether the SO interaction is repulsive or attractive. In the cases considered here,  $\cos(\angle(\mathbf{j}, \mathbf{L}))$  takes the values 1 and  $-1$ . For these two possibilities we can write

$$E_{SO} = \mathcal{E}_{SO}(\ell) j, \quad (4.5)$$

where  $j$  denotes the signed magnitude of  $\mathbf{j}$ , i.e.,  $j := \|\mathbf{j}\| \cos(\angle(\mathbf{j}, \mathbf{L}))$ . Equation (4.5) allows us to answer two important questions: (i) Do we see an imprint of the EOS on the SO interaction? (ii) Does the linear dependence of  $E_{SO}$  on  $j$  capture the main dynamics?

According to our spin definition (see above), the spins are constant during the adiabatic evolution. This is a good approximation at these separations and also supported by numerical evidence in binary black hole simulations [68–71]. The  $\mathcal{E}_{SO}(\ell)$  term can be computed using

$$\mathcal{E}_{SO}(\ell) = \frac{E_j^{(\uparrow\uparrow)}(\ell) - E_j^{(\downarrow\downarrow)}(\ell)}{2j} \quad (4.6)$$

for different (signed) spin magnitudes  $j$ , where  $E_j^{(\uparrow\uparrow)}(\ell)$  and  $E_j^{(\downarrow\downarrow)}(\ell)$  is  $E(\ell)$  for aligned and anti-aligned spins. Indeed, for a given spin, all the terms in (4.3) except  $E_{SO}$  cancel in the combination (4.6) because they all have the same sign.

The function  $\mathcal{E}_{SO}(\ell)$  is shown in Fig. 5 for all three EOSs considered here: SLy (top panel),  $\Gamma 2$  (middle panel), and MS1b (bottom panel). Additionally, we compute the average for all EOSs (solid line) and compare our results with the linear-in-spin part of the 4PN energy from Eq. (8.23) in [72], which is shown as a black dashed line in Fig. 5. From the figure we observe: (i)  $\mathcal{E}_{SO}(\ell)$  is positive, therefore the SO-interaction is repulsive/attractive (positive/negative) according to the sign

<sup>4</sup> Notice that the individual masses of the stars in isolation ( $M^A$ ,  $M^B$ ) are obtained here for spinning neutron stars and differ from the results for irrotational stars with the same baryonic mass.

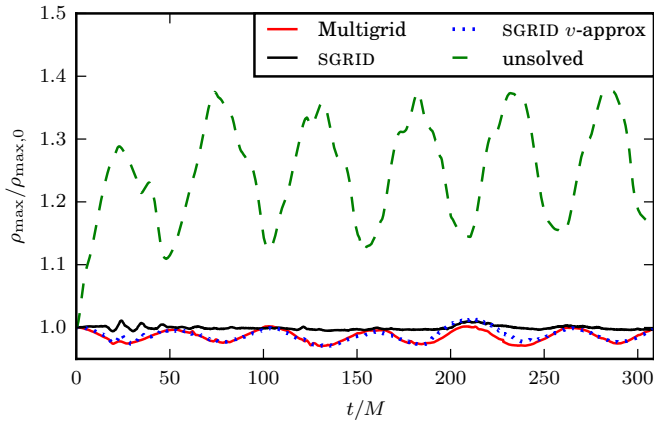


FIG. 6: Star’s maximum density scaled by its initial value: Simple superposition of TOV stars without solving the constraints (dashed green), Cartesian multigrid method solver of [17] (solid red), SGRID data assuming constant three-velocity (dotted blue) and SGRID data solving the fluid potential equation (2.32) (solid black).

of  $j$  [in general, this depends on  $\angle(\mathbf{j}, \mathbf{L})$ ]; (ii) all the curves agree within their errors, i.e., there is no significant dependence on finite size (EOS) effects. (iii) the PN expression from [72] captures the behavior of our conformally flat data for all employed EOSs.

We notice that the  $E_{SS}$  and the  $E_T$  terms in (4.3) can be extracted in a similar way. However, for the spin magnitudes and orbital separations considered here they lie within the uncertainty of our data.

## B. Highly eccentric configurations

In [17] we described a method to produce hydrodynamically consistent initial data for relativistic stars on orbits with arbitrary eccentricities for the first time. In our initial implementation of the method, we used an elliptic solver based on a Cartesian multigrid method, for which it is technically difficult to solve an equation to determine the velocity potential, since this would require boundaries at the star’s surface. Instead of introducing surface-fitted coordinates, we employed a constant three-velocity approximation, which could be motivated by the restriction to irrotational binaries. This means that we assumed the instantaneous (at apoastron) three-velocity  $v^y$  of a fluid element measured by a coordinate observer to be constant throughout the star, so the four-velocity could be written as

$$u^\alpha = u^t(t^\alpha + v^y y^\alpha). \quad (4.7)$$

However, SGRID provides surface-fitted coordinates and allows us to solve easily for the velocity potential. First, we want to briefly compare our old results to the newly obtained SGRID results and show the improvement of the initial data gained by solving the additional equation for the velocity potential. Fig. 6 compares the oscillations of the central density throughout the evolution for the previous multigrid solver and SGRID for two equal

mass stars with baryonic masses  $M_b^{A,B} = 1.620$  on a quasicircular orbit with an initial  $(2, 2)$  mode GW-frequency of  $M\omega_{22}^0 = 0.053$ .

This simple test case with two polytropic stars ( $\Gamma_2$ ) clearly shows the influence of the fully solved velocity potential: While we observe strong oscillations of 30% in the central density for superimposed TOV stars (which gives constraint violating initial data), we only observe roughly 4% oscillations for the constraint solved data using the constant 3-velocity approximation. In this case, SGRID and the Cartesian multigrid data give a good agreement. If we drop the approximation and solve for  $\phi$ , we can obtain even lower oscillations, improved by a factor of five, i.e., less than 1% (solid black line in Fig. 6). Here we use the same evolution setup in BAM as in [17], in order to make a direct comparison: We use the Baumgarte-Shapiro-Shibata-Nakamura [73–75] formulation, and 98 points in each direction in each of 5 refinement levels, with a grid spacing of  $h_5 = 0.1875$  on the finest level. We do not use the conservative mesh refinement introduced in [36]. The SGRID initial data use  $n_A = n_B = 24$ ,  $n_\varphi = 8$  and  $n_{\text{Cart}} = 20$  points. The reduced density oscillation with our new setup will allow us to study orbit induced oscillations as in [30] in more detail and disentangle the orbital effect from oscillations due to the initial data construction, which were present in previous attempts.

We now consider quasi-equilibrium sequences for different eccentricities. We compare our eccentric sequences to post-Newtonian results for the eccentricity in Fig. 7. Here we compute the PN eccentricity from the ADM expressions for the energy and angular momentum; we subtract the gravitational masses of the stars in isolation from the total ADM energy to obtain the binding energy that enters the PN calculation. (We did not perform such a comparison in [17], since the BAM implementation does not use a compactified grid including spatial infinity and was thus unable to compute the ADM quantities sufficiently accurately for this comparison.) In this figure, we see that the PN eccentricity indeed converges nicely to the input eccentricity as the binary’s separation increases, but it only converges well to the input eccentricity as one increases the PN order for smaller eccentricities (0 and 0.1). For the two larger eccentricities we consider (0.4 and 0.5), the 1PN results are closer to the input eccentricity than the 3PN results (though the 3PN results are closer than the Newtonian or 2PN results).

In order to obtain the PN expressions we used to create this figure, we, in essence, derived the 3PN extension of the 1PN expression for the eccentricity given in Eq. (2.36) of Mora and Will [76], using the general 3PN results they give. (The only difference in the derivations is that since we solve for the square of the eccentricity, we do not perform the PN expansion of the square root given in their expression.) We start from the expressions for  $\tilde{E} := E_b/(M\nu)$  and  $\tilde{J} := J/(M\nu^2)$  (the scaled binding energy and angular momentum) that Mora and Will give in Eqs. (2.35) and (2.40) for both harmonic and ADM coordinates. (Note that  $\tilde{E}$  and  $\tilde{J}$  are the same as the  $E$  and  $\ell$  used in Sec. IV A; the latter agreement only holds for the zero spin case we consider here.) We then invert



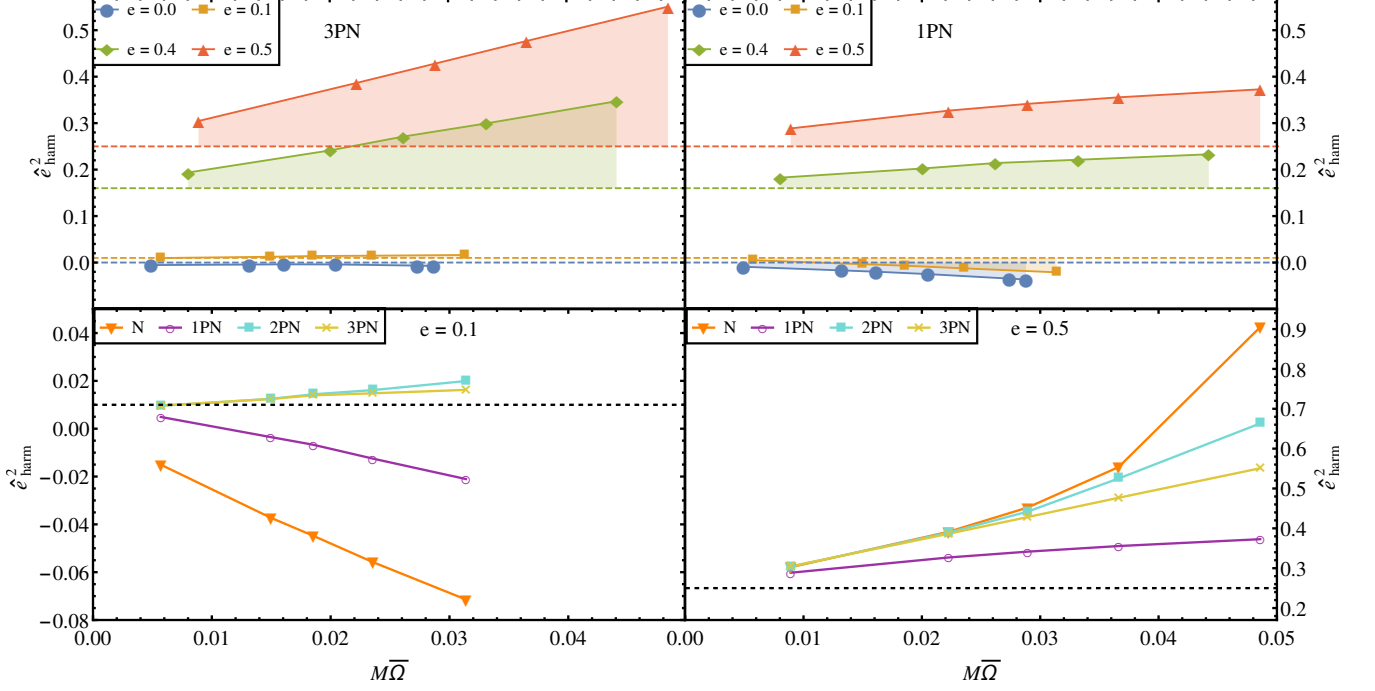


FIG. 7: The two plots in the top panel show the squared eccentricity  $\hat{e}_{\text{harm}}^2$  calculated from the ADM energy  $E$  and angular momentum  $J$  using harmonic coordinate PN expressions. We show the results at 3PN (top left) and 1PN (top right) for runs with different input eccentricity  $e$  (given as horizontal dashed lines). (We plot the square of the PN eccentricity since this quantity becomes negative for small  $e$ .) While the results for small eccentricities are calculated more accurately with increasing PN orders, the error is no longer monotonic with PN order for larger eccentricities. The two plots on the bottom panel show convergence of the eccentricity estimate with increasing PN order for an input eccentricity  $e = 0.1$  on the left and how this convergence becomes more erratic for higher eccentricities (using  $e = 0.5$  as an example) on the right side.

the series for  $\tilde{E}$  to express the PN parameter  $\zeta$  in terms of  $\tilde{E}$ ; we now use  $\tilde{E}$  as our expansion parameter. We can thus calculate the series for  $\tilde{E}\tilde{J}^2$  by substituting the series for  $\zeta$  in terms of  $\tilde{E}$  into the PN series for  $\tilde{J}$  and expanding consistently.

We then use the resulting harmonic coordinate expression to obtain a PN series for the square of the eccentric-

ity parameter,  $\hat{e}_{\text{harm}}^2$ , in terms of  $\tilde{E}$  and  $\tilde{J}$ . We experimented with various treatments of the expansion (e.g., not expanding after substituting the expression for  $\zeta$  in terms of  $\tilde{E}$  and/or solving for the eccentricity numerically instead of by series inversion) and found that a consistent expansion to a given PN order produced the most reasonable-looking results. Specifically, this gives

$$\begin{aligned} \hat{e}_{\text{harm}}^2 = & 1 - 2\xi + [-4 - 2\eta + (-1 + 3\eta)\xi]\tilde{E} + \left[ \frac{20 - 23\eta}{\xi} - 22 + 60\eta + 3\eta^2 - (31\eta + 4\eta^2)\xi \right] \tilde{E}^2 \\ & + \left[ \frac{-2016 + (5644 - 123\pi^2)\eta - 252\eta^2}{12\xi^2} + \frac{4848 + (-21128 + 369\pi^2)\eta + 2988\eta^2}{24\xi} - 20 + 298\eta - 186\eta^2 - 4\eta^3 \right. \\ & \left. + \left( -30\eta + \frac{283}{4}\eta^2 + 5\eta^3 \right) \xi \right] \tilde{E}^3, \end{aligned} \quad (4.8)$$

where  $\xi := -\tilde{E}\tilde{J}^2$ . We also performed the same calculation with the ADM coordinate expressions, which differ from the harmonic coordinate ones starting at 2PN, and found the expected small differences in the results ( $\lesssim 5\%$ , with smaller differences for larger eccentricities).

Our original motivation for using these particular PN results was to avoid using expressions which are not well-

behaved in the limit of a head-on collision from rest, which is what our eccentric data approach in the limit  $e \nearrow 1$ , e.g., expressions that have factors of  $\tilde{J}$  in the denominator. However, even though we start from expressions that are well-behaved in this limit (by considering  $\tilde{E}\tilde{J}^2$  instead of  $\tilde{J}$  by itself), we still obtain factors of  $1/\xi$  in the final expression for  $\hat{e}_{\text{harm}}^2$  [Eq. (4.8)]

starting at 2PN. This is not a significant problem since  $J_{\text{ADM}}$  is not very small for the systems we are considering. We thus also investigated the expressions given by Memmesheimer, Gopakumar, and Schäfer (MGS) [77] which are not well-behaved in the limit of constant energy and vanishing angular momentum. Here one can compute the three eccentricities defined in the post-Keplerian parametrization of an eccentric orbit ( $e_r$ ,  $e_t$ , and  $e_\phi$ ) from Eqs. (20) and (25) in MGS (these give the expressions in ADM and harmonic coordinates, respectively).

We find that  $e_t$  (particularly in harmonic coordinates) agrees quite well with the input eccentricities, especially at large separations, with fractional errors of  $< 2.4\%$  for all separations we consider for  $e = 0.5$ . In addition, we can compute the coordinate separation  $r$  of the stars from the ADM energy and angular momentum by noting that the binary is at apoapsis, so we can take  $\dot{r} = 0$  in Eqs. (A1) and (A3) in MGS (again, these give the expressions in ADM and harmonic coordinates, respectively) and then solve for  $r$  numerically. Here we find that the value for  $r$  we obtain by solving the harmonic coordinate equation agrees quite closely with the coordinate separation from SGRID for all the separations we consider, particularly for the two larger eccentricities we consider (fractional errors of  $< 2\%$ ). Such close agreement may simply be fortuitous, since there is no reason *a priori* to expect the coordinate systems used to agree so closely.

### C. Orbits with reduced eccentricity

The *heliptical approximate* symmetry vector (or, more formally, the *instantaneous helical vector*) introduced in Eq. (2.40) allows one to vary the binary's initial radial velocity, in addition to the control on the initial tangential velocity provided by the orbital frequency  $\Omega$ . If we do not make use of this freedom, i.e., if we set the radial velocity and the eccentricity parameter to zero,  $v_r = e = 0$ , we obtain the well known limit of standard quasicircular initial data. However, when we evolve such data, the separation between the stars oscillates. From these oscillations (or their imprint on the gravitational wave signal) we deduce actual measured eccentricities of  $\hat{e} \sim 10^{-2}$ . For the vast majority of astrophysical scenarios, this remaining eccentricity is purely artificial, because GWs efficiently circularise the orbit during the inspiral, leading to almost vanishing eccentricities during the last minutes before merger. In particular, the remaining eccentricity at merger  $\hat{e}$  of the six observed double neutron star systems that will coalesce within a Hubble time will be  $\hat{e} \lesssim 10^{-5}$  [4] and thus several orders of magnitude smaller than the eccentricity obtained when evolving standard quasicircular initial data.

The effect of this artificial eccentricity can be observed in various quantities, most notably the gravitational waveform. Therefore, we apply an iterative method to reduce the eccentricity, as outlined in [17]. This method is similar to the standard eccentricity reduction procedure for binary black holes [26, 78, 79], and the recent work on eccentricity reduction for binary neutron stars [29].

The basic idea is to find a measure for the eccentricity and determine which corrections have to be applied in order to remove the measured eccentricity from a Keplerian orbit. In this work, we use the proper distance  $d$  inside the hypersurface (measured along the coordinate line connecting the two local minima of the lapse, corresponding to the centers of the two stars) as well as the GW frequency  $\omega_{22}$  to estimate the remaining eccentricity  $\hat{e}$ . The coordinate distance  $d_{\text{coord}}$  can also be used to estimate  $\hat{e}$ . However,  $d_{\text{coord}}$  depends much more strongly on the particular gauge choice than the proper distance does and thus gives reliable results only in certain cases (cf. [29]), which is why we choose not to use it. Using  $d$  for the two neutron stars, we track this quantity throughout the evolution and fit it to the model

$$d(t) = S_0 + A_0 t + \frac{1}{2} A_1 t^2 - \frac{B}{\omega_f} \cos(\omega_f t + \phi) \quad (4.9)$$

Note that it is also possible to fit the time derivative  $\dot{d}(t)$  and get rid of one fitting parameter. However, taking the derivative of  $d$  introduces noise, especially for lower eccentricities. Applying some low-pass filters can help to improve the results, but  $d$  is generally better suited for obtaining the eccentricity measure than  $\dot{d}$ . The following results, however, apply to both methods. A comparison of the fitting model with the expected Keplerian orbits under the assumption that the eccentricity  $e$  is small for quasicircular orbits (so we can neglect higher orders of a series expansion), yields an eccentricity

$$e = \frac{B}{d_0 \omega_f} =: \hat{e}_d, \quad (4.10)$$

where  $d_0$  is the initial separation.

The ellipticity part of the model  $[-\frac{B}{\omega_f} \cos(\omega_f t + \phi)]$  leads to an initial radial velocity of  $B \sin \phi$  for the stars, which means that the initial radial velocity  $v_r$  in Eq. (2.40) has to be corrected by

$$\delta v_r = -B \sin \phi \quad (4.11)$$

in order to remove the eccentricity generated by the radial velocity. Similarly, we can adjust the eccentricity parameter  $e$  (and thus the initial tangential velocity) in order to remove the residual eccentricity induced by radial acceleration. The orbital angular frequency at apoastron  $\Omega_{\text{apo}}$  is related to the  $\Omega$  of the symmetry vector in Eq. (2.40) by  $\Omega_{\text{apo}} \approx (1 - e)\Omega$ . In Newtonian physics we have  $\Omega_{\text{apo}}^2 = (1 - e)GM/d_0^3$ . So if we change  $e$  by a small  $\delta e$ , this will lead to a change in  $\Omega_{\text{apo}}^2$  by  $\delta \Omega_{\text{apo}}^2 \approx -\frac{GM}{d_0^3} \delta e = \frac{\Omega_{\text{apo}}^2}{e-1} \delta e$ . Here all contributions of  $O(e^2)$  have been dropped, since we are only considering situations where  $e^2$  is quite small ( $\lesssim 10^{-4}$ ).

The radial acceleration in Eq. (4.9) is given by  $B \omega_f \cos \phi$ . Considering that a change of  $\delta \Omega_{\text{apo}}^2$  yields a change of the acceleration of  $d_0 \delta \Omega_{\text{apo}}^2$ , we obtain a necessary correction of

$$\delta e = \frac{B \omega_f \cos \phi}{\Omega_{\text{apo}}^2 d_0} (1 - e), \quad (4.12)$$

where  $\Omega_{\text{apo}}$  can be approximated by either  $\omega_f$  or  $\Omega$ . We obtain the correction parameters (4.11), (4.12) from our fit to the data from the evolution, where we need at least one to two orbits for the fit to be accurate enough. Then we iterate this process until the eccentricity is sufficiently small, i.e., in most cases two or three iterations.

Besides the already mentioned methods, there exist several other techniques to determine the eccentricity. To check the reliability of our results, we want to make use of the GWs to give an additional estimate of the eccentricity  $\hat{e}_{\text{GW}}$ . We follow the procedure given in [80], based on [81], and model the GW frequency motivated by post-Newtonian calculations as (cf. [82])

$$\omega_{\text{fit}} = \frac{1}{4}\tau^{-3/8} \left( 1 + c_1\tau^{-1/4} + c_2\tau^{-3/8} \right), \quad (4.13)$$

where  $c_1, c_2$  are determined by fitting and

$$\tau^2 = \frac{\nu^2(t_c - t)^2}{25M^2} + \tau_0^2, \quad (4.14)$$

where  $t_c$  and  $\tau_0$  are again fitting parameters. We proceed by looking at the quantity

$$\hat{e}_\omega(t) = \frac{\omega_{22}(t) - \omega_{\text{fit}}(t)}{2\omega_{\text{fit}}(t)}. \quad (4.15)$$

This measure of eccentricity is time dependent and strongly oscillatory, but the global extremum

$$\hat{e}_{\text{GW}} = \max_t |\hat{e}_\omega(t)| \quad (4.16)$$

can be seen as a time-independent measure of eccentricity; see Fig. 8. As it is to be expected intuitively, this value can mostly be found in the beginning of the evolution, just after the initial gauge noise has decayed. Note that the initial noise has to be cut off in order to obtain consistent data; this is also necessary for the estimate based on the proper distance. Comparing the eccentricities obtained this way with the eccentricities computed from the proper distance, we observe an agreement within roughly five percent (comparing  $\hat{e}_{\text{GW},3} = 8.4 \times 10^{-4}$  to  $\hat{e}_{d,3} = 8.7 \times 10^{-4}$  for the third eccentricity reduction iteration step of an SLy EOS run; cf. Table II). Considering the decrease in signal-to-(numerical)-noise of the proper distance oscillations at higher iterations, and thus the reduced accuracy in the parameters one obtains from the fitting procedure, this agreement is satisfying and shows the consistency of the measures. In order to minimize the computational effort for finding eccentricity reduced initial data, it makes sense to evaluate  $\hat{e}_d$  to find the next iteration step's parameters, since in this case we have to evolve for fewer time steps. Using the gravitational wave signal necessitates longer evolutions to ensure that the wave has reached the extraction radius.

Table II shows the numerical values for the eccentricity reduction iteration for two runs with different setups, viz., two equal-mass binaries with different total masses, one with the SLy EOS and the other with the  $\Gamma 2$  EOS. Additionally, we show the proper distance  $d$  for the latter setup in Fig. 9. We used SGRID with  $n_A = n_B = 26$ ,  $n_\varphi = 8$ ,  $n_{\text{Cart}} = 22$  points. The evolution was done in BAM with

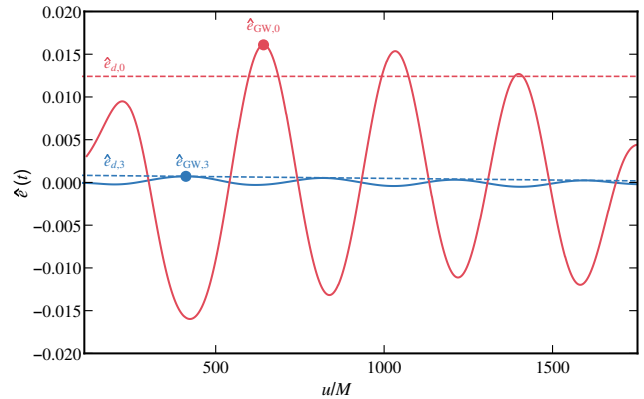


FIG. 8: The eccentricity as a function of retarded time  $u$  computed from the residual of the GW frequency for SLy initial data with an initial [(2,2) mode] GW frequency of  $M\omega_{22}^0 = 0.0365$ . We show the quasircular data (red) and the third iteration of the eccentricity reduction (blue). The global extremum, marked by the points, gives eccentricities of  $\hat{e}_{\text{GW},0} = 0.0156$  and  $\hat{e}_{\text{GW},3} = 0.00084$  for these iterations, which is a factor of 20 improvement. The horizontal dashed lines mark the eccentricities  $\hat{e}_d$  calculated from the proper distance.

TABLE II: Iteration procedure for two binary setups starting at  $M\omega_{22}^0 = 0.0365$ . The first configuration is a  $\Gamma 2$  binary with individual masses of  $M^A = M^B = 1.515$  and a total ADM mass of  $M_{\text{ADM}} = 3.006$ . The second one is an equal mass SLy configuration with  $M^A = M^B = 1.350$  and  $M_{\text{ADM}} = 2.6782$ . The columns give the eccentricity  $e$  and radial velocity  $v_r$  input to the code [cf. Eq. (2.40)], along with  $\hat{e}_d$ , the remaining eccentricity in the binary evolution measured using the proper distance  $d$  in the hypersurface. We also list the values of the binding energy  $E_b = M_{\text{ADM}} - M$  and the angular momentum  $J_{\text{ADM}}$ , which we normalize by  $M$  and  $M^2$ , respectively.

EOS	Iter	$e$ [ $10^{-3}$ ]	$v_r$ [ $10^{-3}$ ]	$\hat{e}_d$ [ $10^{-3}$ ]	$E_b/M$ [ $10^{-3}$ ]	$J_{\text{ADM}}/M^2$
$\Gamma 2$	0	0	0	9.77	-7.984	1.0700
	1	-6.8	-1.63	1.38	-7.922	1.0729
	2	-5.7	-1.14	0.91	-7.920	1.0738
	3	-6.3	-1.16	0.56	-7.920	1.0734
SLy	0	0	0	12.41	-8.115	1.0541
	1	-6.0	-1.13	7.80	-8.103	1.0580
	2	-12.1	-1.91	3.97	-8.088	1.0615
	3	-13.7	-1.09	0.87	-8.085	1.0625

a constraint damping Z4c evolution scheme, as described in Sec. V. We used a total of 7 refinement levels, where the two inner levels contained 96 points in each direction in each box with a grid spacing of 0.15 in the finest. The other outer boxes all contain 192 points in each direction; the grid spacing is doubled on each successive level moving outwards. Finally, the outermost level is given by a cubed sphere (cf. [54, 83–85]; this is also used for the evolutions in Sec. V) with 192 and 84 points in the radial and azimuthal directions, respectively. Over the course of three iteration steps, using the method outlined above to iteratively determine the correction parameters  $\hat{e}_d$  and  $v_r$ , we were able to decrease the eccentricity in the  $\Gamma 2$  case

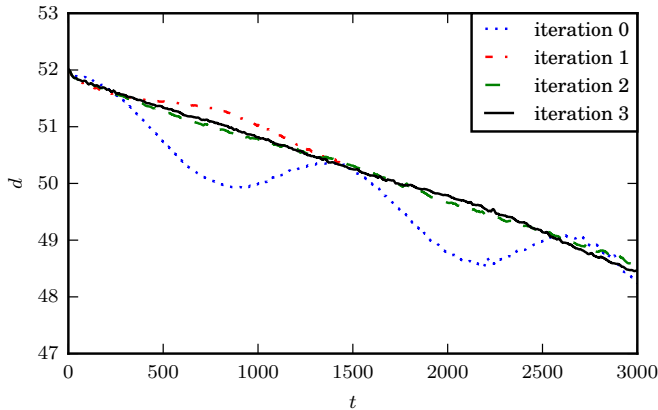


FIG. 9: Comparison of the eccentricity of the simple polytropic  $\Gamma_2$  setup by looking at the proper distance as a function of time. The blue dotted line is from an evolution of the original initial data set, while the solid black line uses the third iteration step of the eccentricity reduction procedure.

from  $\hat{e}_{d,0} = 9.8 \times 10^{-3}$  to  $\hat{e}_{d,3} = 5.6 \times 10^{-4}$ , which can be seen in a significant improvement of the oscillations of the proper distance (Fig. 9). Similar improvements in the gravitational waves can be seen in Fig. 8 for the SLy case.

Furthermore, we can try to give some PN estimates of the improvement of the data by looking again at the PN expressions from Mora and Will [76], which we already utilized in Sec. IV B. We can even expand our comparisons to fourth post-Newtonian order (as summarized in [29]) without any essential changes in the results, since the 4PN contribution is small.

Given the fairly large initial separation of the binaries, we expect the fourth post-Newtonian order results for the ADM energy and angular momentum in terms of the binary’s angular velocity to be quite accurate and we indeed find that the eccentricity reduced data gives a better match to the values for these quantities for a circular orbit than do the original data: Table II gives the binding energy  $E_b$  and the angular momentum  $J_{\text{ADM}}$  and if we compare these to PN for the SLy run (with  $J_{\text{ADM, PN}} = 1.0637M^2$  and  $E_{b, \text{PN}} = -0.008081M$ ), we find a relative error of  $\sim 1\%$  for original data and an error of  $\sim 0.2\%$  for the data at the third iteration. Similarly, for the simple polytropic  $\Gamma_2$  run, we compare our results to  $J_{\text{ADM, PN}} = 1.0731M^2$  and  $E_{b, \text{PN}} = -0.007918M$  and find an improved agreement of the eccentricity reduced data with a deviation of  $\sim 0.04\%$ , compared with a deviation of  $\sim 0.4\%$  for the original data. We thus see that the eccentricity reduced data are closer to quasi-equilibrium than the standard initial data, as was noted by [29].

#### D. Unequal masses

As outlined in Sec. I and explained in more detail in Appendix A 1, some population synthesis models predict relatively high mass-ratio BNS systems. In this section we want to illustrate SGRID’s ability to generate quasiequilibrium configurations for such systems. We

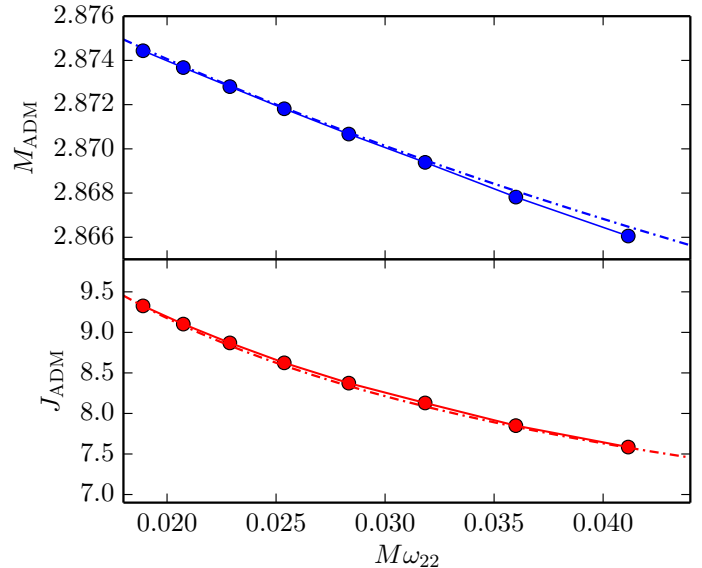


FIG. 10:  $q = 2.06$  sequence. Top panel: ADM mass compared with 4PN tidal results (dot dashed lines). Bottom panel: ADM angular momentum compared with 4PN tidal results (dot dashed lines).

model the systems by the stiff EOS MS1b. This EOS allows rather large baryonic masses up to  $M_b = 3.35$  and gravitational masses up to  $M = 2.76$  for single neutron stars in isolation. As is seen in the next subsection, it is one of the EOSs for which we achieved high neutron star masses in equal-mass binaries with SGRID.

The particular configuration constructed below consists of  $M_b^A = 1.00$  ( $M^A = 0.94$ ) and  $M_b^B = 2.20$  ( $M^B = 1.94$ ) neutron stars resulting in a mass ratio of  $q = 2.06$ . We want to highlight that this is (i) a slightly larger mass ratio than the largest predicted by the population synthesis models discussed in Appendix A 1, (ii) the largest mass ratio computed for a realistic (irrotational) binary configuration in quasi-equilibrium,<sup>5</sup> and (iii) the largest mass ratio evolved in full general relativity;<sup>6</sup> see Sec. V A. We employ a grid with  $n_A = n_B = 28$ ,  $n_\varphi = 8$ ,  $n_{\text{Cart}} = 24$  and construct a sequence varying the distance parameter  $b \in [16, 30]$ . This results in GW frequencies of  $M\omega_{22} \in [0.019, 0.041]$ .

The ADM mass and angular momentum for this sequence are shown in Fig. 10. As a comparison, we show the 4PN results including tidal components given in Appendix A of [29] (obtained from [86] and [87]). However, the influence of the tidal contributions and higher-PN terms (above 2PN) is negligible at the scale shown here. Additionally, we emphasize that a direct comparison of these results is not really warranted, since SGRID uses

<sup>5</sup> In [22] (see that paper’s Table 1), one of us computed corotating binary neutron star initial data with baryonic mass ratios up to 3 for large separations, using a polytropic EOS and small baryonic masses.

<sup>6</sup> Up to now the highest mass ratio evolved in full general relativity was  $q = 1.5$  [35, 36].

the conformal flatness approximation, which is known to be violated at 2PN (see, e.g., the discussion in Sec. III A of [17]).

Due to the newly implemented mechanism in SGRID which adjusts the center of mass so that  $P_{\text{ADM}}^y$  is kept small (ideally vanishing), the linear momentum of the configuration stays within  $\sim 10^{-5}$  to  $\sim 10^{-4}$ . In particular, for the configuration with  $M\omega_{22} = 0.0359$  that we evolve in Sec V A, the linear momentum is  $\mathbf{P}_{\text{ADM}} = (4.23 \times 10^{-7}, -1.10 \times 10^{-5}, -1.96 \times 10^{-6})$ .

### E. High compactness

While population synthesis models predict a number of binary neutron star systems containing high-mass (and thus high-compactness) neutron stars (see Appendix A 1), computing initial data for binary neutron stars with high compactnesses is a challenging task for most codes. The highest compactness achieved for a neutron star in a relativistic binary is:  $\mathcal{C} \simeq 0.26$  for a neutron star-black hole system [88],  $\mathcal{C} \simeq 0.25$  for corotating binary neutron stars [89],  $\mathcal{C} \simeq 0.26$  for irrotational binary neutron stars [37], and  $\mathcal{C} \simeq 0.22$  for binary neutron stars with relatively low spins [18].

In the following we present results for most EOSs listed in Table I (except for the  $\Gamma_2$  EOS, which does not allow high compactness neutron stars) and provide an estimate of the highest compactness easily reachable with our numerical method. In physical terms, the maximum feasible compactness depends mostly on two different properties: (i) the chosen EOS and (ii) the binary separation. However, in SGRID the resolution and iteration procedure (e.g., the softening parameter and mass increment) also play important roles.

As a starting point, we choose a simple procedure to estimate the maximum compactness  $\mathcal{C}_{\text{max}}$  reachable with SGRID. We consider equal-mass nonspinning binaries, fix the separation parameter  $b$ , and increase the baryonic masses of the two stars in steps of  $\Delta M_b = 0.005$ , starting from  $M_b^A = M_b^B = 1.2$ . We stop increasing the mass when the elliptic solve of Eqs. (2.18), in particular the Hamiltonian constraint equation, does not reduce the residual and no solution can be found. For our test we use a resolution of  $n_A = n_B = 24$ ,  $n_\varphi = 8$ ,  $n_{\text{Cart}} = 20$ .

Table III summarizes the maximum compactness achieved for different EOSs and separations. In all cases we were able to achieve higher compactnesses at larger separations. The maximum compactness for the EOSs and separations considered lies within (0.197, 0.212) for this simple iteration procedure. We obtain the highest compactness for this test (with a constant number of grid points) with the simple polytropic EOS  $\Gamma_2.72$ . This is to be expected, since runs with piecewise polytropic EOSs require higher resolutions to obtain the same accuracy as runs with simple polytropic EOSs, as discussed in Sec. IV F.

Even higher compactnesses can be achieved by reducing  $\Delta M_b$ , decreasing the softening parameter to 0.2, and using higher resolutions. We now give an explicit example of this procedure.

In order to achieve high compactness with the SLy EOS, we have considered a non-spinning equal mass system with a separation parameter of  $b = 31$ . We started with baryonic masses  $M_b^A = M_b^B = 1.5$  and increased the mass in each iteration by a factor of 1.07 until we reached  $M_b^A = M_b^B = 1.82$ . The highest resolution used for this configuration was  $n_A = n_B = 28$ ,  $n_\varphi = 8$ ,  $n_{\text{Cart}} = 24$ . This results in a binary with ADM mass  $M_{\text{ADM}} = 3.193$ , angular momentum  $J_{\text{ADM}} = 12.759$ , orbital angular velocity  $\Omega = 0.00336$ , dimensionless GW-frequency  $M\omega_{22} = 0.0216$ , and a coordinate separation of 63.270 between the star centers. A single TOV star with the same baryonic mass would have an ADM mass of 1.60564 and a radius of 7.69608 (in standard Schwarzschild areal radius coordinates), which implies a compactness of 0.2086.

Increasing the baryonic masses beyond  $M_b^A = M_b^B = 1.82$  has proven very difficult. For masses above this value we observe that the elliptic solver cannot always solve Eq. (2.18a) for  $\psi$  within the main iteration, because the values from the previous iteration are not good enough as an initial guess for the Newton-Raphson scheme we use. We were able to address this problem by making two changes to our Newton-Raphson scheme. First, we take smaller Newton steps if this results in a smaller residual error than a full step (this procedure is known as backtracking). And second, if backtracking also fails we simply skip the elliptic solve for  $\psi$ . The overall iteration still succeeds if we do not skip the elliptic solve for  $\psi$  too often. Using this trick we started from the initial data for  $M_b^A = M_b^B = 1.82$  and increased the masses by a factor of 1.02 in the main iteration until we reached  $M_b^A = M_b^B = 2.0$ . The resulting initial data were again computed with  $n_A = n_B = 28$ ,  $n_\varphi = 8$ ,  $n_{\text{Cart}} = 24$  and result in a binary with ADM mass  $M_{\text{ADM}} = 3.459$ , angular momentum  $J_{\text{ADM}} = 14.444$ , orbital angular velocity  $\Omega = 0.00347$ , dimensionless GW-frequency  $M\omega_{22} = 0.0242$ , and a coordinate separation of 63.262 between the star centers. The Hamiltonian constraint violation for this data set is about twice as big as for the lower mass data, because we do not always solve Eq. (2.18a), which is the Hamiltonian constraint. A single TOV star with the same baryonic mass would have an ADM mass of 1.74067 and a radius of 7.6104 (in standard Schwarzschild area radial coordinates), which implies a compactness of 0.2287.

If we try to increase the baryonic masses beyond  $M_b^A = M_b^B = 2.0$  we can never solve Eq. (2.18a) for  $\psi$ , so we obtain constraint violating initial data.

### F. Convergence of SGRID

The convergence of SGRID was already presented in Fig. 3 of [22] for a corotating equal-mass quasicircular binary neutron star system with a simple polytropic EOS. However, we want to show here how well the code converges in more complicated situations. To illustrate this, we consider the configurations presented in Tab. IV. In particular, we choose configurations with  $q = 1.0$  where each star has a gravitational mass of

TABLE III: Overview of high compactness configurations without fine tuning the iteration procedure. The columns refer to: the SGRID distance parameter  $b$ , the dimensionless gravitational wave frequency  $M\omega_{22}$ , the maximum baryonic mass  $M_{b, \max}$ , the corresponding gravitational mass  $M_{\max}$ , and compactness  $C_{\max}$ .

EOS	$b$	$M\omega_{22}$	$M_{b, \max}$	$M_{\max}$	$C_{\max}$	$b$	$M\omega_{22}$	$M_{b, \max}$	$M_{\max}$	$C_{\max}$	$b$	$M\omega_{22}$	$M_{b, \max}$	$M_{\max}$	$C_{\max}$
SLy	22	0.032	1.727	1.534	0.199	26	0.026	1.744	1.547	0.200	32	0.020	1.780	1.575	0.204
ENG	22	0.033	1.788	1.583	0.199	26	0.024	1.824	1.611	0.203	32	0.021	1.852	1.632	0.206
MPA1	22	0.035	1.871	1.661	0.200	26	0.029	1.899	1.676	0.202	32	0.022	1.927	1.683	0.203
ALF2	22	0.036	1.899	1.678	0.200	26	0.029	1.937	1.708	0.204	32	0.023	1.976	1.738	0.208
H4	22	0.038	1.976	1.762	0.197	26	0.031	1.996	1.777	0.199	32	0.024	2.026	1.800	0.203
MS1b	22	0.043	2.183	1.931	0.198	26	0.036	2.216	1.963	0.201	32	0.027	2.250	1.982	0.203
MS1	22	0.043	2.205	1.955	0.197	26	0.036	2.238	1.981	0.200	32	0.028	2.273	2.007	0.203
$\Gamma 2.72$	22	0.042	2.162	1.908	0.205	26	0.034	2.183	1.924	0.207	32	0.027	2.238	1.966	0.212

TABLE IV: Convergence test setups. Columns refer to: Name of the configuration, EOS, distance parameter  $b$ , eccentricity parameter  $e$  [from (2.38)], the baryonic masses  $M_b^A$  and  $M_b^B$ , and the angular velocity vector  $\omega^i$  as specified in Eq. (2.22).

Name	EOS	$b$	$e$	$M_b^A$	$M_b^B$	$\omega_{A,B}^i$
$\Gamma 2q100w000e00$	$\Gamma 2$	20	0.0	1.4336	1.4336	(0, 0, 0)
$\Gamma 2q100w005e00$	$\Gamma 2$	20	0.0	1.4336	1.4336	$0.005 \cdot (1, 1, 1)$
$\Gamma 2q100w000e03$	$\Gamma 2$	20	0.3	1.4336	1.4336	(0, 0, 0)
$\Gamma 2q100w005e03$	$\Gamma 2$	20	0.3	1.4336	1.4336	$0.005 \cdot (1, 1, 1)$
$\Gamma 2q116w000e00$	$\Gamma 2$	20	0.0	1.5491	1.3199	(0, 0, 0)
$H4q100w000e00$	H4	20	0.0	1.4687	1.4687	(0, 0, 0)
$H4q100w005e00$	H4	20	0.0	1.4687	1.4687	$0.005 \cdot (1, 1, 1)$
$H4q100w000e03$	H4	20	0.3	1.4687	1.4687	(0, 0, 0)
$H4q100w005e03$	H4	20	0.3	1.4687	1.4687	$0.005 \cdot (1, 1, 1)$
$H4q116w000e00$	H4	20	0.	1.5887	1.3506	(0, 0, 0)

1.35. We either investigate nonspinning configurations [i.e.,  $\omega_A^i = \omega_B^i = (0, 0, 0)$ ] or choose an angular velocity of  $\omega_A^i = \omega_B^i = (0.005, 0.005, 0.005)$ . We also use different eccentricities of  $e = 0.0$  and  $e = 0.3$ . Finally, we consider an unequal mass configuration with gravitational masses 1.45 and 1.25 ( $q = 1.16$ ). We compute initial data for these systems for both a simple polytropic EOS as well as a piecewise polytropic EOS (the fit to the realistic H4 EOS).

Figure 11 summarizes our findings. In the simple polytropic runs (upper panel), we encounter a higher Hamiltonian constraint for  $\Gamma 2q100w005e00$  and  $\Gamma 2q100w005e03$  than for the other configurations. This clearly shows that the addition of spin increases the complexity of the system, while adding eccentricity has no noteworthy effect. In the cases where no spin is present, the Hamiltonian constraint is one to two orders of magnitude smaller. For unequal masses we see a slightly larger constraint violation. The momentum constraints converge in a similar manner, but their magnitude is roughly one order of magnitude smaller.

When piecewise polytropes are employed, the constraint violations increase substantially. This is to be expected, since the solution is only  $C^1$  at the interfaces

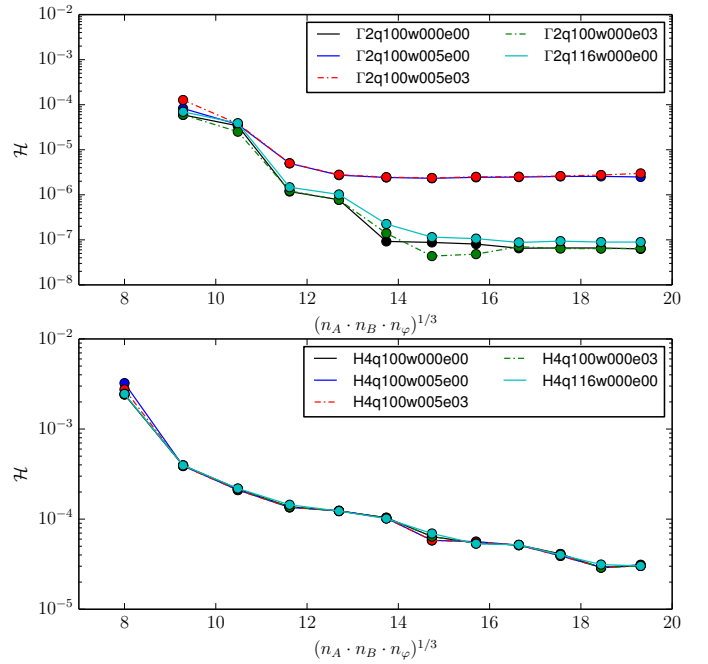


FIG. 11: Convergence analysis for representative configurations. Simple polytropic  $\Gamma 2$  configurations (top panel) and piecewise polytropic (H4) configurations (bottom panel). The plot shows the average Hamiltonian constraint inside the two stars in the regions  $A \in [0, A_{\max}]$  and thus includes the stars' surfaces, which are the most problematic regions. We have fixed  $n_\varphi = 8$  and use  $n_A = n_B$ ,  $n_{\text{Cart}} = n_A - 4$ .

between the different pieces, so one will no longer obtain exponential convergence from the spectral method. In this case, however, the addition of spin and eccentricity or the consideration of unequal masses has no noteworthy additional effect. Since spin most likely affects the convergence primarily through the deformation of the star's surface, it is not surprising that it does not affect the convergence so much for piecewise polytropes at these resolutions, where the portion near the surface is already quite troublesome, due to the necessity of resolving the crust. We expect that one would see a difference due to the addition of spin at much higher resolutions or for higher spin magnitudes. This reduction in convergence when using piecewise polytropes means that in most cases we use



higher resolutions when computing piecewise polytropic setups, compared to previous work with just simple polytropes.

## V. DYNAMICAL EVOLUTIONS

In this section we present evolutions of our new initial data for two new configurations: (i) a high-mass ratio simulation with  $q = 2.06$ , which is the *highest mass ratio binary neutron star* ever evolved in full numerical relativity; (ii) an unequal-mass configuration where the spins are not aligned with the orbital angular momentum, which is the *first precessing binary neutron star* simulation performed so far. The new dynamical evolutions presented here show, as a proof of principle, that the BNS phenomenology can be very rich in these newly accessible regions of parameter space, where we are now able to study mass exchange during the inspiral or the precession and nutation of the orbital plane during a binary neutron star simulation. Additionally, we discuss (iii) the effect of eccentricity reduction on the waveform phasing.

We perform the evolutions with the newest version of the BAM code [36, 51, 52] including the recently implemented conservative mesh refinement algorithm employed in [36, 90]. We also use the Z4c scheme [54, 91] with constraint preserving boundary conditions [54, 92]. The BAM grid setup consists of 7 refinement levels. The outermost level ( $l = 0$ ) uses a multipatch “cubed-sphere” grid [54, 83–85].

The setups of Sec. VB do not employ any symmetry condition. For the other simulations we employ reflection symmetry across the orbital plane, letting us use half the number of grid points in the  $z$ -direction. Further information about the particular grid and initial conditions is given in Tab. V.

### A. A $q = 2.06$ binary

In this section we evolve one of the models computed in Sec. IVD. We have set the rest mass of the primary star to  $M_b^A = 2.200$ , corresponding to a gravitational mass of  $M^A = 1.944$  and compactness  $\mathcal{C}^A = 0.199$  in isolation, while the companion is characterized by  $M_b^B = 1.000$ ,  $M^B = 0.944$ ,  $\mathcal{C}^B = 0.103$ . We have not tried to add spin/eccentricity or performed eccentricity reduction since we want to focus solely on the high mass ratio effects. Nevertheless, the setup shows a rather small eccentricity of  $\hat{e}_d = 4.2 \times 10^{-3}$ ,  $\hat{e}_{\text{GW}} = 5.1 \times 10^{-3}$  and despite the high mass ratio a small linear momentum of  $\mathbf{P}_{\text{ADM}} = (4.23 \times 10^{-7}, -1.10 \times 10^{-5}, -1.96 \times 10^{-6})$ . The initial gravitational wave frequency is  $M\omega_{22}^0 = 0.0359$ . Star B is already deformed at this separation indicated by a mass shedding parameter of  $\chi \simeq 0.89$ ; cf. Eq. (C4).

This configuration, with a gravitational mass ratio of  $q = 2.06$ , is the highest mass ratio binary neutron star evolved in full general relativity, and well above the mass ratio of  $q = 1.5$  considered before [35, 36]. Note

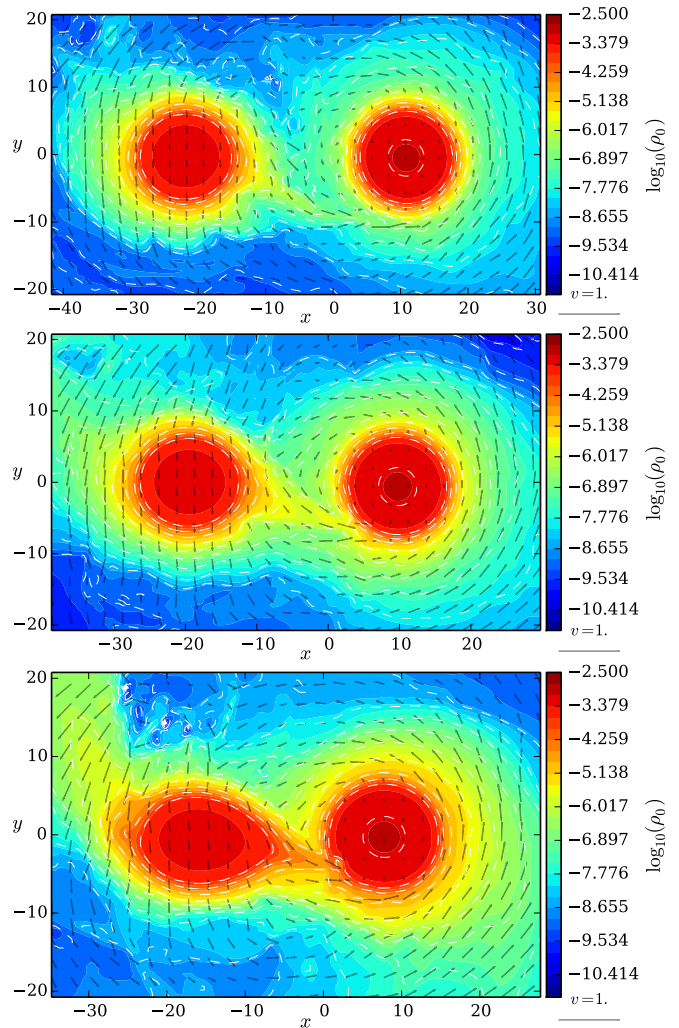


FIG. 12: Plot of the matter density  $\rho_0$  and the velocity  $v^i$  in the orbital plane for the  $q = 2.06$  simulation at times  $t = 1726M$  (upper panel), two revolutions later at  $t = 2227M$  (middle panel), and yet another two revolutions later at  $t = 2644M$  (lower panel). Over the 4 revolutions shown, one can see a clear mass transfer between the two stars. Note that each plot has a somewhat different scale.

that [93] reports results of Newtonian smooth particle hydrodynamics (SPH) evolutions (including radiation reaction) for a similar  $q = 2$  setup [gravitational masses of  $(1.0 + 2.0)$ ], but does not mention any mass transfer, which we find in our simulation. However, mass transfer is observed in white dwarf binary simulations with  $q = 2$  [94].

#### 1. Mass transfer

In Fig. 12 we show snapshots of the density in the orbital plane during the inspiral. The upper panel of Fig. 12 shows the binary at  $t = 1726M$ . Although the stars are clearly separated, mass transfer from the companion ( $M^B$ ) to the primary star ( $M^A$ ) has already set in. Two revolutions later [ $t = 2227M$  (middle panel)] and four revolutions later [ $t = 2644M$  (lower panel)] the

TABLE V: Initial data and grid details for the dynamical evolutions. The columns refer to: the simulation name, the gravitational and baryonic masses of star A and B, the stars' dimensionless angular momenta  $j^{A,B}$ , the number of grid points employed in each direction in the fixed and moving boxes, the number of radial and azimuthal points, the finest grid spacing, and the outer boundary location.

name	$M^A$	$M_b^A$	$M^B$	$M_b^B$	$j^A$	$j^B$	$n$	$n^{mv}$	$n_r$	$n_\theta$	$h_6$	$r_b$
MS1b-q206	1.944	2.200	0.944	1.000	(0,0,0)	(0,0,0)	128	72	144	63	0.250	1692
SLy $(\nearrow\nearrow)$	1.3553	1.500	1.1072	1.200	$(0.13/\sqrt{3})(1,1,1)$	$(0.16/\sqrt{3})(1,1,1)$	128	64	128	56	0.245	1532
SLy $(\uparrow\uparrow)$	1.3547	1.500	1.1067	1.200	$0.077(0,0,1)$	$0.089(0,0,1)$	128	64	128	56	0.245	1532
SLy $(^{00})$	1.3544	1.500	1.1065	1.200	(0,0,0)	(0,0,0)	128	64	128	56	0.245	1532
SLy-eccred	1.350	1.495	1.350	1.495	(0,0,0)	(0,0,0)	192	96	192	84	0.15	1384

mass transfer becomes more dramatic. During this period,  $\sim (2-3) \times 10^{-2} M_\odot$  of material was transferred between the two stars, i.e.,  $\sim (2-3)\%$  of the rest mass of the less massive star. The estimate is based on the rest mass leaving the finest refinement level around star B and entering the refinement level of star A. The uncertainty is mainly related to mass loss due to the artificial atmosphere treatment [36]. (Note that the overall rest mass is conserved to better than 0.12% in this simulation until very late times, post-merger, when matter starts leaving the grid.) We observe that for this system the mass transfer happens continuously until the companion is tidally disrupted.

The average rate of mass transfer is  $\dot{M}_{AB} \sim 10^{-5} \sim 1 M_\odot \text{ s}^{-1}$ , taking place for  $\sim 10^{-2} \text{ s}$ , from which one can estimate the accretion power. Here we just make a simple, order-of-magnitude estimate, since this is likely all that is warranted by the accuracy of our estimate of the mass transfer. If one just considers the change in energy of this matter going down the more massive star's Newtonian potential well, we have an average accretion power of  $\sim \dot{M}_{AB} \mathcal{C}^A \sim 10^{-6} \sim 10^{53} \text{ erg s}^{-1}$ , comparable to the neutrino luminosities found in simulations of BNS mergers [41, 49, 50]. (Recall that  $\mathcal{C}^A$  is the compactness of  $M^A$  in isolation.) This gives a total accretion energy of  $\sim 10^{51} \text{ ergs}$ , which is comparable to the energy released in a supernova. But of course, one cannot say anything definite about the amount of this energy that would be released in photons or neutrinos, since these are not present in our simulation. While one might expect to be able to see the effects of this amount of mass transfer on the phase of the gravitational waves, the present simulation does not appear to be accurate enough to make such a comparison.

The merger happens at  $t = 2692M$ . We classify the merger remnant as a supramassive neutron star (SMNS), since it is below the maximum supported gravitational mass of a rigidly rotating star for the MS1b EOS, which is  $\sim 3.2-3.3 M_\odot$ , i.e., roughly  $\sim 15-20\%$  larger than the corresponding maximum gravitational mass of a nonrotating neutron star (see, e.g., Sec. 2.9.1 in [95]). We thus do not expect the SMNS to collapse on dynamical timescales. This is supported by our simulation, where no indication for a collapse is present through the end of the simulation at  $t = 6500M \simeq 0.09 \text{ s}$ . The central density reaches a constant value  $\rho_c \simeq 9.8 \times 10^{-4} \simeq 6 \times 10^{14} \text{ g cm}^{-3}$  and the final merger product settles into a stable configura-

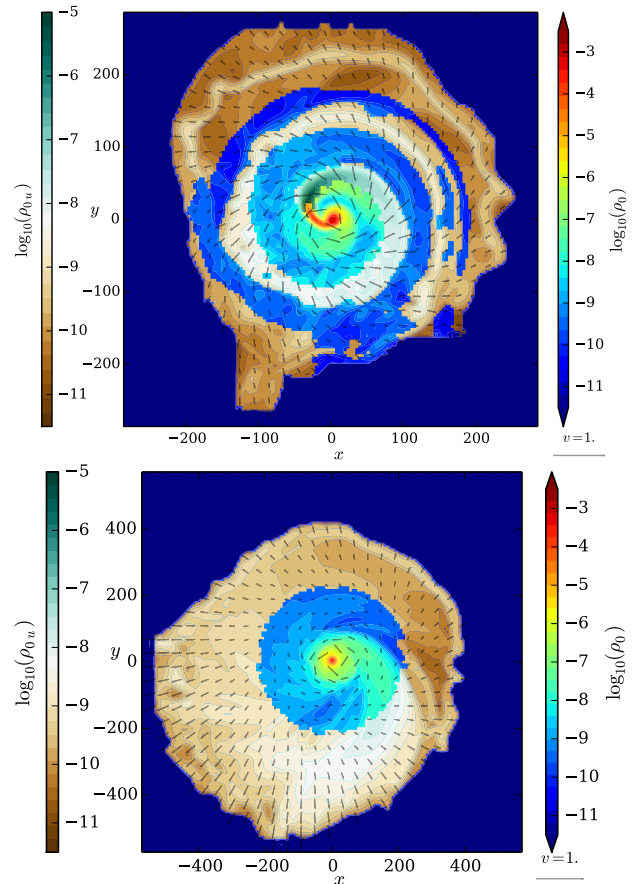


FIG. 13: Plot of the matter density  $\rho_0$ , the density of unbound matter  $\rho_{0u}$ , and the velocity field  $v^i$  in the orbital plane for the  $q = 2.06$  simulation after merger. In the upper panel ( $t = 2798M$ ) a clear spiral like pattern in the ejecta is visible, where material is expelled due to torque in the tidal tail of the companion star. The lower panel ( $3421M$ ) shows that material is ejected over the entire grid anisotropically. Note that the two panels have different scales.

tion.

## 2. Ejecta and kick

In this simulation we observe a significant mass ejection,  $M_{\text{ejecta}} \simeq 7.6 \times 10^{-2} M_\odot$ , which is among the largest found for full general relativistic simulations of binary



neutron star mergers, including the case of eccentric binaries [96], and much larger than any of the ejecta masses found for the quasicircular case in the studies in [36, 97].

Figure 13 visualizes the ejected material, distinguishing it from the bound material by using a different color bar. Here we compute the unbound material using the method given in [36]. In our simulation most of the material is ejected into the orbital plane by torque on the tidal tail of the companion star; cf. the discussion in [36, 97]. We can also see this in the spiral-like pattern in the upper panel of Fig. 13, at a time of  $t = 2798M$ . In the lower pattern we see also clearly that the ejection happens anisotropically, where the density inside of the ejected material at a given radial distance from the SMNS differs by several orders of magnitude in different directions. The kinetic energy of the ejecta is  $\sim 2 \times 10^{-3} \simeq 4 \times 10^{50}$  erg. Note that the ejecta mass we find is a factor of  $\sim 2$  larger than that found in the Newtonian calculation of [93] (Table 1 there). This is significant, since, as discussed in [36], the uncertainty on the ejecta mass is about  $\lesssim 20\%$ , and mainly due to the resolution.

The anisotropic mass ejection causes the merger remnant to recoil. We approximate the ejecta's linear momentum by computing

$$\mathbf{P}_{\text{ej}} = M_{\text{ej}} \langle \mathbf{v}_{\text{plane}} \rangle = M_{\text{ej}} \frac{\int D \mathbf{v}_{\text{plane}} dx dy}{\int D dx dy}, \quad (5.1)$$

where the integrals here are restricted to the orbital plane (while  $M_{\text{ej}}$  is computed from the integral of the rest-mass density  $D$  of the unbound matter over all three dimensions) and  $\mathbf{v}_{\text{plane}}$  denotes the ejecta velocity in the orbital plane (i.e., just the  $x$  and  $y$  components). We find that  $v_{\text{kick}}^{\text{ej}} = \|\mathbf{P}_{\text{ej}}\|/M \sim 100 - 1000 \text{ km s}^{-1}$ . This number is also consistent with the one obtained from the coordinate position of the SMNS. However, the value should just be seen as an order of magnitude estimate, where the main difficulties here are the low resolution, the long simulation time, and the gauge dependence of the measurement. Since this is an unequal-mass system, we also expect some contribution to the kick from anisotropic gravitational wave emission. We compute this from the GW linear momentum flux,

$$\mathbf{v}_{\text{kick}}^{\text{GW}} = -\frac{1}{M} \int \dot{\mathbf{P}}_{\text{GW}} dt \quad (5.2)$$

where the linear momentum flux  $\dot{\mathbf{P}}_{\text{GW}}$  is computed as in [51]. We find  $v_{\text{kick}}^{\text{GW}} \simeq 100 \text{ km s}^{-1}$  at merger. The GW kick is smaller than the ejecta kick, as is found in black hole-neutron star simulations [98, 99].

### 3. Gravitational waves

Let us discuss the gravitational waveform. The four dominant modes of the gravitational waveform are presented in Fig. 14. The inspiral-merger signal ends at  $u_{\text{mrg}} = 2692M$ , and we find no evidence for an obvious GW signature of the mass transfer described above. We study the effect of the mass-ratio on the GW multipolar

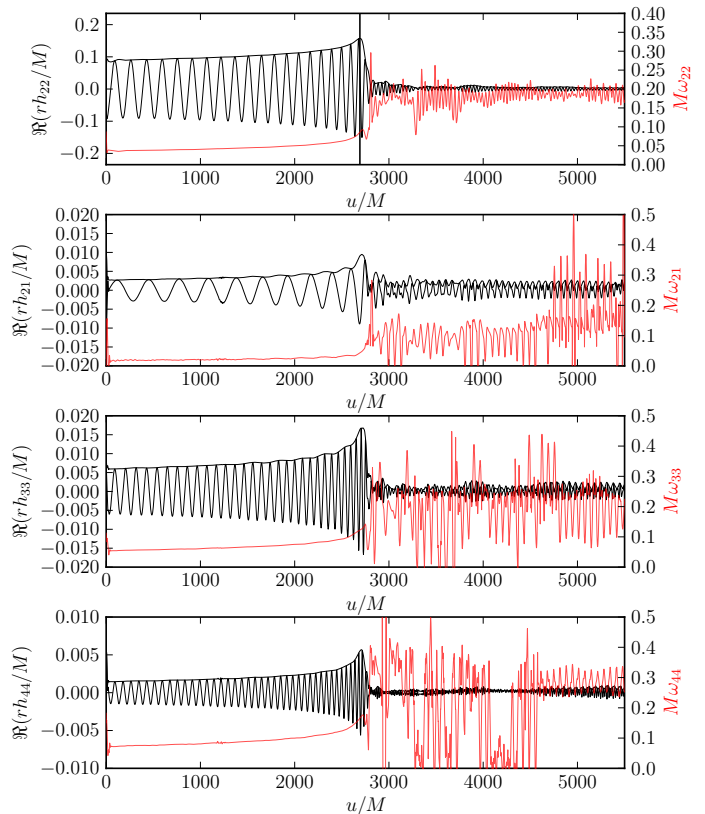


FIG. 14: The four dominant multipoles of the GWs from the  $q = 2.06$  simulation, viz.,  $(l, m) = (2, 2)$ ,  $(2, 1)$ ,  $(3, 3)$ , and  $(4, 4)$ . We plot the real part of the modes in black and show the dimensionless GW frequency for all modes in red. In the top plot, the solid vertical line marks the merger. The frequency oscillations are in part unphysical and resolution dependent. The large frequency spikes in the post-merger phase are caused by zeros of the amplitude.

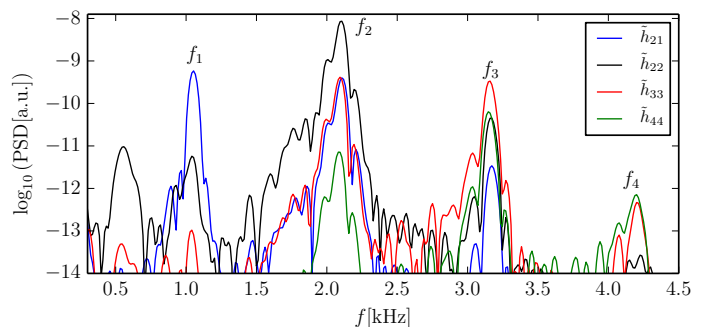


FIG. 15: Power spectrum density for the dominant postmerger modes of the  $q = 2.06$  simulation. We used a time interval  $u \in [3800M, 5700M]$  for the computation, and therefore focus only on the SMNS spectrum. The harmonicity of the frequencies  $f_1, f_2, f_3, f_4$  is clearly visible.

structure by computing the relative GW energy contribution of each dominant mode over the total energy released up to merger ( $E_{lm}/E$ ) and comparing with the  $q = 1$  case with the same EOS [100] (though with a slightly different total mass: 2.70, as opposed to 2.89 for the  $q = 2.06$  simulation; the  $q = 1$  system also radiates almost 40% more energy per total mass than the  $q = 2.06$  system). We find

that for the  $q = 1$  simulation  $\sim 99.6\%$  of the energy is released in the  $(2, 2)$ -mode, while  $\sim 98\%$  is released for MS1b-q206. For  $q = 1$  the  $(2, 1)$  and the  $(3, 3)$  modes are zero by symmetry; for  $q = 2.06$  the  $(2, 1)$  mode releases about  $\sim 0.08\%$  of the energy and the  $(3, 3)$  mode  $\sim 1.4\%$ . The next dominant mode,  $(4, 4)$ , contributes to  $\sim 0.19\%$  of the total energy for  $q = 1$  and  $0.22\%$  for  $q = 2.06$ .

Finally, we study the postmerger GW frequencies for the dominant modes. We perform a Fourier analysis on the interval  $u \in [3800M, 5700M]$  in Fig. 15. The  $f_2$  frequency [the dominant frequency of the  $(2, 2)$  mode] is clearly visible in all modes (though it may not be dominant) and is close to  $f_2 = 2.09\text{kHz}$  ( $Mf_2 = 0.0298$ ).  $f_2$  agrees within  $2.5\%$  with the relation presented in [101], which indicates the robustness of the fit given there even for high mass ratios. Comparing with the  $q = 1$  case, we do not find a significant difference in the  $f_2$  value. Inspection of the peaks of the other modes, reveal that the  $f_k$  frequencies are harmonic to a very high accuracy, i.e.,  $f_1 = f_2/2 = f_3/3 = f_4/4$ . In particular we have  $f_1 = 1.05\text{ kHz}$  ( $Mf_1 = 0.0150$ ),  $f_3 = 3.16\text{ kHz}$  ( $Mf_3 = 0.0449$ ),  $f_4 = 4.20\text{ kHz}$  ( $Mf_4 = 0.0598$ ). The agreement is better than  $1\%$ , though the uncertainties in the frequencies are larger than this, about  $0.15\text{ kHz}$  and are mainly caused by a shift of the frequencies over time due to the changing compactness of the neutron star. This harmonicity was also found in [102], though there they obtained the mode frequencies from a Fourier transform of the pressure and used the spatial conformal flatness approximation in their simulation. Here we have verified that the same harmonicity is present in an observable quantity (the modes of the gravitational radiation) in a fully relativistic simulation.

## B. A precessing unequal mass binary

In this section we investigate the evolution of a BNS system with a rather generic spin configuration and  $q = 1.22$ . The CRV angular velocity  $\omega^i$  for star A and star B is set as  $\omega = 0.005(1, 1, 1)$ , i.e., their spins both point at an angle of  $45^\circ$  to the orbital angular momentum. This evolution is the first precessing BNS merger simulated in numerical relativity. We indicate this precessing spin configuration with  $\text{SLy}^{(\nearrow \nearrow)}$  as we use the SLy EOS (Tab. I). The dimensionless spin magnitudes are  $j^A \simeq 0.13$  and  $j^B \simeq 0.16$ . Although such high spins are not observed in double neutron star systems so far, there is no physical reason to exclude such a scenario. In particular, binary neutron star systems with spins misaligned from the orbital angular momentum, as here, are more likely to form dynamically in dense stellar regions, such as globular clusters, where there are many rapidly spinning neutron stars, as is discussed in Appendix A 2. The stars have baryonic masses of  $M_b^A = 1.5$  and  $M_b^B = 1.2$ ; the gravitational masses are  $M^A = 1.3553$  and  $M^B = 1.1072$ .

Together with  $\text{SLy}^{(\nearrow \nearrow)}$  we evolve for comparison two other configurations with the same baryonic masses (and  $q$ ) but with the CRV angular velocity set to  $\omega = 0.005(0, 0, 1)$  ( $\text{SLy}^{(\uparrow \uparrow)}$ ), and  $\omega = 0.0$  ( $\text{SLy}^{(00)}$ ). Thus  $\text{SLy}^{(\uparrow \uparrow)}$  has no precession, and  $\text{SLy}^{(00)}$  no spin interac-

tions at all.

All the SGRID data are computed with  $n_A = n_B = 28$ ,  $n_\varphi = 8$ ,  $n_{\text{Cart}} = 24$ . We have not tried to reduce the eccentricity for this particular setup to save computational resources. The residual eccentricity of the precessing system is  $\hat{e}_d \simeq 4 \times 10^{-3}$ ,  $\hat{e}_{\text{GW}} \simeq 5 \times 10^{-3}$  for the two eccentricity measures considered in Sec. IV C. The resolution in the finest level covering the neutron star is  $h_6 = 0.245$ , similar to the low resolution setups of [100, 103, 104], but no symmetries are applied to the grid (full 3D). Thus, although the principal dynamics are properly modeled at this resolution, quantitative statements come with quite large uncertainties.

### 1. Dynamics

Figure 16 (upper and lower left) shows the coordinate tracks (positions of the local minimum of the lapse) of the neutron stars in the  $\text{SLy}^{(\nearrow \nearrow)}$  simulation. The change of the orbital plane due to the misaligned spin of the binary neutron stars is clearly visible. This effect can also be seen in the change of the  $z$ -coordinate over time (upper right panel). During the inspiral approximately one precession cycle is finished, i.e., the orbital plane again coincides (approximately) with the  $xy$ -plane during merger.

We present the evolution of the  $L^2$  norm of the Hamiltonian constraint in the upper panel of Fig. 17 and of the rest mass conservation in the lower panel. Because of the constraint propagation and damping properties of the Z4c scheme, the constraint violations stay at or below the value of the initial data. The rest mass conservation over the entire simulation is up to  $\sim 0.3\%$ . Overall, these diagnostics indicate the errors in the simulation are under control. The small violation of rest-mass conservation is related to the artificial atmosphere and the relatively low resolution we employed; see the discussion in [36].

The initial angular momentum of the system is  $\mathbf{J}_{\text{ADM}}(t = 0) = (0.251, 0.239, 6.951)$  or normalized  $\hat{\mathbf{J}} = (0.0361, 0.0343, 0.9989)$ . We find that  $\hat{\mathbf{J}}$  changes slightly over the entire simulation, which is to be expected, as the total angular momentum precesses slightly in post-Newtonian calculations, as discussed in, e.g., [105]. We can estimate the opening angle of the precession cone (neglecting spin-spin effects) using Eq. (51) from [105] and evaluating everything at  $t = 0$ , using the initial orbital frequency to evaluate  $M/r$  to 1PN order. We calculate the orbital angular momentum by subtracting the spin angular momenta of the two stars in isolation from the ADM angular momentum. Using this method, we obtain (as a first approximation) an opening angle of the precession cone of  $\lambda_J \simeq 1.3 \times 10^{-3}$ . Due to the decreasing orbital separation over the evolution, we expect that the opening angle should be slightly larger in our full GR simulation. In fact, this can be observed and we find an angle of  $\sim 1.5 \times 10^{-3} \simeq 0.086^\circ$ , where the numerical uncertainty is  $\lesssim 10^{-4}$  based on comparison with simulations without precession. The opening angle of the precession cone for the orbital angular momentum is  $\lambda_L \sim 0.05$ , from a simple calculation of the initial angle between the orbital and total angular momenta, which agrees with the

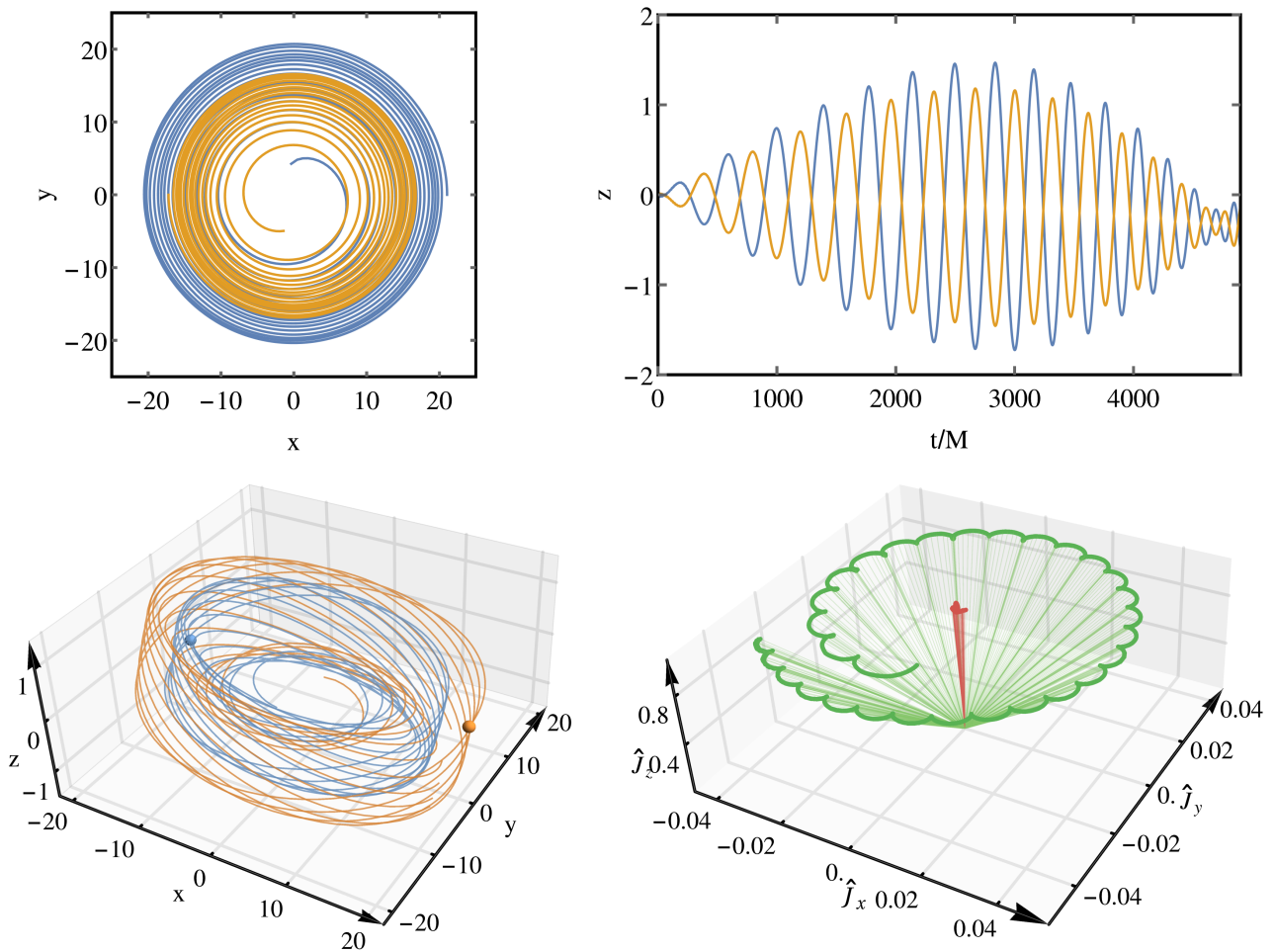


FIG. 16: Orbital dynamics of the precessing binary neutron star inspiral. Upper left: neutron star tracks in the  $xy$ -plane. Upper right:  $z$ -coordinates of the stars' centers as a function of the coordinate time  $t$ . Lower left: 3D neutron star tracks visualizing the precession of the orbital plane, where the spheres denote the original positions of the stars. Lower right: Precession and nutation of the orbital angular momentum  $\hat{\mathbf{L}}$  (green lines). The coordinate system is rotated such that  $\hat{\mathbf{J}}(t=0)$  lies along the  $z$ -axis. The orbital angular momentum performs slightly more than one precession cycle with a period of  $T_{\text{precess}} \simeq 4720M$ . The opening angle  $\lambda_L$  decreases from  $\sim 0.05 \simeq 3^\circ$  to  $\sim 0.035 \simeq 2^\circ$  over the inspiral. The direction of the total angular momentum also precesses at the same period with a considerably smaller opening angle of  $\lambda_J \simeq 1.5 \times 10^{-3} \simeq 0.086^\circ$  (red lines).

initial opening angle found in our simulation. The opening angle  $\lambda_L$  decreases from  $\sim 0.05 \simeq 3^\circ$  to  $\sim 0.035 \simeq 2^\circ$  over the inspiral.

The lower right panel of Fig. 16 presents the precession of the orbital plane, as given by the direction of the orbital angular momentum. The effects of precession and nutation are clearly visible. The normalized orbital angular momentum  $\hat{\mathbf{L}}$  we plot in this figure is constructed as the vector orthogonal to the orbital plane, which we estimate using the coordinate line between the two star centers at two adjacent timesteps. To minimize high frequency noise we apply a low-pass filter. The precession period is  $T_{\text{precess}} \simeq 4720M$ , which agrees within  $\lesssim 10\%$  with the PN estimates, based on a PN evolution similar to the discussion in [70].<sup>7</sup>

Binding energy vs. reduced orbital angular momentum curves provide a gauge-invariant way of characterizing the binaries' dynamics [38, 66, 100]. In order to compute such curves, we modify Eqs. (4.1) and (4.2) to take the emitted energy and total angular momentum of the GWs into account; see, e.g., Eqs. (12) and (13) in [38]. Energy curves for  $\text{SLy}^{(\nearrow\nearrow)}$ ,  $\text{SLy}^{(\uparrow\uparrow)}$ , and  $\text{SLy}^{(00)}$  are shown in Fig. 18, together with their pairwise differences (bottom panel).

The differences between the spinning configurations and  $\text{SLy}^{(00)}$  essentially quantify the repulsive spin-orbit (SO) interaction contribution to the binding energy, which is the dominant one for the dynamics. The energetics of  $\text{SLy}^{(\nearrow\nearrow)}$  are quite close to those of  $\text{SLy}^{(\uparrow\uparrow)}$ . This happens because the leading order SO terms ( $\propto \mathbf{L} \cdot \mathbf{S}_i / r^3$ )

<sup>7</sup> The formulation of [70] uses non-spinning terms at the 3.5PN level, SO terms up to 4PN, spin-spin terms up to 2PN, and for

the precession SO contributions up to the next-to-next-to-leading order are included.

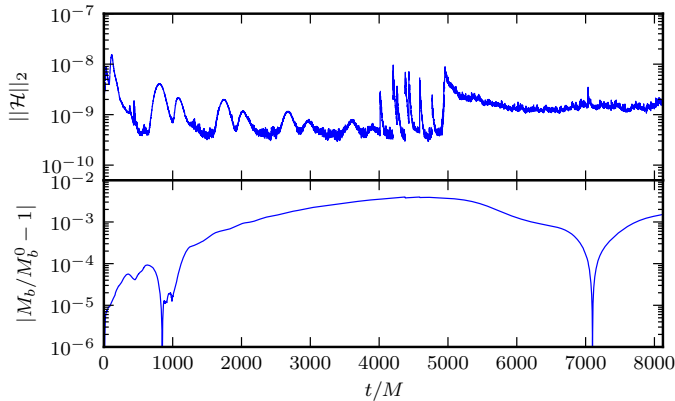


FIG. 17:  $L^2$  norm of the Hamiltonian constraint (upper panel) and baryonic mass conservation (lower panel). Quantities are computed in level  $l = 1$ , i.e., the outermost Cartesian box of the numerical domain.

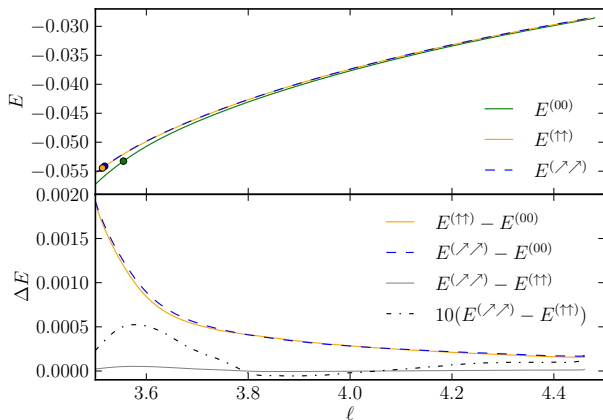


FIG. 18: Binding energy as a function of the reduced orbital angular momentum for the precessing simulation  $\text{SLy}^{(\nearrow\searrow)}$  (blue dashed),  $\text{SLy}^{(00)}$  (solid orange), and  $\text{SLy}^{(\uparrow\uparrow)}$  (solid green). The bottom panel reports differences between the curves.

are identical in the initial data for  $\text{SLy}^{(\nearrow\searrow)}$  and  $\text{SLy}^{(\uparrow\uparrow)}$ .<sup>8</sup> During the evolution, the difference between the SO interactions of  $\text{SLy}^{(\uparrow\uparrow)}$  and  $\text{SLy}^{(\nearrow\searrow)}$  is solely due to the slight changes in the projection of the spins onto the angular momentum as they precess. For distances  $d \sim 16 - 8$  this corresponds to corrections on the order of  $10^{-4}$  to the binding energy. The leading order spin-spin (SS) contribution ( $E_{SS} = [3(\mathbf{n} \cdot \mathbf{S}_1)(\mathbf{n} \cdot \mathbf{S}_2) - (\mathbf{S}_1 \cdot \mathbf{S}_2)]/r^3$ , where  $\mathbf{n}$  denotes the unit vector pointing from one star to the other) is exactly zero in the  $\text{SLy}^{(\nearrow\searrow)}$  initial data and order  $10^{-6}$  in the  $\text{SLy}^{(\uparrow\uparrow)}$  initial data. During evolution the SS contribution of  $\text{SLy}^{(\nearrow\searrow)}$  is of the order  $\sim 10^{-5}$ . This explains the differences between  $\text{SLy}^{(\nearrow\searrow)}$  and  $\text{SLy}^{(\uparrow\uparrow)}$  at the level of  $\sim 10^{-4} - 10^{-5}$  due to these SO and SS corrections, which can be observed in Fig. 18. However, significant differences between  $\text{SLy}^{(\nearrow\searrow)}$  and  $\text{SLy}^{(\uparrow\uparrow)}$  can be

observed in some of the higher modes, notably the  $(2, 1)$  mode, as we shall see in the following.

## 2. Gravitational Waves

We present the three largest amplitude modes of the GW signal in Fig. 19. As in the nonprecessing case, the dominant emitter of GWs is the  $(2, 2)$ -mode. However, interesting physical aspects are present in the subdominant modes. The amplitude of the  $(2, 1)$ -mode is modulated by the precession period, giving a second possibility to extract the value of that period, which agrees with the estimate given above. Additionally, the amplitude of the modulation we observe is consistent with the expected contribution to the  $(2, 1)$ -mode from the binary's dominant mass quadrupole radiation [which only appears in the  $(2, 2)$ -mode for nonprecessing systems] due to the precession of the orbital plane. In particular, since the initial angle between the total and orbital angular momenta is small in this case,  $\lambda_L := \angle(\hat{\mathbf{L}}, \hat{\mathbf{J}}) \simeq 0.05$ , decreasing slightly over the evolution, as discussed in the previous section (see also Fig. 16), one can work to linear order in  $\lambda_L$ , where one finds that the maximum amplitude of the mass quadrupole's contribution to the  $(2, 1)$ -mode is  $2\lambda_L$  times the amplitude of the Newtonian mass quadrupole radiation.<sup>9</sup> One obtains the expression for the maximum mass quadrupole contribution to the  $(2, 1)$  mode by noting that  $2\lambda_L$  is the largest angle the orbital angular momentum (originally aligned with the  $z$ -axis to a very good approximation) makes with the  $z$ -axis; cf. the PN expressions for the modes expanded in  $\iota$  in Eqs. (4.17) of [107]. (Note that  $\iota$  is defined as the angle between the orbital angular momentum and the initial total angular momentum, which they take to be along the  $z$ -axis in the coordinate system they use to define the mode decomposition.) Of course, there are contributions to the  $(2, 1)$  mode from the current quadrupole, as well, but these are much smaller than the contribution due to precession, as is seen in Fig. 19, since the current quadrupole contributions are suppressed by a factor of  $v\delta$  compared to the Newtonian mass quadrupole radiation.

The systems finally merges after  $\sim 30$  GW cycles [in the  $(2, 2)$  mode] at a frequency of  $M\omega_{22}^{\text{mrg}} \sim 0.128$  (solid vertical line in upper left panel; for consistency with our previous work, we define the merger as the maximum of  $|h_{22}|$ ) at  $t = 4927M$ .

Comparing  $\text{SLy}^{(\nearrow\searrow)}$  with the other two simulations, we observe two main differences during the inspiral. First, without spin the merger happens earlier at  $t = 4839M$ , due to the fact that no repulsive spin-orbit interaction is present. In case of the  $\text{SLy}^{(\uparrow\uparrow)}$  simulation, the merger happens at  $t = 4960M$ , which agrees within  $\Delta t = 33M$

<sup>8</sup> The following discussion is based on leading-order PN expressions for the binding energy that can be found in, e.g., Eq. (2.7) of [106].

<sup>9</sup> Similarly, the amplitude of the  $(2, 2)$ -mode is the same as the amplitude of the Newtonian mass quadrupole radiation up to corrections that are suppressed by factors of  $v\lambda_L\delta$ ,  $v^2$ , or  $\lambda_L^2$ , where  $v$  is the binary's orbital velocity and  $\delta := (M^A - M^B)/M \simeq 0.1$ .



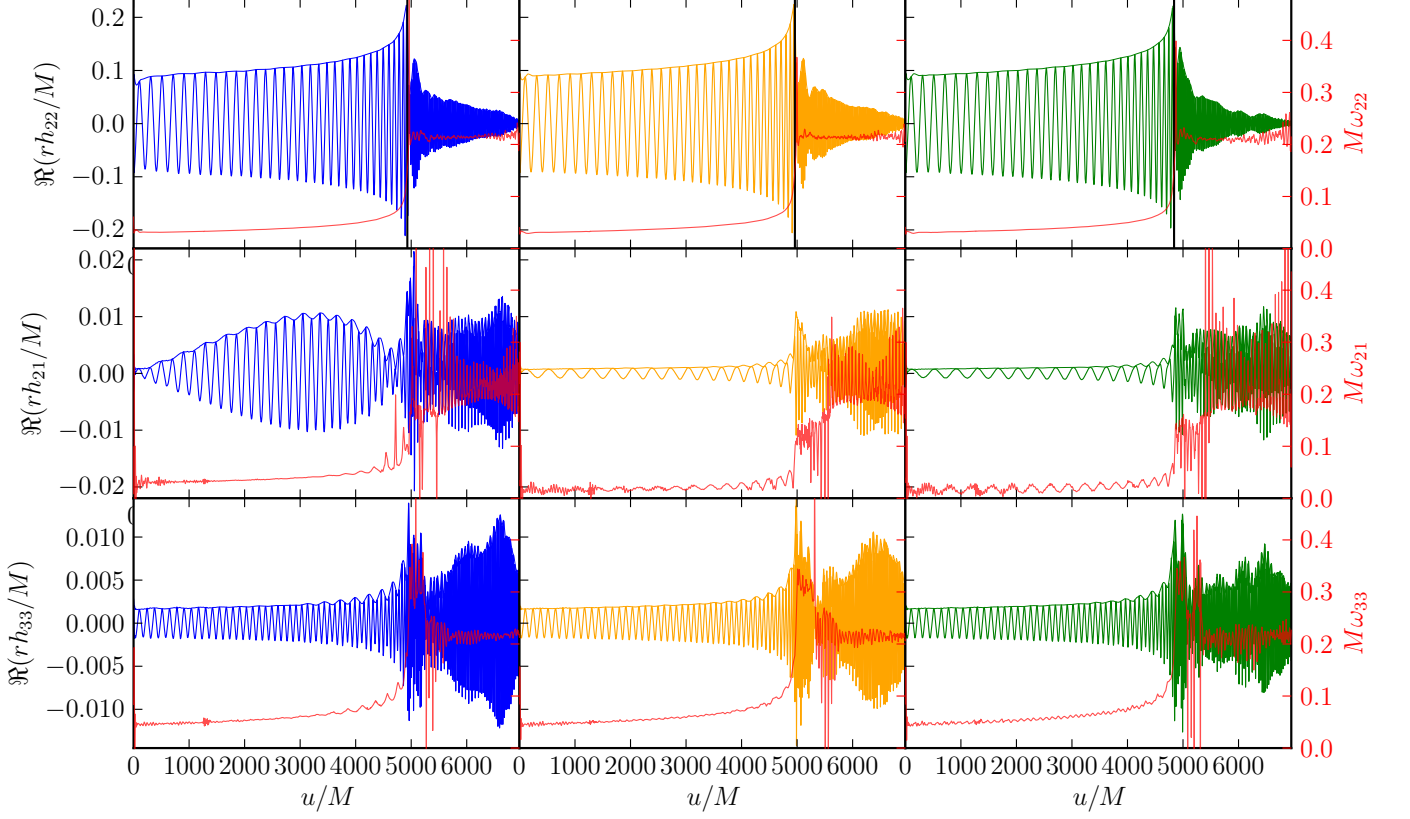


FIG. 19: The three most dominant multipoles of the GW  $(l, m) = (2, 2), (2, 1), (3, 3)$  for  $\text{SLy}^{(\nearrow \nearrow)}$  (left panels),  $\text{SLy}^{(\uparrow \uparrow)}$  (middle panels), and  $\text{SLy}^{(00)}$  (right panels). We plot the real part of the modes and the dimensionless GW frequency in red. In the upper plots, the solid vertical lines mark the moment of merger (i.e., the maximum of  $|h_{22}|$ ), where a later merger in the two cases with spin is seen, due to the spin-orbit interaction. We observe that the  $(2, 1)$  mode in the precessing case is dominated by the large contribution from the mass quadrupole at twice the orbital frequency due to the precession of the orbital plane, while it only has the much smaller contribution from the current quadrupole at the orbital frequency in the two nonprecessing cases. We extracted the wave at a radius of  $r = 446M$ . Some very small noise in the frequency at early times is visible and due to reflections at the boundary. After merger, the frequency calculation is less accurate and affected by larger oscillations, mostly unphysical.

with the precessing simulation. The second observation is that the amplitude of the  $rh_{21}$  is much smaller than for the precessing simulation. The non-zero amplitude is caused by the unequal masses of the two stars, but no clear imprint of the spin is visible (cf. the middle and right panels). Due to the small amplitude of the  $(2, 1)$  mode in the nonprecessing simulations it is not very well resolved, which is clearly visible in unphysical sinusoidal oscillations of the frequency. The same holds to a lesser extent for the  $(3, 3)$ -mode. Additionally, the large frequency spikes present in the post-merger phase of the subdominant modes are caused by zeros of the amplitude.

In order to further assess the differences between the  $\text{SLy}^{(\nearrow \nearrow)}$  and  $\text{SLy}^{(\uparrow \uparrow)}$  waveforms, we compare the nonprecessing data to the precessing ones after transformation to the precessing frame. The transformation is performed with a method similar to the one used in binary black hole simulations in [53], and the main result is shown in Fig. 20. In particular, the rotation of the  $\Psi_{4\ lm}$  multipoles reads (Eq. (A9) in [53])

$$\tilde{\Psi}_{4\ lm} = \sum_{m'=-l}^l e^{im'\gamma} d_{m'm}^l(-\beta) e^{im\alpha} \Psi_{4\ lm'}, \quad (5.3)$$

where  $d_{m'm}^l$  are the Wigner  $d$ -matrices. We focus on the  $(2, 1)$  and  $(2, 2)$  modes and perform the rotation as follows: (i) we look for the Euler angles  $\beta, \gamma$  for which  $|\tilde{\Psi}_{4\ 21}|$  is minimal (Ref. [53] maximizes  $|\tilde{\Psi}_{4\ 22}|^2 + |\tilde{\Psi}_{4\ 2-2}|^2$ ); (ii) we split the dataset in several chunks (vertical dashed lines in Fig. 20) and fit the obtained Euler angles with low-order polynomials. This step optimizes the fits and minimizes numerical oscillations. We do not need to worry about the third Euler angle  $\alpha$  here, as it is irrelevant in the case we consider, where we only look at the magnitude of the modes of  $\tilde{\Psi}_4$ . From Fig. 20 one sees that  $|\tilde{\Psi}_{4\ 2m}^{(\nearrow \nearrow)}|$  (i.e., the version in the nonprecessing frame) is almost equivalent to  $|\Psi_{4\ 2m}^{(\uparrow \uparrow)}|$ . The effect is very clear in the  $(2, 1)$  mode. This preliminary result suggests it will be possible to model precessing BNS waveform using aligned spin BNS models for moderate spin magnitudes (cf. [53]).

The merger remnant is a hypermassive neutron star (HMNS), which mostly emits in the  $(2, 2)$  channel at early times. After  $t \approx 5900M$  the amplitude of the  $(2, 2)$  mode decreases until the  $(2, 1)$  and  $(3, 3)$  modes have the same amplitude as the  $(2, 2)$  mode. Note that at this time

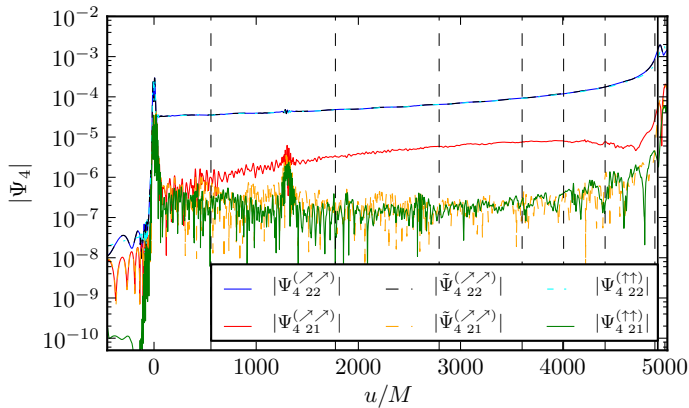


FIG. 20: Amplitude of the (2,2) and (2,1) modes of  $\Psi_4$  for the  $\text{SLy}^{(\nearrow\searrow)}$  and  $\text{SLy}^{(\uparrow\uparrow)}$  simulations, along with the same amplitudes for  $\text{SLy}^{(\nearrow\searrow)}$  in the nonprecessing frame (denoted by  $\tilde{\Psi}_4$ ) obtained as in [53]. Note that we only consider the inspiral here. The transformation is done in chunks (separated by vertical dashed lines). The agreement between  $|\tilde{\Psi}_4^{(\nearrow\searrow)}|$  and  $|\Psi_4^{(\uparrow\uparrow)}|$  after transformation to the non-precessing frame is clearly visible. The noise around  $u \approx 1500M$  is caused by reflections of the outer boundary.

the (2,0) and (4,4) modes also have comparable amplitudes. We find a frequency shift of the  $f_2$ -frequency [the dominant frequency in the (2,2) mode] of  $\sim 60$  Hz due to the additional angular momentum of the HMNS formed by the spinning configurations; the origin of such frequency shifts was discussed in detail in [38]. The estimated  $f_2$ -frequencies are 2.75, 2.79, and 2.81 kHz, for  $\text{SLy}^{(00)}$ ,  $\text{SLy}^{(\uparrow\uparrow)}$ , and  $\text{SLy}^{(\nearrow\searrow)}$ , respectively.

### C. Effect of eccentricity reduction on waveform phasing

Although an eccentricity reduction procedure for BNS quasicircular initial data has been already presented in [29], its performance on the relevant observable quantity, i.e., the GW phase and amplitude, has not been evaluated directly. Here, we investigate the effect of eccentricity reduced data on the GW phasing and amplitude by a direct comparison with data in which eccentricity reduction has not been performed. Such a comparison is particularly important since the eccentricity reduction procedure is computationally expensive and might be not necessary for certain applications or when the data are affected by larger uncertainties due, for example, to truncation errors.

We compare the GW phase of two  $\text{SLy } q = 1$  runs: In one case we evolve initial data with  $\hat{e}_d = 1.241 \times 10^{-2}$  (Iter 0) and in the other data with  $\hat{e}_d = 8.7 \times 10^{-4}$  (Iter 3); see Table II.

We focus on the  $\ell = m = 2$  multipole and omit the subscript in the waveform quantities. Waveforms are aligned on the interval  $[t_1, t_2] = [1000, 6000] \simeq [370M, 2222M]$  shifting by constant time and phase offsets  $T, \Phi$ . The

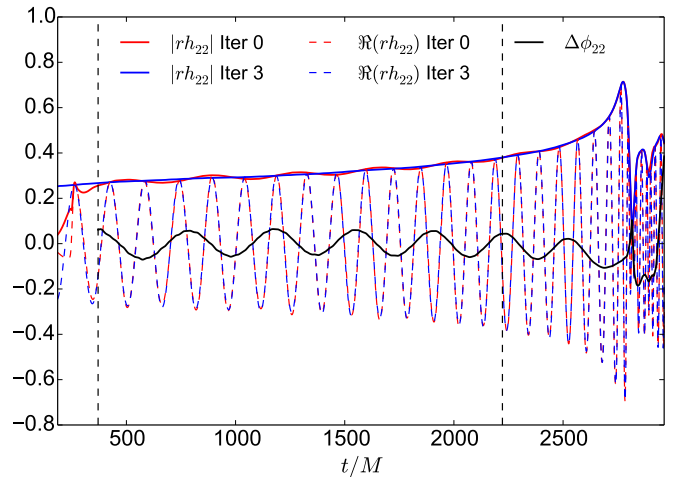


FIG. 21: GW phasing of the evolved initial data without (Iter 0) and with (Iter 3) eccentricity reduction for the  $\text{SLy } q = 1$  configuration. Vertical dotted lines denote the region over which we align the waveforms.

latter are determined by minimizing the function [108]

$$G(T, \Phi) = \int_{t_1}^{t_2} |\phi_1(t) - \phi_2(t + T) - \Phi|^2 dt, \quad (5.4)$$

where  $\phi_{1,2}$  denotes the GW phase of the two datasets. A more robust alignment procedure based on a frequency interval can also be used [100], but the current procedure is sufficient for our purposes.

We present the results in Fig. 21. The phase difference  $\Delta\phi_{22}$  oscillates between  $[-0.06, 0.06]$  rad during the  $\sim 21$  GW cycles, and it is essentially flat up to merger,  $t \simeq 2780M$ . Similarly, the amplitude of the non-eccentricity reduced data (Iter 0) oscillates around the eccentricity reduced ones (Iter 3); the amplitude oscillations are  $\sim 5\%$  at early times  $t \sim 370M$  and decrease as the system approaches merger.

Overall, these results show that the use of eccentricity reduced data with  $\hat{e}_d \sim 10^{-4}$  (about 3 iterations of our procedure) improves the waveform quality for GW modeling purposes, and should be employed in future precision studies of the gravitational waveform. However, eccentricity reduction is likely to be effective only if combined together with an improvement of other source of errors, notably truncation errors. We notice in this respect that  $\Delta\phi \sim 0.12$  rad is at least a factor two smaller than the typical uncertainty introduced by truncation errors at the resolutions employed here [100].

## VI. CONCLUSIONS

Due to advances in the construction of constraint solved and consistent initial data, simulations of binary neutron stars in full general relativity are now able to cover more of the binary neutron star parameter space accurately. In particular, it is now possible to study different EOS [40–42], large mass ratios [36, 37], spinning neutron star configurations [38], highly eccentric setups [17],

and neutron stars on orbits with less residual eccentricity than the standard ones [29, 109]. We have recently upgraded the SGRID code to be able to generate consistent, constraint-solved initial data with the ability to vary all these parameters.<sup>10</sup> The most noteworthy improvement was the combination of the constant rotational velocity approach (from [23]) with a generic specification of the symmetry vector (from [17]) allowing arbitrary eccentricities (including eccentricity reduction).

In this paper, we have exhibited SGRID’s ability to generate binary neutron star initial data for many situations of interest and included dynamical simulations of some generic configurations evolved with the BAM code.

### A. Quasi-equilibrium sequences

We have constructed the following quasi-equilibrium setups:

*Binaries in the constant rotational velocity approach.* With the help of quasi-equilibrium sequences we studied spinning neutron star configurations for different equations of state and characterized the spin-orbit contribution to the binding energy. Our results show that the spin-orbit interaction can be well approximated by post-Newtonian theory within the uncertainty of our numerical method.

*Highly eccentric binaries.* We also constructed highly eccentric sequences following the description of [17], but with the advantage of solving the elliptic equation for the velocity potential, which results in smaller artificial density oscillations by a factor of  $\sim 5$ . This will allow a more detailed analysis of tidally-induced oscillations in the neutron stars than was performed in [30] using superposed initial data, which led to much larger initial oscillations. Additionally, we compared our eccentric sequences with PN calculations in various ways, where our analysis showed that, as expected, close agreement is only obtained in the limit of large separations or small eccentricities.

*Eccentricity reduced binaries.* We can use the same technology that allows us to create highly eccentric orbits to reduce the eccentricity present in standard binary neutron star initial data constructed using a helical Killing vector. Here we iteratively adjust our eccentricity and radial velocity parameters, similar to the procedure presented in [29].

*Varying compactnesses and mass-ratios.* As additional parameters, we considered different mass ratios and compactnesses. We were able to construct a sequence for a mass ratio of  $q = 2.06$  and equal-mass binary neutron

stars with compactness up to  $C = 0.23$ .

This shows that with its recent upgrades, SGRID allows one to construct binary neutron star configurations in a substantial portion of the possible inspiral parameter space (and one can vary all the relevant parameters independently). Of course, there is a considerable amount of physics that we do not include here. However, the physics we have neglected does not affect the inspiral at a level that can be detected via gravitational waves for the parameter values expected to be present in neutron star binaries. Nevertheless, this missing physics can still play an important role in the merger or potentially produce other interesting effects, and includes magnetic fields, elasticity (e.g., in the solid crust), and composition, all of which would need to be appropriately incorporated in the initial data. Of this additional physics, the inclusion of magnetic fields is likely the most pressing. Unfortunately, there is no known method for including magnetic fields consistently in constraint-solved initial data: All simulations of magnetized binary neutron stars (e.g., [43–47]) add the magnetic field by hand after constraint solving. Developing such a method would be a useful advance in binary neutron star initial data construction.

### B. Dynamical Evolutions

To ensure that the constructed data are suitable for dynamical simulations, we have evolved three configurations.

$q = 2.06$  *run.* As a first example, we evolved the highest mass ratio ever considered in a full general relativistic binary neutron star configuration. The configuration consisted of a  $q = 2.06$  setup with the MS1b EOS. Because of the high mass ratio and the rather stiff EOS, we observed mass transfer between the two stars several revolutions before merger. During this process material with a rest-mass of  $\sim (2 - 3) \times 10^{-2} M_\odot$  is transferred, with an average accretion power of  $\sim 10^{53}$  erg s<sup>-1</sup>. During the merger process,  $\sim 7.6 \times 10^{-2} M_\odot$  get unbound and are released from the system with a kinetic energy of  $\sim 4 \times 10^{50}$  erg. The ejecta process happens primarily due to torque in the tidal tail of the lower massive star and forms a spiral like pattern. Due to this anisotropic ejection of material, the merger remnant receives a large kick of  $O(100)$  km s<sup>-1</sup>. The final merger remnant can be characterized as a supramassive neutron star, which is not expected to collapse on dynamical timescales. An investigation of the merger remnant’s GW spectrum, including more than just the dominant (2, 2)-mode, reveals that many of the peak frequencies are harmonically related to high accuracy.

*Precessing and unequal masses run.* As a second example, we considered the first precessing binary neutron star merger simulation. Contrary to most BNS investigations (except, e.g., [66, 110]) we present more than just the dominant (2, 2) mode and find a clear imprint of the precession in the subdominant (2, 1) mode, where the am-

<sup>10</sup> Note that here we only consider the “inspiral parameter space,” consisting of the purely relativistic hydrodynamic parameters (eccentricity, masses, spins, and EOS) that can be measured with an inspiral gravitational wave signal with current or proposed gravitational wave detectors in physically expected scenarios.

plitude is modulated by the precession frequency. Considering for comparison a simulation with the same leading-order spin-orbit interaction, we show that the relation between the gauge-invariant binding energy vs. reduced orbital angular momentum up to the merger exhibits only a minor imprint of the precession for the spin magnitudes we consider. Regarding the post-merger GW spectrum, we observed a frequency shift of the dominant  $f_2$  mode due to the spins of the binary’s components (cf. [38]).

*Reduced eccentricity run.* Finally, we have performed simulations of an equal-mass configuration with and without eccentricity reduced initial data and we have quantified the differences in the waveform’s amplitude and phase. We found that although the eccentricity reduction improves the waveform quality, one also needs to reduce other errors in the waveforms, notably truncation errors, in order for the improvement due to eccentricity reduction to be effective.

### Acknowledgments

It is a pleasure to thank Roland Haas, Michael Kramer, Alessandro Nagar, Jan Steinhoff, Maximiliano Ujevic for helpful discussions and valuable comments. We are particularly indebted to Patricia Schmidt for her help understanding the precession effects on the waveform. This work was supported in part by DFG grant SFB/Transregio 7 “Gravitational Wave Astronomy,” the Graduierten-Akademie Jena, and the DFG Research Training Group 1523/1 “Quantum and Gravitational Fields.” N.K.J.-M. acknowledges support from the AIRBUS Group Corporate Foundation through a chair in “Mathematics of Complex Systems” at the International Centre for Theoretical Sciences. S.B. acknowledges partial support from the National Science Foundation under grant numbers NSF AST-1333520, PHY-1404569, and AST-1205732. C.M. was supported by the STFC grant PP / E001025 / 1. W.T. was supported by the National Science Foundation under grant PHY-1305387. The authors also gratefully acknowledge the Gauss Centre for Supercomputing e.V. for funding this project by providing computing time on the GCS Supercomputer SuperMUC at Leibniz Supercomputing Centre and the computing time granted by the John von Neumann Institute for Computing provided on the supercomputer JU-ROPA at Jülich Supercomputing Centre. We also acknowledge usage of computer time on the Fermi CINECA machine allocated through the ISCRA initiative. Additionally, this work used the Extreme Science and Engineering Discovery Environment, which is supported by National Science Foundation grant number ACI-1053575, computer resources at the Institute of Theoretical Physics of the University of Jena, and the HPC cluster KOKO at Florida Atlantic University.

### Appendix A: Astrophysical predictions for more extreme masses, mass ratios, and spins for binary neutron stars

Here we assess the prospects for binary neutron star mergers with more extreme masses and spins—such as those we simulated in Sec. V—actually occurring in nature. (Note that this assessment only covers the masses and spin magnitudes, not the equation of state or spin misalignment.)

#### 1. Large and small masses and larger mass ratios

There is good evidence that the population of neutron stars in the universe extends at least from  $\sim 1M_\odot$  up to  $2M_\odot$ . In particular, there are two precise measurements of high-mass ( $\sim 2M_\odot$ ) neutron stars in binaries with white dwarfs [63, 64] as well as some less precise measurements of low-mass ( $1M_\odot$ ) neutron stars in X-ray binaries [111, 112]. There are also recent measurements of low compactnesses for isolated neutron stars [113], which would imply quite small masses  $\sim 1M_\odot$  for many of the equations of state we consider.<sup>11</sup> Additionally, there is recent work that suggests that the initial (pre-accretion) mass of the low-mass millisecond pulsar J0751+1807 (whose present mass is  $1.26 \pm 0.12M_\odot$ ) could have been as low as  $1.1M_\odot$  [115].

The theoretical bounds on the neutron star mass allow for an even larger mass range (and thus, in principle, large mass ratios, up to  $\sim 3$ ), as some EOSs have maximum masses of  $\sim 3M_\odot$  (e.g., the  $\sim 2.8M_\odot$  maximum masses for the MS1 and MS1b EOSs we consider in this work; see Table I). However, the minimum mass of neutron stars in the universe is likely around the minimum observed mass of  $\sim 1M_\odot$ . While the minimum mass of a star constructed from a cold dense matter equation of state is quite small ( $< 0.1M_\odot$ ), the minimum mass of a hot protoneutron star is considerably larger,  $0.89$ – $1.13M_\odot$  for the models considered in [116]. This minimum mass provides a practical lower bound on neutron star masses formed from supernovae, barring formation of lower-mass stars by fragmentation (see, e.g., [117]), which is quite speculative. Moreover, the high kicks that neutron stars formed by fragmentation would be expected to receive make them unlikely components of binaries. Additionally, there is a further restriction from the baryonic mass of the iron core of the supernova progenitor, which gives a minimum mass of  $1.15$ – $1.2M_\odot$ , as discussed in Sec. 3.3 of [1], though there are uncertainties in both these bounds due to uncertainties in supernova physics. (Note that Tauris, Langer, and Podsiadlowski [118] estimate that the minimum mass of a neutron star formed in an ultra-stripped supernova is  $1.1M_\odot$ .) See [1, 2] for a general review of neutron star masses.

<sup>11</sup> Note that these authors quote compactnesses in units of  $M_\odot/\text{km}$ , not the dimensionless compactnesses we use in this work, as is mentioned explicitly in the caption to Fig. 1 of [114].



As mentioned in Sec. I, the mass range of the observed binary neutron star systems is much smaller, particularly if one only considers the six systems that will merge within a Hubble time, where the minimum and maximum masses are  $1.25$  and  $1.44M_{\odot}$  (PSRs J0737–3039B and B1913+16, the less massive star in the Double Pulsar and the Hulse-Taylor pulsar, respectively), and the largest observed mass ratio is  $1.07$ , for the Double Pulsar (see, e.g., Table 1 in [1, 2] and Table 3 in [119]). Thus, one might naïvely not expect to see a very wide range of masses (and thus mass ratios) in many binary neutron star coalescences. However, for certain values of poorly constrained parameters, population synthesis calculations (e.g., the Synthetic Universe models from Dominik *et al.* [7]) predict the existence of binary neutron stars (formed “*in situ*,” i.e., not by dynamical capture) with masses over the entire observed range of neutron star masses, and some systems with reasonably large mass ratios.

Let us now consider the predictions of the Synthetic Universe population synthesis data available online [120]; these are the standard model and Variations 1–15 of Dominik *et al.* [7], where each of the variations varies one of the poorly constrained parameters in the calculation—see Table 1 in [7]. (See [121] for a study of the predicted gravitational wave detection rates using a few of these models and [122] for a study of the effects of varying certain initial conditions.) Additionally, each of these models has four further variants, given by the four combinations of two choices for the metallicity (solar and 0.1 solar)<sup>12</sup> and two treatments of the common envelope phase of the binary’s evolution (submodels A and B, which correspond to the optimistic and pessimistic predictions, respectively, for the fate of binaries which enter the common envelope phase when the donor is in the Hertzsprung gap). These models all assume a minimum neutron star mass of  $1M_{\odot}$  (as mentioned in [121]) and a maximum mass of  $2.5M_{\odot}$  (except for Variations 5 and 6, which assume a maximum mass of 3 and  $2M_{\odot}$ , respectively).

All of these models predict a galactic binary neutron star merger rate above the estimated lower bound of  $2.1 \text{ Myr}^{-1}$  inferred from observations (see the discussion in Sec 4.1 of [124]) at solar metallicity, except for Variation 1 (both submodels), and submodel B in Variations 2, 4, and 12 (see Table 2 in [7]). We still show results for these models, for comparison, particularly since that lower bound is not particularly firm.

We show the total number of coalescing binaries in each of these models in Fig. 22, marking the numbers of systems with individual masses  $\geq 1.5$ ,  $1.75$ , and  $2M_{\odot}$ . We also show the maximum and minimum individual masses and mass ratio present in the coalescing systems in that figure. (Here we select the systems that coalesce within 10 Gyr from the formation of the binary, the criterion

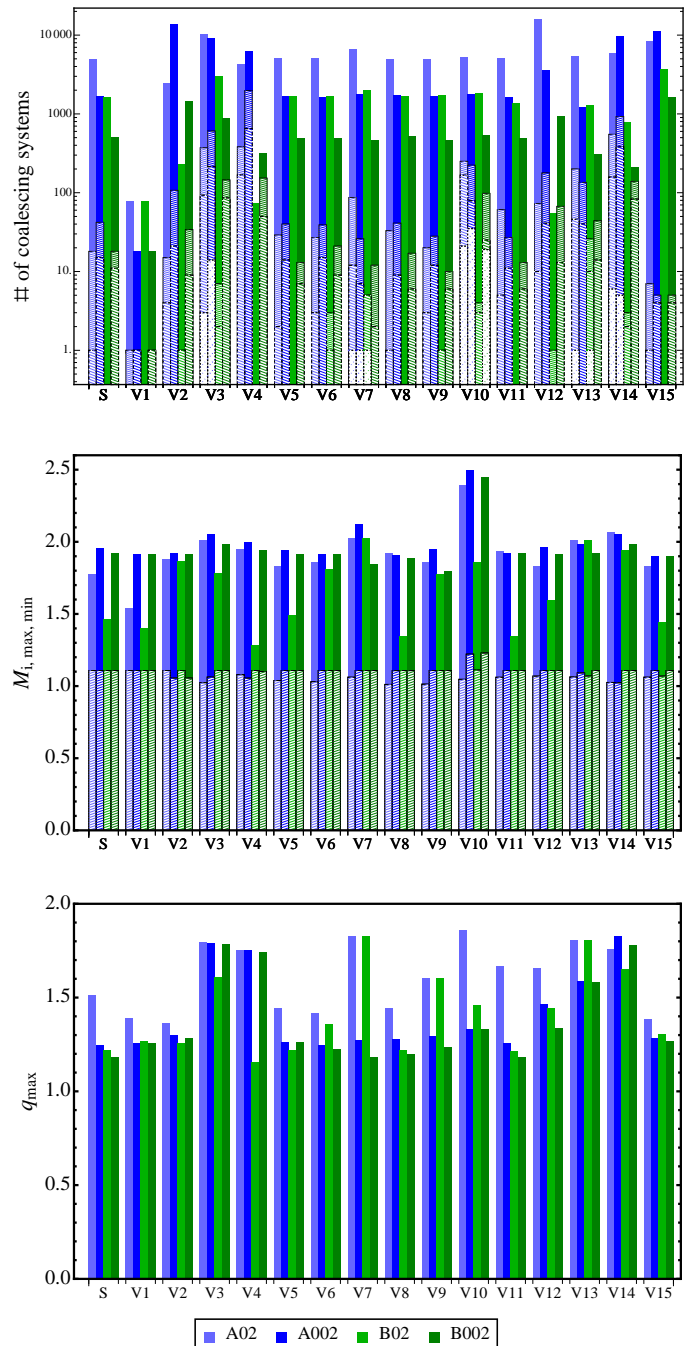


FIG. 22: The total number of coalescing binary neutron star systems in the various Synthetic Universe population synthesis models, with the numbers with individual masses greater than  $\geq 1.5$ ,  $1.75$ , and  $2M_{\odot}$  also marked (top), along with the maximum and minimum individual masses (middle) and maximum mass ratio (bottom) present in these models. Here “S” denotes the standard model and “Vn” denotes the  $n$ th variation. The four variants are denoted by different colored bars, where the letter (A or B) gives the submodel and “02” and “002” correspond to solar metallicity and 0.1 solar metallicity, respectively, the notation used on the Synthetic Universe webpage. In the top plot, the number of coalescing systems with individual masses  $\geq 1.5$ ,  $1.75$ , and  $2M_{\odot}$  are marked with dense hatching, less dense hatching, and dotted hatching, respectively.

<sup>12</sup> Note that the metallicity of objects in the universe varies, generally increasing for more recent formation times, as discussed in, e.g., [123]. These two choices of metallicities are intended to give an indication of the effects of metallicity on these calculations.

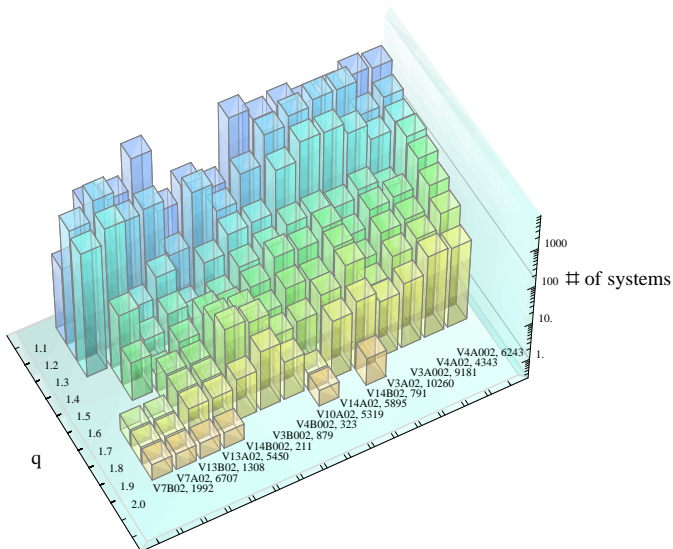


FIG. 23: A histogram of mass ratio of coalescing systems for the various Synthetic Universe models that have a maximum (coalescing) mass ratio of  $\geq 1.7$ . The number of coalescing systems in each model is given after the model's name (with the same notation as in Fig. 22). Each bin has size 0.1 and is labeled by the maximum mass ratio present in the bin. The models are ordered to help clarify the plot.

for the population of potentially observable coalescing binaries used in [7].) We see that many of the models predict at least some coalescing systems with individual masses close to  $2M_{\odot}$  (at least above  $1.75M_{\odot}$ ). The minimum individual masses present are mostly close to  $1.1M_{\odot}$ , though in a few models they approach the minimum mass of  $1M_{\odot}$ , while in Variation 10 (which assumes a delayed supernova engine), the minimum mass in the low metallicity case is  $1.2M_{\odot}$ . The maximum total mass is never more than 20% smaller than twice the maximum individual mass, and in almost half of the cases is within 5% of it.

The minimum total mass is always very close to  $2.2M_{\odot}$ , except for Variation 1, where it is  $2.49M_{\odot}$  (for all four cases), and Variation 10, where it is between  $2.3$  and  $2.5M_{\odot}$ , depending on the case. Indeed, mergers with a stable neutron star as the final remnant may even be rather common, if the neutron star maximum mass is  $\gtrsim 2.5M_{\odot}$  as is assumed in all but Variation 6: One finds hundreds to thousands of coalescing systems with total masses below this limit in all but a handful of these Synthetic Universe models. Moreover, these numbers are a significant fraction of the total number of systems in each of the population models (in a number of cases well above 90%, including the standard case with solar metallicity and submodel B, where the fraction is 99.88%). There are even tens to hundreds of coalescing systems with total masses less than  $2.25M_{\odot}$  in many models. In the models from [122], which vary various initial conditions using a base model quite similar to the standard model from [7], one does not find many of the more extreme systems we consider here, since these models do not include the choices for the binary evolution parameters that

generate such systems.

Since there is a wide range of individual masses in these models, one might expect there to also be a wide range of mass ratios present, which we indeed find to be the case, as illustrated in the bottom panel of Fig. 22. We also show a histogram of the number of systems with different mass ratios for the models that have maximum mass ratios  $\geq 1.7$  in Fig. 23. The maximum mass ratio in the full (not just the coalescing) population is 1.94, found in Variation 10 with solar metallicity and either submodel. The maximum mass ratio in the coalescing population is 1.86 and is also found in Variation 10 with solar metallicity, though here just for submodel A. Note that this variation assumes a delayed supernova engine, and thus may be unphysical, as discussed in [7]. We therefore note that Variation 7 (which assumes low supernova kicks) with solar metallicity gives a maximum mass ratio of 1.83 in both the full and coalescing populations for both submodels, as does Variation 14 (which assumes a weakly bound common envelope) for 0.1 solar metallicity and submodel A.

While the very largest mass ratios are indeed uncommon even in these more extreme population models (see Fig. 23), two models predict  $> 50$  coalescing systems with mass ratios  $\geq 1.7$  (Variation 4, which assumes a very weakly bound common envelope, with submodel A and either metallicity). These models are on the extreme side, but even the standard model predicts a single mass ratio 1.5 coalescing system (with submodel A and solar metallicity).

## 2. Larger spins

Compared to the spins of millisecond pulsars (where the largest spin known is 716 Hz [125]), the members of known binary neutron stars are not spinning nearly so rapidly.<sup>13</sup> The shortest spin period observed so far is 22.7 ms (corresponding to a frequency of 44 Hz) for the more massive star in the Double Pulsar, PSR J0737–3039A, which is likely not to spin down too much by the time the system merges, as discussed in Appendix A 3. PSR J0737–3039A has a dimensionless spin of  $j \in [0.02, 0.03]$ , where the uncertainty comes from the uncertainty in the EOS.

However, for a direct estimate of the typical spin in binary neutron star systems, we are restricted by the fact that we currently only know a small sample of the binary neutron star systems in our galaxy (around twelve). Furthermore, the existence of the sizeable population of rapidly spinning neutron stars, with 207 known pulsars

<sup>13</sup> While PSR J1807–2500B (NGC 6445B) has a spin of 239 Hz, it is at present unclear whether its companion is a neutron star or a white dwarf [126]. (The uncertainty about the nature of the companion is somewhat larger for this system than it is for most binary pulsars. This is also the most massive companion of a fully recycled neutron star.) Additionally, this system will not merge within a Hubble time, so it would not contribute directly to binary neutron star merger rate calculations.

with spins over 200 Hz [127]<sup>14</sup> suggests that there should be a population of binary neutron stars where at least one star has a significant spin at merger. (Note that 200 Hz corresponds to a dimensionless spin of  $\sim 0.1$  for the EOSs considered in this work.) This would most likely be the heavier star, which could have its spin increased by accretion from its companion when its companion is still a post-main sequence star, a process known as recycling (see, e.g., [129]). (The recycling process reduces the star's external magnetic field, which will likely allow the rapid spin obtained from accretion to persist until merger.)

However, one needs to accrete a fair amount of matter in order to spin a neutron star up to high frequencies ( $\sim 0.1M_\odot$  for frequencies of  $\sim 500$  Hz is quoted in Sec. 7 in [129]), and one does not expect to accrete lots of matter when the companion is a neutron star progenitor. In particular, Tauris, Langer, and Podsiadlowski [118] consider the ultra-stripped supernova binary neutron star formation channel, which they claim is the primary channel for forming binary neutron stars that will merge within a Hubble time. In their calculations, they obtain a maximum spin of  $\sim 40$  Hz, assuming Eddington-limited accretion onto the neutron star, and  $\sim 90$  Hz, assuming three times Eddington accretion (which they mention is easily obtained, and for which there may be evidence in the inferred formation channels of other systems); see their Sec. 6.1.1.

Additionally, MacLeod and Ramirez-Ruiz [130] find that even though the neutron star only accretes  $< 0.1M_\odot$  during the common envelope phase in their simulations, the neutron star could still be spun up to  $\sim 250$  Hz in the cases where one accretes close to  $0.1M_\odot$ . Of course, if the neutron star experiences a significant enough spin-down after the accretion episode, then these high spins will reduce substantially before merger. However, one expects the magnetic field to be reduced by accretion, as mentioned above, and for reasonably small periods and magnetic fields after the common envelope phase (e.g.,  $\sim 4$  hours and  $\sim 10^9$  G), the spin at merger can still be  $\sim 200$  Hz. See the next subsection for further discussion of the issue of determining the spin at merger.

One can also imagine forming a double neutron star with a member with a high spin through dynamical formation via binary-single (or even binary-binary) interactions in dense stellar regions, such as globular clusters (see, e.g., [8, 10]), where one swaps out the companion that recycled the highly spinning neutron star. This process is discussed as a likely formation channel for the binary containing the 239 Hz pulsar J1807–2500B [126], which resides in a globular cluster, and whose companion may be another neutron star. There is even the exotic possibility of forming a binary where both neutron stars have millisecond periods through this channel, or through the double recycling scenario proposed by Sigurdsson and Hernquist [9], where the neutron stars' main

sequence companions are disrupted and this material recycles both neutron stars.

### 3. Neutron star spin predictions at merger

In addition to considering the purely theoretical prospects for relatively high spin in merging binary neutron stars, one can also consider the spins at merger of known pulsars whose companion is a neutron star. The simplest way to estimate the spin at merger is to assume that the pulsar's observed spindown is due solely to magnetic dipole radiation. This was already done for the fastest-spinning neutron star known in a neutron star binary (J0737–3039A, the more massive star in the Double Pulsar) by one of us in [23]. There it was found that this pulsar's spin will only decrease slightly, from 44 to 37 Hz, in the 85 Myr from now until the system merges, with this assumption. Although the observed spindown is likely not due entirely to magnetic dipole radiation, we will show that the estimate for this particular pulsar is valid without this assumption (with reasonable assumptions about the size of the pulsar's braking index).

For magnetic dipole radiation the pulsar's braking index ( $n := \nu\ddot{\nu}/\dot{\nu}^2$ , where  $\nu$  is the pulsar's spin frequency) is 3. However, all reliably measured values of the braking index (only 8) are less than 3 (and can be as low as  $\sim 1$ ); see, e.g., Table I in [131]. Note that all of the pulsars with reliably measured braking indices are much younger than J0737–3039A, with ages of at most  $\sim 10^4$  years, as opposed to J0737–3039A's age of  $\sim 10^8$  years. If one looks at these braking indices versus the pulsars' characteristic ages from the ATNF catalogue [127], one sees that the significantly older pulsars all have lower—but more uncertain—braking indices than the younger ones. (See Fig. 7.5 in [132] for an illustration, albeit without error bars. They also plot less well-determined braking indices for much older pulsars, finding quite large values up to  $\sim 10^5$ , though they are also likely quite uncertain.) All these pulsars are also more slowly rotating than J0737–3039A, with a largest frequency of  $\sim 30$  Hz for the Crab pulsar. Nevertheless, it turns out that the prediction of J0737–3039A's spin at merger is quite insensitive to the braking index assumed, since the spin-down timescale is considerably longer than the time to merger.

Specifically, the period evolution of a pulsar with a generic (constant) braking index  $n$  is given by  $\dot{P} = KP^{2-n}$ , where  $K$  is a constant. We can solve this in terms of the pulsar's period at  $t = 0$ ,  $P_0$ , and express  $K$  in terms of the pulsar's characteristic age at  $t = 0$ ,  $\tau_0 := P_0/(2\dot{P}_0)$ , giving

$$\begin{aligned} P(t) &= P_0 \left[ 1 + \frac{n-1}{2} \frac{t}{\tau_0} \right]^{1/(n-1)} \\ &= P_0 \left\{ 1 + \frac{1}{2} \frac{t}{\tau_0} + \frac{2-n}{8} \left( \frac{t}{\tau_0} \right)^2 + O \left( \left[ \frac{t}{\tau_0} \right]^3 \right) \right\}, \end{aligned} \quad (\text{A1})$$

Here we have expanded to second order in  $t/\tau_0$  to illus-

<sup>14</sup> This is out of 2525 known pulsars. Also note that 20 out of the 23 known pulsars in the rich globular cluster 47 Tucanae have spins over 200 Hz [128].

trate that the correction term due to the braking index is quite small when  $t/\tau_0$  is small. In case of J0737–3039A, where  $\tau_0 = 210$  Myr, so  $t_{\text{merger}}/\tau_0 \simeq 0.4$ , the corrections due to possible deviations of the braking index from 3 are  $\lesssim 5\%$  (considering  $n \in [0, 5]$ , where  $n = 5$  corresponds to pure gravitational wave damping). Additionally, for the very large magnitude (and likely quite uncertain) braking indices found for pulsars of about the age of J0737–3039A discussed above, the change in the pulsar’s spin until merger is negligible.

Of course, this calculation still assumes a constant braking index and  $K$ . If, for instance, J0737–3039A has a large buried magnetic field from the accretion episode that is thought to have spun it up (its external field is only  $6.3 \times 10^9$  G, while its companion’s is  $\sim 10^{12}$  G) [133], and enough of this field becomes unburied before the binary coalesces, then this could spin the pulsar down far more than is predicted by the calculation above: Since the spin-down rate goes as the square of the magnetic field, an increase in the external field by an order of magnitude would decrease the characteristic age  $\tau$  by a factor of 100, so one could easily obtain a final spin that was smaller by a factor of 2 or more if this larger external field is present for  $\sim 10$  Myr or longer. And if a  $\sim 10^{12}$  G field emerges completely,  $\tau$  will decrease to  $\sim 10^4$  years, so such an external field could spin the star down by an order of magnitude in only  $\sim 1$  Myr.

However, this scenario relies on the pulsar’s having accreted a small enough amount of matter to allow a significant amount of field to become unburied in the remaining time before merger. As illustrated in, e.g., Fig. 1 of [134], the unburial timescale is very sensitive to the amount of accreted material (with factors of 2 leading to order of magnitude changes). Since there is no way of which we are aware of estimating the amount of material accreted onto J0737–3039A to within a factor of 2, and the entire picture is further complicated by the possibility of magnetic field decay (e.g., Ohmic decay), not just burial (see, e.g., Sec. 10.3.1 in [135] for a brief review), we do not pursue this possibility further here.

## Appendix B: Alternative derivation of a first integral to the Euler equation

We have already outlined a possible derivation of a first integral to Euler’s equation for rotating neutron stars, see Sec. II A and [23, 24]. In this appendix we obtain the first integral using a much shorter derivation based on the Cartan identity, which relates the Lie derivative operator  $\mathcal{L}$  to the exterior derivative operator  $\mathbf{d}$ . In particular, for a differential form  $\omega$  and a vector  $\mathbf{u}$  one has

$$\mathcal{L}_{\mathbf{u}}\omega = \mathbf{u} \cdot \mathbf{d}\omega + \mathbf{d}(\mathbf{u} \cdot \omega). \quad (\text{B1})$$

where a dot denotes contraction between adjacent indices. We will now use the canonical momentum

$$\mathbf{p} = h\mathbf{u} = \mathbf{d}\phi + \mathbf{w} \quad (\text{B2})$$

as introduced in Eqs. (2.20) and (2.23), together with the additional definition (2.25), to write

$$\mathbf{p} = p^0 \bar{\mathbf{k}} + \mathbf{w} = p^0(\mathbf{k} + \mathbf{V}), \quad (\text{B3})$$

where in the last step we have used Eqs. (2.19) and (2.20).

Using  $\mathbf{u} \cdot \mathbf{u} = -1$ , the Euler equation (2.11) can be written in the Carter-Lichnerowicz [136, 137] form:

$$\mathbf{u} \cdot \mathbf{d}\mathbf{p} = 0, \quad (\text{B4})$$

Using Eq. (2.19), Eq. (B4) can be rewritten as

$$\mathbf{k} \cdot \mathbf{d}\mathbf{p} + \mathbf{V} \cdot \mathbf{d}\mathbf{p} = 0. \quad (\text{B5})$$

We now rewrite  $\mathbf{k} \cdot \mathbf{d}\mathbf{p}$  using the Cartan identity (B1) to obtain

$$\mathcal{L}_{\mathbf{k}}\mathbf{p} - \mathbf{d}(\mathbf{k} \cdot \mathbf{p}) + \mathbf{V} \cdot \mathbf{d}\mathbf{p} = 0, \quad (\text{B6})$$

where  $\mathcal{L}_{\mathbf{k}}\mathbf{p}$  vanishes by assumption if the symmetry vector  $\mathbf{k}$  Lie-derives the flow. We could then obtain a first integral  $\mathbf{k} \cdot \mathbf{p} = \text{const}$  for irrotational ( $\mathbf{d}\mathbf{p} = 0$ ) or corotational ( $\mathbf{V} = 0$ ) flow, since then the last term is zero as well. In the general case of spinning neutron stars, however, that is not true. Nevertheless, we can again make use of our assumptions (2.24b), (2.24c), and (2.27) (this time without projecting onto the three dimensional slice), i.e.,

$$\mathcal{L}_{\mathbf{k}}\mathbf{d}\phi \approx \mathcal{L}_{\bar{\mathbf{k}}}\mathbf{w} \approx \mathcal{L}_{\frac{\mathbf{w}}{p^0}}\mathbf{w} \approx 0, \quad (\text{B7})$$

where the latter two can be combined to get

$$\mathcal{L}_{\frac{\mathbf{p}}{p^0}}\mathbf{w} = \mathcal{L}_{\bar{\mathbf{k}}}\mathbf{w} + \mathcal{L}_{\frac{\mathbf{w}}{p^0}}\mathbf{w} \approx 0. \quad (\text{B8})$$

Now it is possible to rewrite the first and the last term of equation (B6) with the goal of finding a first integral. Therefore, we can write  $\mathcal{L}_{\mathbf{k}}\mathbf{p} = \mathcal{L}_{\mathbf{k}}(\mathbf{d}\phi + \mathbf{w}) \approx \mathcal{L}_{\mathbf{k}}\mathbf{w}$  to simplify the first term. For the last term, we will apply Cartan’s identity once again and the definitions from (B2) to write

$$\mathbf{V} \cdot \mathbf{d}\mathbf{p} = \mathbf{V} \cdot \mathbf{d}\mathbf{w} = \mathcal{L}_{\mathbf{V}}\mathbf{w} - \mathbf{d}(\mathbf{V} \cdot \mathbf{w}). \quad (\text{B9})$$

Substituting these two terms into (B6) and exploiting linearity of the Lie derivative yields

$$\mathbf{d}(\mathbf{k} \cdot \mathbf{p} + \mathbf{V} \cdot \mathbf{w}) \approx \mathcal{L}_{\mathbf{k}+\mathbf{V}}\mathbf{w} = \mathcal{L}_{\bar{\mathbf{k}}+\frac{\mathbf{w}}{p^0}}\mathbf{w} \approx 0. \quad (\text{B10})$$

which gives rise to an approximate first integral

$$\mathbf{k} \cdot \mathbf{p} + \mathbf{V} \cdot \mathbf{w} \approx \text{const} \quad (\text{B11})$$

In a final step, using the normalization condition  $\mathbf{u} \cdot \mathbf{u} = -1$ , one can straightforwardly show that  $\mathbf{k} \cdot \mathbf{p} + \mathbf{V} \cdot \mathbf{w} = -\frac{h}{u^0} - \mathbf{V} \cdot \mathbf{d}\phi$ , which corresponds to equation (2.30).

Notice, however, that the assumptions (B7) used in the derivation here are slightly stronger than the original assumptions (2.24b), (2.24c) and (2.27), which make assumptions only about projections onto the three dimensional slice.

## Appendix C: Single CRV-stars

### 1. Comparison with rigidly rotating stars

As explained in [24], the particular choice of the angular velocity  $w^i$  given by Eq. (2.35) leads to a negligible

shear, thus any substantial differential rotation can be neglected. We provide corroborating evidence for this statement here. For this purpose we construct single rotating neutron stars in the CRV approach and compare them with rigidly rotating stars. We compute the rigidly rotating stars with the project `Nrotstar` of the publicly available LORENE library [15]. `Nrotstar` solves the Einstein equations with a self-consistent field method and multi-domain spectral methods. To compute CRV stars, we use SGRID and the formalism described in Sec. II. In particular, we take the approximate symmetry vector  $\mathbf{k}$  to be the timelike Killing vector  $\partial_t$ . We also use  $n_A = n_B = 26$ ,  $n_\varphi = 8$ , and  $n_{\text{Cart}} = 22$ .

In Fig. 24 we present sequences of CRV and rigidly rotating stars with the simple polytropic  $\Gamma 2.72$  EOS for different central enthalpies (i.e. different baryonic masses). There is no evidence that the result would be different for piecewise polytropes.

Due to the fact that  $\omega^z$  in the CRV approach does not agree with the frequency measured by an observer at infinity (as already outlined in [38]), we compute CRV configurations for a constant  $\omega^z$  and find a corresponding sequence of rigidly rotating stars by choosing the frequency in `Nrotstar` such that both methods give similar results. We obtain the SGRID data by varying the baryonic masses  $M_b \in [1.1, 2.0]$  with a spacing of  $\Delta M_b = 0.1$ . We clearly see that for frequencies below 300Hz, rigidly rotating data and CRV data agree well. However for larger angular momentum larger discrepancies occur. This can be caused by (i) the reduced accuracy for faster rotating stars (see Sec. C 3) and (ii) the fact that the members of a sequence with different masses and the same  $\omega^z = \text{const}$  may not all correspond to the same observable frequency.

## 2. Empirical $\omega$ - $j$ -Relation

In addition to the comparison with rigid rotating stars, we want to answer the question of how the dimensionless spin of a single CRV-star can be obtained from input parameters of the SGRID code, namely the EOS, the baryonic mass  $M_b$ , and the angular velocity vector  $\omega^i$ . A phenomenological model to obtain a rough estimate of the star's spin value would reduce the computational costs to find accurate initial data for particular configurations. For this reason we choose four EOS: SLy, ALF2, MS1b, and  $\Gamma 2$  with baryonic masses in the range  $[1.1, 1.7]$ , spanning a range in the compactness of  $\mathcal{C} \in (0.09, 0.20)$ .

The dimensionless angular momentum  $j$  of a neutron star is given by

$$j = \frac{J_{\text{ADM}}}{M_{\text{ADM}}^2} = \frac{I\omega_{\text{obs}}}{M_{\text{ADM}}^2}, \quad (\text{C1})$$

where  $J_{\text{ADM}}$  and  $M_{\text{ADM}}$  are the spacetime's ADM angular momentum and mass, respectively, and  $I$  the moment of inertia of the star. Now  $\omega_{\text{obs}}$ , the rotational period an observer at infinity would measure, is not known *a priori*, but probably depends linearly on the angular velocity  $\omega$ , for slowly rotating neutron stars. We thus recast Eq. (C1)

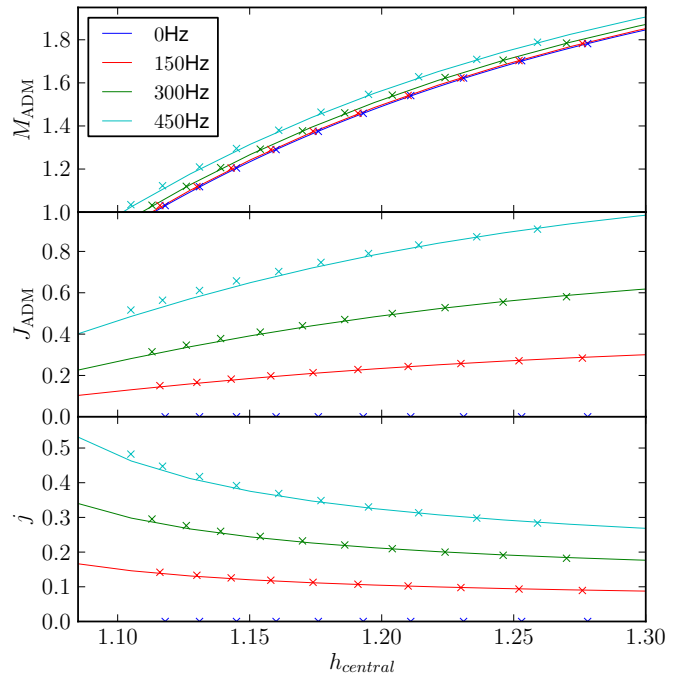


FIG. 24: Comparison of single neutron stars with rigid rotation and CRV rotation using a simple polytropic EOS ( $\Gamma 2.72$ ). The values for  $\omega^z$  in the CRV-approach are 0.0, 0.005, 0.01, and 0.015. (These data are shown as crosses.) The solid lines are computed for rigidly rotating stars with the LORENE library.

in the form

$$j = f(\mathcal{C}, M_b)\omega. \quad (\text{C2})$$

Also, the gravitational mass of the single star (i.e.,  $M_{\text{ADM}}$ ) for this spacetime is not known in advance and is thus absorbed in the function  $f$ . We find with numerical experiments the following expression:

$$j_{\text{fit}} = a_1(1 + m_1 M_b)(1 + c_1 \mathcal{C} + c_2 \mathcal{C}^2 + c_3 \mathcal{C}^3 + c_4 \mathcal{C}^4)\omega, \quad (\text{C3})$$

where the parameters  $a_1 = 88.8131$ ,  $m_1 = 1.39522$ ,  $c_1 = -19.003$ ,  $c_2 = 152.99$ ,  $c_3 = -570.678$ ,  $c_4 = 806.896$  are obtained from a fit of the data presented in Fig. 25 and where we use the compactness  $\mathcal{C}$  of an irrotational star with the same baryonic mass for simplicity. Specifically, we computed five different values  $\omega = (0.000, 0.002, 0.004, 0.006, 0.008)$  for each of the baryonic masses (1.1, 1.2, 1.3, 1.4, 1.5, 1.6, 1.7) and for the EOSs SLy, ALF2, MS1b, and  $\Gamma 2$ . We want to stress that the resulting relation is just empirical and probably does not represent any underlying physical properties.

## 3. Rapidly rotating neutron stars

The fastest spinning neutron star observed so far is PSR J1748–2446ad, with a spin period of 1.4 ms, corresponding to a frequency of 716 Hz [125]. This corresponds to a dimensionless spin of  $j \in [0.3, 0.6]$  (for the EOSs given in Tab. I), where the uncertainty comes from our ignorance of the EOS and the mass of the star.



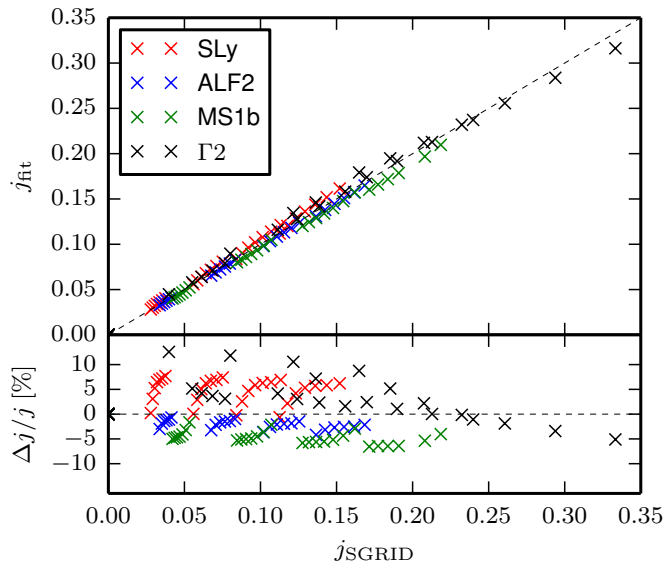


FIG. 25: Comparing the spin computation according to Eq. (C3) ( $j_{\text{fit}}$ ) with the spin output by SGRID ( $j_{\text{SGRID}}$ ) for SLy (red), ALF2 (blue), MS1b (green), and  $\Gamma^2$  (black). Absolute values (upper panel) and fractional residuals (bottom panel).

Considering such systems, it is interesting to estimate the maximum spin that can be achieved with SGRID. For this purpose we consider once more the SLy, ALF2,

and MS1b EOSs and single star configurations. The iteration process to achieve high spins for realistic EOSs is as follows. We start with  $\omega = 0$  (zero spin, i.e., a solution of the TOV-equation) and increase the angular velocity in steps of  $\Delta\omega = 0.005$  up to  $\omega = 0.01$  and in smaller steps of  $\Delta\omega = 0.0025$  up to  $\omega = 0.0275$ . Note that higher spins could be computed for lower resolutions, but for higher resolutions the iteration procedure fails. Depending on the EOS, maximum dimensionless spins of  $0.5 \leq j_{\text{max}} \leq 0.7$  can be obtained (shown in the upper panel of Fig. 26). The middle panel shows the mass shedding parameter [138]

$$\chi = \frac{\partial_r h|_{\text{eq}}}{\partial_r h|_{\text{pole}}} \quad (\text{C4})$$

which measures the deformation of the neutron star (caused by its rotation) according to the derivative of the enthalpy at the star's surface parallel or perpendicular to the symmetry axis. Note that in binaries  $\partial_r h|_{\text{eq}}$  is evaluated along the line connecting the two stars' centers. The lower panel shows the  $L^2$ -norm Hamiltonian constraint in the domain covering the neutron star up to  $A_{\text{max}} = 0.35$ , i.e., including the star's surface, which is the most problematic region. The Hamiltonian constraint grows for angular velocities  $\omega \geq 0.02$ . We suggest that this is related to the deformed shape of the neutron star, indicated by the decreasing  $\chi$ .

- 
- [1] J. M. Lattimer, *Ann. Rev. Nucl. Part. Sci.* **62**, 485 (2012), 1305.3510.
  - [2] J. M. Lattimer, *Observed neutron star masses*, <http://www.stellarcollapse.org/nsmasses>.
  - [3] P. C. Peters, *Phys. Rev.* **136**, B1224 (1964).
  - [4] I. Kowalska, T. Bulik, K. Belczynski, M. Dominik, and D. Gondek-Rosinska, *Astron. Astrophys.* **527**, A70 (2011), 1010.0511.
  - [5] J. van Leeuwen et al., *Astrophys. J.* **798**, 118 (2015), 1411.1518.
  - [6] J. K. Swiggum et al., *Astrophys. J.* **805**, 156 (2015), 1503.06276.
  - [7] M. Dominik, K. Belczynski, C. Fryer, D. E. Holz, E. Berti, T. Bulik, I. Mandel, and R. O'Shaughnessy, *Astrophys. J.* **759**, 52 (2012), 1202.4901.
  - [8] M. J. Benacquista and J. M. B. Downing, *Living Rev. Relativity* **16**, 4 (2013), 1110.4423.
  - [9] S. Sigurdsson and L. Hernquist, *Astrophys. J. Lett.* **401**, L93 (1992).
  - [10] F. Verbunt and P. C. C. Freire, *Astron. Astrophys.* **561**, A11 (2014), 1310.4669.
  - [11] W. H. Lee, E. Ramirez-Ruiz, and G. van de Ven, *Astrophys. J.* **720**, 953 (2010), 0909.2884.
  - [12] M. Favata, *Phys. Rev. Lett.* **112**, 101101 (2014), 1310.8288.
  - [13] M. Agathos, J. Meidam, W. Del Pozzo, T. G. F. Li, M. Tompitak, J. Veitch, S. Vitale, and C. Van Den Broeck (2015), 1503.05405.
  - [14] C. L. Rodriguez, B. Farr, V. Raymond, W. M. Farr, T. B. Littenberg, D. Fazi, and V. Kalogera, *Astrophys. J.* **784**, 119 (2014), 1309.3273.
  - [15] E. Gourgoulhon, P. Grandclément, J.-A. Marck, J. Novak, and K. Taniguchi, <http://www.lorene.obspm.fr>.
  - [16] W. E. East, F. M. Ramazanoglu, and F. Pretorius, *Phys. Rev. D* **86**, 104053 (2012), 1208.3473.
  - [17] N. Moldenhauer, C. M. Markakis, N. K. Johnson-McDaniel, W. Tichy, and B. Brügmann, *Phys. Rev. D* **90**, 084043 (2014), 1408.4136.
  - [18] A. Tsokaros, K. Uryū, and L. Rezzolla, *Phys. Rev. D* **91**, 104030 (2015), 1502.05674.
  - [19] F. Foucart, L. E. Kidder, H. P. Pfeiffer, and S. A. Teukolsky, *Phys. Rev. D* **77**, 124051 (2008), 0804.3787.
  - [20] H. Pfeiffer, N. Tacik, F. Foucart, R. Haas, J. Kaplan, C. Muhlberger, M. Duez, L. Kidder, M. Scheel, and B. Szilagyi, in *APS Meeting Abstracts* (2015), p. 13004.
  - [21] N. Tacik *et al.* (unpublished).
  - [22] W. Tichy, *Classical Quantum Gravity* **26**, 175018 (2009), 0908.0620.
  - [23] W. Tichy, *Phys. Rev. D* **84**, 024041 (2011), 1107.1440.
  - [24] W. Tichy, *Phys. Rev. D* **86**, 064024 (2012), 1209.5336.
  - [25] A. Buonanno, L. E. Kidder, A. H. Mroué, H. P. Pfeiffer, and A. Taracchini, *Phys. Rev. D* **83**, 104034 (2011), 1012.1549.
  - [26] W. Tichy and P. Marronetti, *Phys. Rev. D* **83**, 024012 (2011), 1010.2936.
  - [27] A. H. Mroué and H. P. Pfeiffer (2012), 1210.2958.
  - [28] M. Pürrer, S. Husa, and M. Hannam, *Phys. Rev. D* **85**, 124051 (2012), 1203.4258.
  - [29] K. Kyutoku, M. Shibata, and K. Taniguchi, *Phys. Rev. D* **90**, 064006 (2014), 1405.6207.
  - [30] R. Gold, S. Bernuzzi, M. Thierfelder, B. Brügmann, and F. Pretorius, *Phys. Rev. D* **86**, 121501(R) (2012),

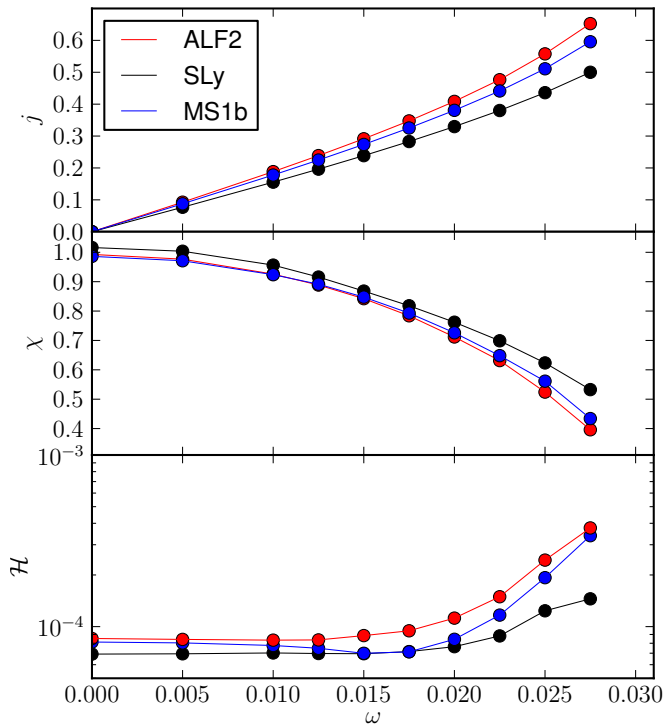


FIG. 26: The dimensionless spin (top panel), mass shedding parameter (middle panel), and norm of the Hamiltonian constraint (bottom panel) versus the angular velocity  $\omega$  for three EOS (SLy, ALF2, and MS1b).

- 1109.5128.
- [31] W. Kastaun, F. Galeazzi, D. Alic, L. Rezzolla, and J. A. Font, *Phys. Rev. D* **88**, 021501 (2013), 1301.7348.
- [32] P. Tsatsin and P. Marronetti, *Phys. Rev. D* **88**, 064060 (2013), 1303.6692.
- [33] W. Kastaun and F. Galeazzi, *Phys. Rev. D* **91**, 064027 (2015), 1411.7975.
- [34] W. E. East, V. Paschalidis, and F. Pretorius, *Astrophys. J.* **807**, L3 (2015), 1503.07171.
- [35] M. Shibata and K. Taniguchi, *Phys. Rev. D* **73**, 064027 (2006), astro-ph/0603145.
- [36] T. Dietrich, S. Bernuzzi, M. Ujevic, and B. Brügmann, *Phys. Rev. D* **91**, 124041 (2015), 1504.01266.
- [37] K. Taniguchi and M. Shibata, *Astrophys. J. Suppl. Ser.* **188**, 187 (2010), 1005.0958.
- [38] S. Bernuzzi, T. Dietrich, W. Tichy, and B. Brügmann, *Phys. Rev. D* **89**, 104021 (2014), 1311.4443.
- [39] J. A. Faber and F. A. Rasio, *Living Rev. Relativity* **15**, 8 (2012), 1204.3858, URL <http://www.livingreviews.org/lrr-2012-8>.
- [40] M. Shibata, K. Taniguchi, and K. Uryū, *Phys. Rev. D* **71**, 084021 (2005), gr-qc/0503119.
- [41] Y. Sekiguchi, K. Kiuchi, K. Kyutoku, and M. Shibata, *Phys. Rev. Lett.* **107**, 051102 (2011), 1105.2125.
- [42] Y. Sekiguchi, K. Kiuchi, K. Kyutoku, and M. Shibata, *Phys. Rev. Lett.* **107**, 211101 (2011), 1110.4442.
- [43] M. Anderson, E. W. Hirschmann, L. Lehner, S. L. Liebling, P. M. Motl, D. Neilsen, C. Palenzuela, and J. E. Tohline, *Phys. Rev. Lett.* **100**, 191101 (2008), 0801.4387.
- [44] Y. T. Liu, S. L. Shapiro, Z. B. Etienne, and K. Taniguchi, *Phys. Rev. D* **78**, 024012 (2008), 0803.4193.
- [45] B. Giacomazzo, L. Rezzolla, and L. Baiotti, *Mon. Not. R. Astron. Soc. Lett.* **399**, L164 (2009), 0901.2722.
- [46] K. Kiuchi, K. Kyutoku, Y. Sekiguchi, M. Shibata, and T. Wada, *Phys. Rev. D* **90**, 041502(R) (2014), 1407.2660.
- [47] K. Dionysopoulou, D. Alic, and L. Rezzolla (2015), 1502.02021.
- [48] F. Galeazzi, W. Kastaun, L. Rezzolla, and J. A. Font, *Phys. Rev. D* **88**, 064009 (2013), 1306.4953.
- [49] Y. Sekiguchi, K. Kiuchi, K. Kyutoku, and M. Shibata, *Phys. Rev. D* **91**, 064059 (2015), 1502.06660.
- [50] C. Palenzuela, S. L. Liebling, D. Neilsen, L. Lehner, O. L. Caballero, E. O'Connor, and M. Anderson (2015), 1505.01607.
- [51] B. Brügmann, J. A. González, M. Hannam, S. Husa, U. Sperhake, and W. Tichy, *Phys. Rev. D* **77**, 024027 (2008), gr-qc/0610128.
- [52] M. Thierfelder, S. Bernuzzi, and B. Brügmann, *Phys. Rev. D* **84**, 044012 (2011), 1104.4751.
- [53] P. Schmidt, M. Hannam, S. Husa, and P. Ajith, *Phys. Rev. D* **84**, 024046 (2011), 1012.2879.
- [54] D. Hilditch, S. Bernuzzi, M. Thierfelder, Z. Cao, W. Tichy, and B. Brügmann, *Phys. Rev. D* **88**, 084057 (2013), 1212.2901.
- [55] J. W. York, Jr., in *Sources of Gravitational Radiation*, edited by L. Smarr (Cambridge University Press, Cambridge, 1979), pp. 83–126.
- [56] G. Lovelace, R. Owen, H. P. Pfeiffer, and T. Chu, *Phys. Rev. D* **78**, 084017 (2008), 0805.4192.
- [57] K.-W. Lo and L.-M. Lin, *Astrophys. J.* **728**, 12 (2011), 1011.3563.
- [58] M. Ansorg, *Classical Quantum Gravity* **24**, S1 (2007), gr-qc/0612081.
- [59] R. C. Tolman, *Phys. Rev.* **55**, 364 (1939).
- [60] J. R. Oppenheimer and G. Volkoff, *Phys. Rev.* **55**, 374 (1939).
- [61] J. S. Read, B. D. Lackey, B. J. Owen, and J. L. Friedman, *Phys. Rev. D* **79**, 124032 (2009), 0812.2163.
- [62] L. Lindblom, *Phys. Rev. D* **82**, 103011 (2010), 1009.0738.
- [63] P. B. Demorest, T. Pennucci, S. M. Ransom, M. S. E. Roberts, and J. W. T. Hessels, *Nature* **467**, 1081 (2010), 1010.5788.
- [64] J. Antoniadis et al., *Science* **340**, 6131 (2013), 1304.6875.
- [65] T. Damour, A. Nagar, D. Pollney, and C. Reisswig, *Phys. Rev. Lett.* **108**, 131101 (2012), 1110.2938.
- [66] S. Bernuzzi, A. Nagar, M. Thierfelder, and B. Brügmann, *Phys. Rev. D* **86**, 044030 (2012), 1205.3403.
- [67] T. Damour, *Phys. Rev. D* **64**, 124013 (2001), gr-qc/0103018.
- [68] G. Lovelace, M. A. Scheel, and B. Szilágyi, *Phys. Rev. D* **83**, 024010 (2011), 1010.2777.
- [69] M. A. Scheel, M. Giesler, D. A. Hemberger, G. Lovelace, K. Kuper, M. Boyle, B. Szilágyi, and L. E. Kidder, *Classical Quantum Gravity* **32**, 105009 (2015), 1412.1803.
- [70] S. Ossokine, M. Boyle, L. E. Kidder, H. P. Pfeiffer, M. A. Scheel, and B. Szilágyi (2015), 1502.01747.
- [71] C. O. Lousto and J. Healy (2015), 1506.04768.
- [72] M. Levi and J. Steinhoff, *J. Cosmol. Astropart. Phys.* **1412**, 003 (2014), 1408.5762.
- [73] T. Nakamura, K. Oohara, and Y. Kojima, *Prog. Theor. Phys. Suppl.* **90**, 1 (1987).
- [74] M. Shibata and T. Nakamura, *Phys. Rev. D* **52**, 5428 (1995).

- [75] T. W. Baumgarte and S. L. Shapiro, Phys. Rev. D **59**, 024007 (1998), gr-qc/9810065.
- [76] T. Mora and C. M. Will, Phys. Rev. D **69**, 104021 (2004), gr-qc/0312082.
- [77] R.-M. Memmesheimer, A. Gopakumar, and G. Schäfer, Phys. Rev. D **70**, 104011 (2004), gr-qc/0407049.
- [78] H. P. Pfeiffer, D. A. Brown, L. E. Kidder, L. Lindblom, G. Lovelace, and M. Scheel, Classical Quantum Gravity **24**, S59 (2007), gr-qc/0702106.
- [79] S. Husa, M. Hannam, J. A. González, U. Sperhake, and B. Brügmann, Phys. Rev. D **77**, 044037 (2008), 0706.0904.
- [80] B. Walthers, B. Brügmann, and D. Müller, Phys. Rev. D **79**, 124040 (2009), 0901.0993.
- [81] J. G. Baker, J. R. van Meter, S. T. McWilliams, J. Centrella, and B. J. Kelly, Phys. Rev. Lett. **99**, 181101 (2007), gr-qc/0612024.
- [82] M. Hannam, S. Husa, F. Ohme, D. Müller, and B. Brügmann, Phys. Rev. D **82**, 124008 (2010), 1007.4789.
- [83] C. Ronchi, R. Iacono, and P. Paolucci, J. Comput. Phys. **124**, 93 (1996).
- [84] J. Thornburg, Classical Quantum Gravity **21**, 3665 (2004), gr-qc/0404059.
- [85] D. Pollney, C. Reisswig, E. Schnetter, N. Dorband, and P. Diener, Phys. Rev. D **83**, 044045 (2011), 0910.3803.
- [86] L. Blanchet, Living Rev. Relativity **17**, 2 (2014), 1310.1528.
- [87] J. E. Vines and É. É. Flanagan, Phys. Rev. D **88**, 024046 (2013), 1009.4919.
- [88] K. Henriksson, F. Foucart, L. E. Kidder, and S. A. Teukolsky (2014), 1409.7159.
- [89] F. Usui, K. Uryū, and Y. Eriguchi, Phys. Rev. D **61**, 024039 (2000), gr-qc/9906102.
- [90] T. Dietrich and S. Bernuzzi, Phys. Rev. D **91**, 044039 (2015), 1412.5499.
- [91] S. Bernuzzi and D. Hilditch, Phys. Rev. D **81**, 084003 (2010), 0912.2920.
- [92] M. Ruiz, D. Hilditch, and S. Bernuzzi, Phys. Rev. D **83**, 024025 (2011), 1010.0523.
- [93] C. L. Fryer, K. Belczynski, E. Ramirez-Ruiz, S. Rosswog, G. Shen, and A. W. Steiner (2015), 1504.07605.
- [94] M. Dan, S. Rosswog, J. Guillochon, and E. Ramirez-Ruiz, Astrophys. J. **737**, 89 (2011), 1101.5132.
- [95] N. Stergioulas, Living Rev. Relativity **6**, 3 (2003), URL <http://www.livingreviews.org/lrr-2003-3>.
- [96] W. E. East and F. Pretorius, Astrophys. J. Lett. **760**, L4 (2012), 1208.5279.
- [97] K. Hotokezaka, K. Kiuchi, K. Kyutoku, H. Okawa, Y.-i. Sekiguchi, M. Shibata, and K. Taniguchi, Phys. Rev. D **87**, 024001 (2013), 1212.0905.
- [98] K. Kyutoku, K. Ioka, H. Okawa, M. Shibata, and K. Taniguchi (2015), 1502.05402.
- [99] K. Kawaguchi, K. Kyutoku, H. Nakano, H. Okawa, M. Shibata, and K. Taniguchi, Phys. Rev. D **92**, 024014 (2015), 1506.05473.
- [100] S. Bernuzzi, A. Nagar, T. Dietrich, and T. Damour, Phys. Rev. Lett. **114**, 161103 (2015), 1412.4553.
- [101] S. Bernuzzi, T. Dietrich, and A. Nagar (2015), 1504.01764.
- [102] N. Stergioulas, A. Bauswein, K. Zagkouris, and H.-T. Janka, Mon. Not. R. Astron. Soc. **418**, 427 (2011), 1105.0368.
- [103] S. Bernuzzi, A. Nagar, S. Balmelli, T. Dietrich, and M. Ujevic, Phys. Rev. Lett. **112**, 201101 (2014), 1402.6244.
- [104] S. Bernuzzi, A. Nagar, S. Balmelli, T. Dietrich, and M. Ujevic, J. Phys. Conf. Ser. **610**, 012047 (2015).
- [105] T. A. Apostolatos, C. Cutler, G. J. Sussman, and K. S. Thorne, Phys. Rev. D **49**, 6274 (1994).
- [106] L. E. Kidder, Phys. Rev. D **52**, 821 (1995), gr-qc/9506022.
- [107] K. G. Arun, A. Buonanno, G. Faye, and E. Ochsner, Phys. Rev. D **79**, 104023 (2009), **84**, 049901(E) (2011), 0810.5336.
- [108] S. Bernuzzi, M. Thierfelder, and B. Brügmann, Phys. Rev. D **85**, 104030 (2012), 1109.3611.
- [109] K. Hotokezaka, K. Kyutoku, H. Okawa, and M. Shibata, Phys. Rev. D **91**, 064060 (2015), 1502.03457.
- [110] C. Reisswig, R. Haas, C. D. Ott, E. Abdikamalov, P. Mösta, D. Pollney, and E. Schnetter, Phys. Rev. D **87**, 064023 (2013), 1212.1191.
- [111] M. L. Rawls, J. A. Orosz, J. E. McClintock, M. A. Torres, C. D. Bailyn, and M. M. Buxton, Astrophys. J. **730**, 25 (2011), 1101.2465.
- [112] F. Özel, D. Psaltis, R. Narayan, and A. S. Villarreal, Astrophys. J. **757**, 55 (2012), 1201.1006.
- [113] V. Hambaryan, R. Neuhäuser, V. Suleimanov, and K. Werner, J. Phys. Conf. Ser. **496**, 012015 (2014).
- [114] R. Neuhäuser, V. V. Hambaryan, M. M. Hohle, and T. Eisenbeiss, J. Phys. Conf. Ser. **337**, 012073 (2012), 1111.0458.
- [115] M. Fortin, M. Bejger, P. Haensel, and J. L. Zdunik (2014), 1409.1120.
- [116] K. Strobil, C. Schaab, and M. K. Weigel, Astron. Astrophys. **350**, 497 (1999), astro-ph/9908132.
- [117] S. B. Popov, D. Blaschke, H. Grigorian, and M. E. Prokhorov, Astrophys. Space Sci. **308**, 381 (2007), astro-ph/0606308.
- [118] T. M. Tauris, N. Langer, and P. Podsiadlowski, Mon. Not. R. Astron. Soc. **451**, 2123 (2015), 1505.00270.
- [119] K. Postnov and L. Yungelson, Living Rev. Relativity **17**, 3 (2014), 1403.4754.
- [120] <http://www.syntheticuniverse.org>.
- [121] M. Dominik, E. Berti, R. O'Shaughnessy, I. Mandel, K. Belczynski, C. Fryer, D. E. Holz, T. Bulik, and F. Pannarale, Astrophys. J. **806**, 263 (2015), 1405.7016.
- [122] S. E. de Mink and K. Belczynski (2015), 1506.03573.
- [123] M. Dominik, K. Belczynski, C. Fryer, D. E. Holz, E. Berti, T. Bulik, I. Mandel, and R. O'Shaughnessy, Astrophys. J. **779**, 72 (2013), 1308.1546.
- [124] K. Belczynski, M. Dominik, S. Repetto, D. E. Holz, and C. L. Fryer (2012), 1208.0358v2.
- [125] J. W. T. Hessels, S. M. Ransom, I. H. Stairs, P. C. C. Freire, V. M. Kaspi, and F. Camilo, Science **311**, 1901 (2006), astro-ph/0601337.
- [126] R. S. Lynch, P. C. C. Freire, S. M. Ransom, and B. A. Jacoby, Astrophys. J. **745**, 109 (2012), 1112.2612.
- [127] R. N. Manchester, G. B. Hobbs, A. Teoh, and M. Hobbs, Astron. J. **129**, 1993 (2005), astro-ph/0412641, URL <http://www.atnf.csiro.au/research/pulsar/psrcat>.
- [128] P. C. C. Freire, *Pulsars in globular clusters*, <http://www.naic.edu/~pfreire/GCpsr.html>.
- [129] T. M. Tauris, in *Evolution of Compact Binaries*, edited by L. Schmidtbreick, M. R. Schreiber, and C. Tappert (Astronomical Society of the Pacific, San Francisco, CA, 2011), vol. 447 of *Astronomical Society of the Pacific Conference Series*, p. 285, 1106.0897.
- [130] M. MacLeod and E. Ramirez-Ruiz, Astrophys. J. Lett. **798**, L19 (2015), 1410.5421.
- [131] O. Hamil, J. Stone, M. Urbanec, and G. Urbancová,



- Phys. Rev. D **91**, 063007 (2015).
- [132] D. Viganò, Ph.D. thesis, University of Alicante (2013), 1310.1243.
  - [133] D. Lorimer et al., Mon. Not. R. Astron. Soc. **379**, 1217 (2007), 0705.3269.
  - [134] E. J. Young and G. Chanmugam, Astrophys. J. Lett. **442**, L53 (1995).
  - [135] M. Fortin, Ph.D. thesis, Polish Academy of Sciences and Paris Observatory (2012), URL <https://tel.archives-ouvertes.fr/tel-00731478>.
  - [136] B. Carter, in *Active Galactic Nuclei*, edited by C. Hazard and S. Mitton (Cambridge University Press, Cambridge, 1979), p. 273.
  - [137] A. Lichnerowicz, *Relativistic Hydrodynamics and Magnetohydrodynamics* (Benjamin, New York, 1967).
  - [138] M. Shibata and K. Taniguchi, Living Rev. Relativity **14**, 6 (2011), URL <http://www.livingreviews.org/lrr-2011-6>.